

# **New Ternary and Quaternary Layered Arsenides**

by

Danisa Tabassum

A thesis submitted in partial fulfillment of the requirements for the degree of

Master of Science

Department of Chemistry

University of Alberta

© Danisa Tabassum, 2017

## Abstract

New layered ternary and quaternary arsenides have been synthesized by direct reactions of the elements at high temperatures and their crystal structures were determined by powder and single-crystal X-ray diffraction. These arsenides include:  $RE_{1-y}Mn_xZn_{2-x}As_2$  ( $RE = \text{Eu-Lu}$ ) and  $RE_{2-y}Mn_xZn_{4-x}As_4$  ( $RE = \text{La-Nd, Sm, Gd}$ ) (Chapter 2);  $RE_4Mn_2As_5$  ( $RE = \text{La-Pr}$ ) (Chapter 3); and  $RE_{4-y}Zn_4As_6$  ( $RE = \text{La-Nd}$ ),  $RE_{5-y}Zn_4As_7$  ( $RE = \text{Pr, Nd, Sm, Gd}$ ), and  $RE_{6-y}Zn_4As_8$  ( $RE = \text{La-Nd, Sm, Gd}$ ) belonging to a homologous series  $RE_{2-y}Zn_4As_{4+n}(REAs)$  ( $n = 2, 3, 4$ ) (Chapter 4). They adopt similar crystal structures related to the  $CaAl_2Si_2$ -type, in accordance with predictions. Band structure calculations of representative members of these series were performed by tight-binding linear muffin tin method to determine electronic structures and to rationalize bonding. Metal site deficiencies were found in the series  $RE_{1-y}Mn_xZn_{2-x}As_2$ ,  $RE_{2-y}Mn_xZn_{4-x}As_4$ , and  $RE_{2-y}Zn_4As_{4+n}(REAs)$  to form charge balanced compounds, whereas the presence of extra electrons in the series  $RE_4Mn_2As_5$  can be rationalized by the metallic behavior or no band gap at the Fermi level. The effect of Mn atoms on the electronic structure of  $RE_{2-y}Mn_xZn_{4-x}As_4$  and  $RE_4Mn_2As_5$  compounds was analyzed by spin-polarized calculations.

## Preface

The thesis describes my research in the laboratory of Dr. Arthur Mar from September 2012 to December 2016 (leave period of 16 months, May 2015-August 2016) toward my Master degree under the title “New Ternary and Quaternary Layered Arsenides.” The following parts provide information of my contributions and co-authors in the subsequent chapters which were already published in different journals.

Chapter 2 contains published work, reported by Lin, X.; Tabassum, D.; Rudyk, B. W.; Mar, A. “Manganese-Substituted Rare-Earth Zinc Arsenides  $RE_{1-y}Mn_xZn_{2-x}As_2$  ( $RE = \text{Eu-Lu}$ ) and  $RE_{2-y}Mn_xZn_{4-x}As_4$  ( $RE = \text{La-Nd, Sm, Gd}$ ),” *Inorg. Chem.* **2014**, *53*, 8431–8441. I assisted Dr. Xinsong Lin in the synthesis and characterization, Dr. Xinsong Lin wrote the draft, Brent W. Rudyk did the XPS analysis, and composition and submission processes were completed by supervisory author Dr. Arthur Mar.

Chapter 3 contains published work, reported by Tabassum, D.; Lin, X.; Mar, A. “Rare-earth manganese arsenides  $RE_4Mn_2As_5$  ( $RE = \text{La-Pr}$ ).” *J. Alloys Comp.* **2015**, *636*, 187–190. I did synthesis, optimization of synthesis condition, data collection and analysis, characterization; and wrote draft, Dr. Lin assisted me during data collection and characterization; and Dr. Mar contributed to compose and submit the article.

Chapter 4 contains published work, reported by Lin, X.; Tabassum, D.; Mar, A. “Narrowing the gap: From semiconductor to semimetal in the homologous series of rare-earth zinc arsenides  $RE_{2-y}Zn_4As_4 \cdot n(REAs)$  and Mn-substituted derivatives  $RE_{2-y}Mn_xZn_{4-x}As_4 \cdot n(REAs)$  ( $RE = \text{La-Nd, Sm, Gd}$ ).” *Dalton Trans.* **2015**, *44*, 20254-20264. I did synthesis and crystal growth, data collection, characterization of rare-earth zinc arsenides  $RE_{2-y}Zn_4As_4 \cdot n(REAs)$ , homogeneity range reaction of

$RE_{2-y}Mn_xZn_{4-x}As_4 \cdot n(REAs)$  ( $RE = La-Nd, Sm, Gd$ ) for Mn whereas Dr. Lin did synthesis and crystal growth, data collection, characterization of Mn-substituted derivatives  $RE_{2-y}Mn_xZn_{4-x}As_4 \cdot n(REAs)$  ( $RE = La-Nd, Sm, Gd$ ), assisted me during characterization of  $RE_{2-y}Zn_4As_4 \cdot n(REAs)$  and wrote draft; and Dr. Mar involved in composition and submission of the article.

## **Acknowledgement**

I spent a wonderful time at the Department of Chemistry, University of Alberta, during my study where I got the privilege to come across with some very excellent people who shape me with their experiences, knowledge and guidance.

First of all, I would like to thank Professor Dr. Arthur Mar for giving me an opportunity to conduct research under his supervision and providing me necessary guidance whenever I needed. I am also very grateful to him for his critical questioning and encouraging comments during the discussions throughout my research which help me to think about the research materials more deeply. I am also thankful to Dr. Jillian Buriak, and Dr. Yunjie Xu for being a part of my supervisory committee and spending their valuable time for taking necessary steps for the completion of my study, reviewing my research progress, and giving guidance, if needed. I am very grateful to Dr. John Klassen, Dr. Jillian Buriak, Dr. Eric Rivard and Dr. Yunjie Xu for their wonderful theory classes which help me to adapt with a new education system compared to back home. I am also thankful to Dr. Mariusz Klobukowski for giving consent to be the armlength examiner for my defence.

I wish to thank Dr. Norman Gee, my TA supervisor, for his cooperative, friendly, and constructive supervision which help me to learn some professional as well as interpersonal skills. His flexibility during scheduling TA duties, funny stories during TA meeting, and encouraging prizes at the end of each term for best TAs simply amazed me. I am also grateful to other TA supervisor for whom I did proctoring and marking because of their mentoring and guidance to perform my duties flawlessly equipped me with some important skills, for example, decision making, punctuality, organization skill and so on.

I am also thankful to my group mates, Dr. Xinsong Lin, who helped me with most of my projects, Krishna, Mansura, Abishek, Anton, Wenglong, Brent, Dong for their support and help on various issues on everyday life that I faced. I would like to appreciate Dr. Robert McDonald for his assistance during single crystal data collection; and Dr. Michael Ferguson for his assistance especially updates about EDX, SEM and powder XRD.

Last, but certainly not least, I would like to appreciate the contribution of my parents (including in-laws) and family members. Special thanks go to my mother, late Saleha Khatun, who encouraged me in my every step from the very beginning of my life to do study sincerely; my husband, Md. Joynal Abedin, who supported me a lot with a smiley face whenever I got very busy during my exams and/ other responsibilities, just an incredible life partner; my son, Nazib and daughter, Jeanan, whose innocent faces gave me energy to perform my duties perfectly and effectively, though with a guilt of feeling not giving them enough time.

# Table of Contents

ABSTRACT.....	ii
PREFACE.....	iii
ACKNOWLEDGEMENT.....	v
<b>Chapter 1 Introduction .....</b>	<b>1</b>
1.1 Solid State Compounds.....	1
1.2 Metal Arsenides .....	2
1.3 Layered Structures, Polytypes, and Homologous Series .....	3
1.4 Bonding.....	5
1.5 Synthesis .....	10
1.6 Characterization .....	11
1.6.1 X-Ray Diffraction .....	11
<i>1.6.1.1 Powder X-ray Diffraction .....</i>	<i>12</i>
<i>1.6.1.2 Single-Crystal X-ray Diffraction.....</i>	<i>14</i>
1.6.2 Energy Dispersive X-ray (EDX) Analysis.....	16
1.7 Band Structure Calculations .....	17
1.8 Target Physical Properties during Project Design .....	23
1.8.1 Superconductivity in Layered Structures.....	23
1.8.2 Dilute Magnetic Semiconductors.....	24
1.8.3 Thermoelectricity .....	25
1.9 Motivation and Objective .....	26
1.10 References.....	27

## Chapter 2 Manganese-Substituted Rare-Earth Zinc Arsenides

$RE_{1-y}Mn_xZn_{2-x}As_2$  ( $RE = \text{Eu-Lu}$ ) and  $RE_{2-y}Mn_xZn_{4-x}As_4$  ( $RE = \text{La-Nd, Sm,}$

**Gd)** ..... **32**

2.1 Introduction.....	32
2.2 Experimental Section.....	35
2.2.1 Synthesis.....	35
2.2.2 Structure Determination.....	36
2.2.3 Band Structure Calculation.....	48
2.2.4 XPS Analysis.....	49
2.3 Results and Discussion.....	50
2.4 Conclusions.....	64

## Chapter 3 Rare-earth manganese arsenides $RE_4Mn_2As_5$ ( $RE = \text{La-Pr}$ ) ..... **72**

3.1 Introduction.....	72
3.2 Experimental.....	73
3.2.1 Synthesis.....	73
3.2.2 Structure determination.....	75
3.2.3 Band structure calculations.....	79
3.3 Results and discussion.....	79
3.4 Conclusions.....	83
3.5 References.....	85

## Chapter 4 Narrowing the gap: From semiconductor to semimetal in the homologous series of rare-earth zinc arsenides $RE_{2-y}Zn_4As_4 \cdot n(REAs)$ and

<b>Mn-substituted derivatives <math>RE_{2-y}Mn_xZn_{4-x}As_4 \cdot n(REAs)</math> (<math>RE = La-Nd, Sm,</math></b>	
<b>Gd) .....</b>	<b>87</b>
4.1 Introduction.....	87
4.2 Experimental.....	89
4.2.1 Synthesis .....	89
4.2.2 Structure determination.....	91
4.2.3 Band structure calculations.....	97
4.2.4 Results and discussion .....	97
4.3 Conclusions.....	113
4.4 References.....	115
<b>Chapter 5 Conclusions.....</b>	<b>117</b>
5.1 Conclusions.....	117
5.1.1 Reported projects .....	117
5.1.2 Current Projects .....	119
5.1.3 Future Work .....	120
5.2 References.....	122
<b>Bibliography .....</b>	<b>123</b>
<b>Appendix 1.....</b>	<b>134</b>
<b>Appendix 2.....</b>	<b>144</b>

## List of Tables

<b>Table 1.1</b> Reported ternary and quaternary arsenides. ....	9
<b>Table 2.1</b> Crystallographic Data for $RE_{1-y}Mn_xZn_{2-x}As_2$ ( $RE = Eu-Lu$ ). ....	41
<b>Table 2.2</b> Crystallographic Data for $RE_{2-y}Mn_xZn_{4-x}As_4$ ( $RE = La-Nd, Sm, Gd$ ). ....	42
<b>Table 2.3</b> Atomic Coordinates and Equivalent Isotropic Displacement Parameters ( $\text{\AA}^2$ ) for $RE_{1-y}Mn_xZn_{2-x}As_2$ ( $RE = Eu-Lu$ ). ....	43
<b>Table 2.4</b> Atomic Coordinates and Equivalent Isotropic Displacement Parameters ( $\text{\AA}^2$ ) for $RE_{2-y}Mn_xZn_{4-x}As_4$ ( $RE = La-Nd, Sm, Gd$ ). ....	45
<b>Table 2.5</b> Interatomic Distances ( $\text{\AA}$ ) for $RE_{1-y}Mn_xZn_{2-x}As_2$ ( $RE = Eu-Lu$ ). ....	47
<b>Table 2.6</b> Interatomic Distances ( $\text{\AA}$ ) for $RE_{2-y}Mn_xZn_{4-x}As_4$ ( $RE = La-Nd, Sm, Gd$ ). ....	48
<b>Table 3.1</b> Cell parameters for $RE_4Mn_2As_5$ ( $RE = La-Pr$ ) .....	74
<b>Table 3.2</b> Crystallographic data for $RE_4Mn_2As_5$ ( $RE = La, Pr$ ). ....	77
<b>Table 3.3</b> Atomic coordinates and equivalent isotropic displacement parameters for $RE_4Mn_2As_5$ ( $RE = La, Pr$ ). ....	78
<b>Table 3.4</b> Interatomic distances ( $\text{\AA}$ ) for $RE_4Mn_2As_5$ ( $RE = La, Pr$ ). ....	78
<b>Table 4.1</b> Cell parameters for $RE_{2-y}Zn_4As_4 \cdot n(REAs)$ ( $n = 2, 3, 4$ ) in powder samples obtained by reaction of the elements at 750 °C. ....	90
<b>Table 4.2</b> Abbreviated crystallographic data for $RE_{2-y}Mn_xZn_{4-x}As_4 \cdot n(REAs)$ ( $n = 2, 3, 4$ ). .....	94
<b>Table 4.3</b> Ranges of interatomic distances ( $\text{\AA}$ ) for $RE_{2-y}Mn_xZn_{4-x}As_4 \cdot n(REAs)$ ( $n = 2, 3,$ 4). ....	96
<b>Table 4.4</b> Observed and predicted members of homologous series $RE_{2-y}M_4As_4 \cdot n(REAs)$ . .....	104

<b>Table A 2.1</b> EDX analyses of $RE_{2-y}Mn_xZn_{4-x}As_4 \cdot n(REAs)$ ( $RE = La-Nd, Sm, Gd; n = 2, 3, 4$ ) crystals. ....	147
<b>Table A 2.2</b> Crystallographic data for $RE_{2-y}Mn_xZn_{4-x}As_4 \cdot n(REAs)$ ( $n = 2, 3, 4$ ).....	148
<b>Table A 2.3</b> Atomic coordinates and equivalent isotropic displacement parameters for $RE_{2-y}Mn_xZn_{4-x}As_4 \cdot n(REAs)$ ( $n = 2, 3, 4$ ). ....	149
<b>Table A 2.4</b> Interatomic distances ( $\text{\AA}$ ) for $RE_{2-y}Mn_xZn_{4-x}As_4 \cdot n(REAs)$ ( $n = 2, 3, 4$ ).....	152

## List of Figures

<b>Figure 1.1</b> Layered structures of (a) MoS <sub>2</sub> and (b) LaFeAsO.....	4
<b>Figure 1.2</b> Polyionic square net of As in the Zintl phases, (a) REZn <sub>0.67</sub> As <sub>2</sub> and (b) REZn <sub>2</sub> As <sub>3</sub> .....	7
<b>Figure 1.3</b> Structure of (a) CeFeAs (double RE layer) and (b) EuMn <sub>2</sub> As <sub>2</sub> (one RE layer).	8
<b>Figure 1.4</b> Different steps of synthesis.....	11
<b>Figure 1.5</b> Diffraction of X-ray (Bragg's law).....	12
<b>Figure 1.6</b> Phase identification in powder X-ray diffraction. ....	13
<b>Figure 1.7</b> Intensity pattern collected from single crystal X-ray diffraction. ....	15
<b>Figure 1.8</b> Schematic representation of EDX process. ....	17
<b>Figure 1.9</b> Band structure: (a) free electron system; (b) extended form and (c) reduced form under potential. ....	18
<b>Figure 1.10</b> Band structure based on LCAO and Bloch theorem. ....	20
<b>Figure 1.11</b> Band structure calculations for LaZn <sub>0.67</sub> As <sub>2</sub> . ....	22
<b>Figure 1.12</b> Layered structure of superconductor, BaFe <sub>2</sub> As <sub>2</sub> and thermoelectric, Bi <sub>2</sub> (SeTe) <sub>3</sub> .....	25
<b>Figure 2.1</b> The <i>0kl</i> nets for crystals of (a) Gd <sub>1-y</sub> Mn <sub>x</sub> Zn <sub>2-x</sub> As <sub>2</sub> and (b) Gd <sub>2-y</sub> Mn <sub>x</sub> Zn <sub>4-x</sub> As <sub>4</sub> . ....	39
<b>Figure 2.2</b> Plots of cell parameters for REMn <sub>0.5</sub> Zn <sub>1.5</sub> As <sub>2</sub> (RE = Eu, Yb), RE <sub>0.5</sub> Mn <sub>0.4</sub> Zn <sub>1.6</sub> As <sub>2</sub> (RE = Gd–Tm, Lu), and RE <sub>1.3</sub> Mn <sub>0.9</sub> Zn <sub>3.1</sub> As <sub>4</sub> (RE = La–Nd, Sm, Gd). ....	52
<b>Figure 2.3</b> (a) REMn <sub>0.4</sub> Zn <sub>1.6</sub> As <sub>2</sub> (RE = Eu, Yb) with CaAl <sub>2</sub> Si <sub>2</sub> -type structure, (b) RE <sub>0.5</sub> Mn <sub>0.4</sub> Zn <sub>1.6</sub> As <sub>2</sub> (RE = Gd–Tm, Lu) with defect CaAl <sub>2</sub> Si <sub>2</sub> -type structure,	

and (c)  $RE_{1.3}Mn_{0.9}Zn_{3.1}As_4$  ( $RE = La-Nd, Sm, Gd$ ) with partially ordered defect  $CaAl_2Si_2$ -type structure; all contain  $[M_2As_2]$  slabs alternately stacked with nets of  $RE$  atoms. The  $RE$  sites are either fully (dark blue) or partially occupied (faded blue). The interstitial Mn sites are partially occupied (faded blue-green). The Zn sites in (b) and the Zn1 sites in (c) are partially occupied (green). ..... 54

**Figure 2.4** Lengths (Å) of rib and handle bonds within metal-centred tetrahedra in  $EuMn_2As_2$  (left),  $EuMn_{0.4}Zn_{1.6}As_2$  (centre), and  $EuZn_2As_2$  (right). ..... 55

**Figure 2.5** Possible  $\sqrt{3}a \times \sqrt{3}a$  superstructure (with unit cell outlined in dashed lines) for idealized model “ $La_{1.33}MnZn_3As_4$ ” containing ordered occupation of 33% La, 50% Mn, and 50% Zn1 sites. .... 59

**Figure 2.6** (a) Density of states (DOS) and its atomic projections for “ $La_{1.33}MnZn_3As_4$ ”. (b) Crystal orbital Hamilton population (COHP) curves for La–As, Mn–As, and Zn–As interactions. The Fermi level is at 0 eV. .... 60

**Figure 2.7** DOS curve for spin-polarized “ $La_{1.33}MnZn_3As_4$ ”, with contributions from Mn states identified by the shaded regions. .... 61

**Figure 2.8** (a) Yb 4d XPS spectra for  $YbMn_{0.3}Zn_{1.7}As_2$  and  $Yb_2O_3$ . (b) Mn 2p XPS spectra for  $YbMn_{0.3}Zn_{1.7}As_2$ ,  $Nd_{1.2}Mn_{1.0}Zn_{3.0}As_4$ , and  $Er_{0.5}Mn_{0.4}Zn_{1.6}As_2$ . The components marked A–C are discussed in the text. .... 63

**Figure 3.1** Structure of  $RE_4Mn_2As_5$  ( $RE = La-Pr$ ) built up of slabs of  $RE$ -centred octahedra (yellow) and Mn-centred tetrahedra (green). The stacking sequence of As atoms in close-packed layers is noted. .... 80

<b>Figure 3.2</b> (a) Density of states (DOS) and its atomic projections for $\text{La}_4\text{Mn}_2\text{As}_5$ . (b) Crystal orbital Hamilton population (–COHP) curves for La–As and Mn–As interactions. ....	81
<b>Figure 3.3</b> DOS curve for spin-polarized $\text{La}_4\text{Mn}_2\text{As}_5$ in a hypothetical ferromagnetic model, with contributions from Mn atoms shown by shaded region. ....	82
<b>Figure 4.1</b> (a) Plots of cell volume per formula unit for different RE members of the three series $\text{RE}_{4-y}\text{Zn}_4\text{As}_6$ , $\text{RE}_{5-y}\text{Zn}_4\text{As}_7$ , and $\text{RE}_{6-y}\text{Zn}_4\text{As}_8$ . (b) Plots of cell lengths as a function of $n$ in the homologous series $\text{RE}_{2-y}\text{Zn}_4\text{As}_4 \cdot n(\text{REAs})$ . The c-parameters are normalized by dividing by 3 for structures in space group...	99
<b>Figure 4.2</b> (a) A fragment of the structure of $\text{RE}_{4-y}\text{M}_4\text{As}_6$ , the $n = 2$ member of $\text{RE}_{2-y}\text{M}_4\text{As}_4 \cdot n(\text{REAs})$ ( $M = \text{Mn}, \text{Zn}$ ). The RE2 sites (lightly shaded) are partially occupied at 0.3–0.4. Mn and Zn atoms are found in a set of split M1a (primary, with occupancy of 0.7–0.8, preferred by Zn) and M1b sites (secondary, with occupancy of 0.2–0.3, preferred by Mn), or in the unsplit M2 sites (preferred by Zn). (b) Local coordination within the $[\text{M}_2\text{As}_2]$ slab is either tetrahedral geometry exhibited by M1b sites or octahedral geometry by RE2 sites, with M1a sites in adjacent slabs. ....	100
<b>Figure 4.3</b> Full structure of $\text{RE}_{4-y}\text{M}_4\text{As}_6$ , with unit cell outlined, in (a) ball-and-stick and (b) polyhedral representations, showing the intergrowth of $[\text{REAs}]$ slabs built from edge-sharing octahedra and $[\text{M}_2\text{As}_2]$ slabs built from edge-sharing tetrahedra. ....	102

- Figure 4.4** Structures of the  $n = 0, 2, 3,$  and  $4$  members of the homologous series  $RE_{2y}M_4As_4 \cdot n(REAs)$  in terms of  $[REAs]$  slabs (yellow) and  $[M_2As_2]$  slabs (green). The stacking sequences of As nets are also marked. .... 103
- Figure 4.5** Starting from the same parent member  $REM_2As_2$  (or  $RE_2M_4As_4$ ), inserting additional  $[REAs]$  slabs leads to either the metal-deficient homologous series  $REM_{2-x}As_2 \cdot n(REAs)$  (left) and the rare-earth-deficient homologous series  $RE_{2-y}M_4As_4 \cdot n(REAs)$  (right). Hypothetical structures have their formulas shown in parentheses. .... 105
- Figure 4.6** (a) Density of states (DOS) and (b) crystal orbital Hamilton population (–COHP) curves for idealized fully stoichiometric model  $La_4Zn_4As_6$ . Removal of two electrons per formula unit lowers the Fermi level from 0 eV (solid line) to the gap at –1 eV (dashed line). .... 109
- Figure 4.7** DOS curves for several members of homologous series  $La_2Zn_4As_4 \cdot n(LaAs)$  based on real, rare-earth-deficient compounds ( $n = 0, 2, 3, 4$ ), hypothetical models ( $n = 1, 5$ ), and the limiting extreme of  $LaAs$  ( $n = \infty$ ). Regions shaded in green represent projections of states originating from  $[Zn_2As_2]$  slabs; the remaining regions shaded in yellow are states originating from  $[LaAs]$  slabs. Removal of two electrons per formula unit lowers the Fermi level to energies indicated by the dashed lines. .... 111
- Figure A 1.1** Powder XRD patterns for  $RE_{1-y}Mn_xZn_{2-x}As_2$  ( $RE = Eu-Lu$ ). Unidentified peaks are marked with asterisks. .... 134
- Figure A 1.2** Powder XRD patterns for  $RE_{2-y}Mn_xZn_{4-x}As_4$  ( $RE = La-Nd, Sm, Gd$ ). Unidentified peaks are marked with asterisks. Observed  $(00l)$  peaks are more

intense than expected because of preferred orientation (e.g., the (005) peaks are marked).....	135
<b>Figure A 1.3</b> (a) Elemental maps and (b) EDX spectrum for $\text{Nd}_{2-y}\text{Mn}_x\text{Zn}_{4-x}\text{As}_4$ .....	136
<b>Figure A 1.4</b> Powder XRD patterns for products from loading compositions “ $\text{Gd}_{0.67}\text{Mn}_x\text{Zn}_{2-x}\text{As}_2$ ” (lower panels), compared with simulated patterns for $\text{Gd}_{1-y}\text{Mn}_x\text{Zn}_{2-x}\text{As}_2$ and $\text{Gd}_{2-y}\text{Mn}_x\text{Zn}_{4-x}\text{As}_4$ (upper panels). Other phases present include various binary arsenides ( $\text{GdAs}$ , $\text{MnAs}$ , $\text{ZnAs}$ , $\text{ZnAs}_2$ , $\text{Zn}_3\text{As}_2$ ).....	137
<b>Figure A 2.1</b> Powder XRD patterns for $\text{RE}_{4-y}\text{Zn}_4\text{As}_6$ ( $\text{RE} = \text{La-Nd}$ ). .....	144
<b>Figure A 2.2</b> Powder XRD patterns for $\text{RE}_{5-y}\text{Zn}_4\text{As}_7$ ( $\text{RE} = \text{Pr, Nd, Sm, Gd}$ ).....	145
<b>Figure A 2.3</b> Powder XRD patterns for $\text{RE}_{6-y}\text{Zn}_4\text{As}_8$ ( $\text{RE} = \text{La-Nd, Sm, Gd}$ ).....	146

## List of Symbols and Abbreviations

$\alpha$	Thermal diffusivity
$\theta$	Angle of reflection
$\kappa$	Thermal conductivity
$\lambda$	Wavelength
$\rho$	Density
$\chi$	Electronegativity
$\mu$	Absorption coefficient
1D	One dimensional
2D	Two dimensional
3D	Three dimensional
$a b c \alpha \beta \gamma$	Unit cell parameters
ASA	Atomic spheres approximation
COOP	Crystal orbital overlap population
COHP	Crystal orbital Hamilton population
CN	Coordination number
$d_{hkl}$	Interplanar distance of a crystal
DFT	Density functional theory
DOS	Density of states
$e^-$	Electron
$E_F$	Fermi level
$E_g$	Band gap
EDX	Energy dispersive X-ray analysis
FWHM	Full-width-at-half-maximum
fm	Formula mass
f.u.	Formula unit
$hkl$	Miller indices
$k$	Wavevector
$l$	Angular orbital momentum
LDA	Local density approximation
LTMO	Linear muffin-tin orbital

<i>M</i>	Transition metal
<i>n</i>	Number of valence electron
<i>Pn</i>	Pnictides, pnictogens
<i>RE</i>	Rare-earth
<i>S</i>	Goodness of fit, scattering coefficient
SEM	Scanning electron microscope
T	Temperature
$T_c$	Critical temperature; Curie temperature
TB	Tight binding
<i>V</i>	Cell volume; applied voltage
VEC	Valence electron concentration
XRD	X-ray diffraction
XPS	X-ray photoelectron spectroscopy
Z	Atomic number; nuclear charge
$Z_{\text{eff}}$	Effective nuclear charge

# Chapter 1

## Introduction

### 1.1 Solid State Compounds

Crystalline solids can be broadly classified into two types: molecular solids containing discrete molecules held together by weak intermolecular forces (e.g. van der Waals forces), and extended solids containing atoms or ions held together by strong bonding forces (ionic, covalent, and metallic interactions). Extended inorganic solids exhibit a wide variety of crystal structures.<sup>1</sup> The study of these solids is interesting, exciting, and important, because there are endless possibilities for forming many compounds consisting of two or more elemental components, they exhibit a wide variety of structures (including many polymorphic forms) and properties, and these properties can be manipulated as required for the appropriate materials applications in technology.<sup>2</sup> The choice of which elements to combine depends on the desired property on which a particular investigation is focused. For example, in terms of electrical properties, metal oxides are generally insulators, many pnictides are semiconductors, and intermetallic compounds are conductors, because the types of bonding interactions dictate the electronic structure. The presence of transition elements often confers interesting magnetic properties as a result of interactions arising from unpaired electrons occupying d- or f-orbitals. My research focuses mainly on the synthesis, structure determination, and bonding of metal arsenides.

## 1.2 Metal Arsenides

Almost all metals (e.g., s-block, d-block, f-block, and p-block metals) combine with arsenic to form binary metal arsenides having one or composition.<sup>3</sup> Among them are many important direct band gap semiconductors such as II–V compounds ( $\text{Zn}_3\text{As}_2$ ,  $\text{Cd}_3\text{As}_2$ )<sup>4</sup> and III–V compounds (AlAs, GaAs, InAs).<sup>5,6</sup> MnAs has attracted attention because it exhibits ferromagnetism below 317 K, associated with a structural change.<sup>7</sup> The combination of semiconducting and ferromagnetic properties gives rise to the possibility of developing materials for *spintronics*, which could lead to further miniaturization of electronic devices.<sup>8</sup> The inherent properties of a material can be modified through the common strategies of doping and chemical substitution. Mn-doped III–V arsenides have been identified as promising materials for dilute magnetic semiconductors (DMS).<sup>9-11</sup> For example,  $\text{Mn}_x\text{Ga}_{1-x}\text{As}$  is a good candidate for a DMS material relative to other III–V compounds because of its intermediate band gap and high Curie temperature.<sup>12</sup> However, there remain significant challenges including solubility of Mn in optimizing  $\text{Mn}_x\text{Ga}_{1-x}\text{As}$  so that it can be used as a DMS material in practical applications. The search for alternative DMS materials is continuing.

In contrast to binary arsenides, which have been studied for the last 100 years, ternary, quaternary, and multinary arsenides have been identified more recently.<sup>13</sup> In particular, many new arsenides have been found to exhibit superconductivity, including LiFeAs (“111-type”),  $A\text{Fe}_2\text{As}_2$  ( $A$  = alkali and alkaline-earth metals; “122-type”), and  $RE\text{FeOAs}$  ( $RE$  = rare-earth metals; “1111-type”).<sup>14</sup> So far many compounds have been reported that are related to these superconducting materials.

Our research group is broadly interested in materials for potential applications as thermoelectrics, semiconductors, superconductors, and non-linear optics. A particularly rich area of investigation is the  $RE-Zn-As$  system, in which several new ternary phases have been discovered:  $REZn_{1-x}As_2$ ,<sup>15</sup>  $REZn_3As_3$ ,<sup>16</sup>  $REZn_2As_3$ ,<sup>17</sup> and  $REZn_{2-x}As_2 \cdot nREAs$  ( $n = 3-6$ ).<sup>18</sup> Many of these compounds are predicted to be semiconducting. The goal of my research is to further investigate these systems to identify other ternary arsenides, and to incorporate Mn in these compounds in hopes of conferring magnetic properties in these semiconductors.

### 1.3 Layered Structures, Polytypes, and Homologous Series

Inorganic solids adopting layered structures are interesting because their strong anisotropy leads to unusual physical properties and the ability to intercalate or deintercalate guest atoms between the layers offers the possibility of tuning these properties.<sup>19</sup> Well known layered materials include graphene,<sup>20</sup> SiC,<sup>21</sup> and MoS<sub>2</sub>,<sup>22</sup> in which the layers are held together by weak van der Waals forces and can easily be exfoliated. In other types of compounds with layered structures, the interlayer forces could be ionic or covalent bonding interactions, but these are still weaker than the intralayer forces. Many of the new arsenide superconductors could be regarded in this way; for example, LaFeAsO has been described as consisting of positively charged layers [LaO]<sup>+</sup> and negatively charged layers [FeAs]<sup>-</sup> are held together by ionic interactions.<sup>14</sup> **Figure 1.1** shows the structures of both types of layered compounds (e.g., MoS<sub>2</sub> and LaFeAsO)

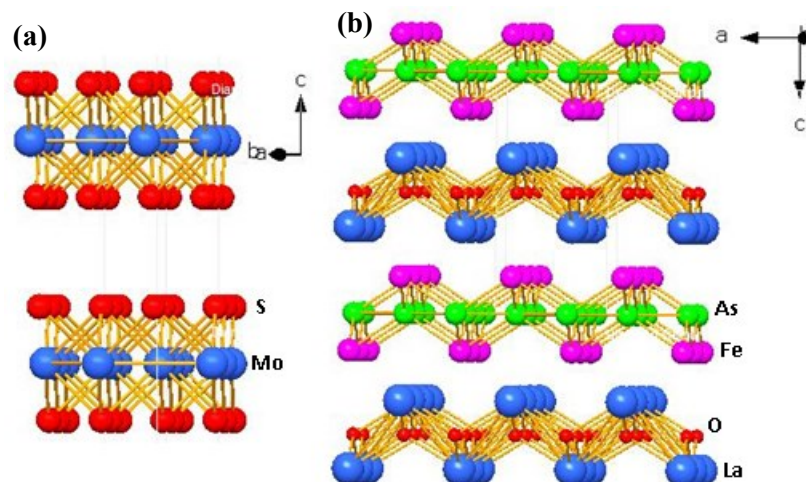


**Figure 1.1** Layered structures of (a) MoS<sub>2</sub> and (b) LaFeAsO.

Many layered compounds exhibit a phenomenon called *polytypism*.<sup>23</sup> As an early example, SiC was recognized by Baumhauer at the beginning of the 20th century to exist as several polytypes.<sup>23</sup> Polytypic structures typically have two dimensions that are similar and a third dimension that is different, along which stacking occurs; these crystalline modifications have definite composition and can be expressed as integral multiples of basic units. To describe the stacking sequence in polytypes, Ramsdel notation (such as 2H, 3C, and 6H) indicates the number of repeating layers in the unit cell and the crystal system (H for hexagonal, C for cubic). Polytypism is a special kind of polymorphism, in terms of energy differences. The potential energy differences among different polytypes are quite small, and the formation of a preferred polytype depends on factors such as temperature, presence of impurities, initial composition, structural distortion, and supersaturation.<sup>24</sup>

Polytypes that are built up from a structural module and can be expressed by a common structural formula are known as *homologous series*. The concept of homologous series pervades other areas of chemistry (e.g., the alkanes C<sub>n</sub>H<sub>2n+2</sub> form a

simple homologous series in organic chemistry), and was first used in solid state chemistry by Magneli to define a series of transition metal oxide under general formula  $M_nO_{3n-1}$  ( $M=Mo, W$ )<sup>25</sup> and later used for different types of oxide series commonly known as perovskites (e.g., Ruddlesden-Popper series,  $A_{n+1}B_nO_{3n+1}$ ; Dion-Jacobson series,  $A_nB_nO_{3n+1}$ ; Aurivillius series,  $Bi_2A_{n-1}B_nO_{3n+3}$ , where A, B = metals with same or different charges), for some mineral sulfosalts (e.g., lillianite series,  $Pb_{N-1-2x}Bi_{2+x}Ag_xS_{N+2}$ , where  $N = (N1 + N2)/2$ ,  $N1$  and  $N2$  equals to the number of metal sites in the alternating slabs,  $x$ =substitution coefficients for  $Bi+Ag = 2Pb$ ;  $N1+N2L = 4,7L = Pb_8Ag_5Bi_{13}S_{30}$ ).<sup>26-31</sup> Recently, it has been investigated as an opportunity to design new compounds in solid state chemistry, which is a more difficult task because there is little synthetic control under the conditions of high-temperature reactions.<sup>32</sup> Successful examples includes chalcogenides (e.g.,  $A_m[M_6Se_8]_m[M_{5+n}Se_{9+n}]$ ,  $A_m[M_{1+l}Se_{2+l}]_{2m}[M_{1+2l+n}Se_{2+3l+n}]$  where  $A=K, Rb, Cs, Sr, Ba$ ;  $M= Sn, Pb$ ),  $Cs_4[Bi_{2n+4}Te_{3n+6}]$  and pnictides (e.g.,  $[Sb_2Te_3]_m \cdot [Sb]_n$ ).<sup>32,33</sup> Among arsenides, the compounds  $REZn_{2-x}As_{2 \cdot n}REAs$  ( $n = 3-6$ ) reported by Mar et al. appear to establish a homologous series.<sup>18</sup>

In the present work, we seek to identify new ternary and quaternary arsenides that are built up of similar types of layers but have different stacking sequences, which satisfy the definition of polytypism.

#### 1.4 Bonding

The type of bonding in solids depends on the electronegativities of atoms combined together. However, complex solids can contain more than one type of bond (ionic, covalent, metallic), which can be of intermediate character.<sup>34</sup> The bonding present in a solid dictates the physical properties (e.g., electrical and optical properties). Based

on electrical properties, inorganic solids can be classified roughly into three categories. At one extreme, electrical insulators are usually found among salt-like compounds in which a large difference in electronegativity leads to full electron transfer and the formation of isolated cations and anions, each attaining an octet according to the Lewis concept.<sup>35</sup> At the other extreme, electrical conductors are found in metallic solids and intermetallic compounds (formed from combinations of two or more metals). For some metallic solids, the formation is guided by considerations of electronegativity, atomic size, and number of valence electrons. However, there are no simple rules or concepts that can explain the formation of all intermetallic compounds because of their diversity of structure and bonding.<sup>36,37</sup> Intermediate in character are semiconductors, which have important applications in technology. Although many inorganic solids (e.g., chalcogenides) are semiconducting, we focus on a particular class of compounds called *Zintl phases*.<sup>38,39</sup> These are compounds consisting of an electropositive element in combination with a post-transition metal, semimetal, or metalloid; interestingly, their structures can be understood in terms of a complete electron transfer from the electropositive to the electronegative elements so that the octet rule is followed. In other words, they are intermetallic compounds whose bonding can be rationalized as if they were ionic compounds; the bonding could be described as “polar metallic,” in analogy to “polar covalent” when mixed covalent-ionic character is present. Typically, the electropositive element is an alkali or alkaline-earth metal, which loses its valence electrons to form an isolated cation. However, some compounds containing rare-earth metals (e.g., CeAs<sub>5</sub>, LaAs<sub>2</sub>, NdP<sub>2</sub>) could be considered to be Zintl phases.<sup>40</sup> The

electronegative element may form additional homoatomic bonds to form a polyanionic substructure that follows the octet ( $8-N$ ) rule.<sup>35,41</sup>

The Zintl concept helps rationalize the bonding in many ternary and quaternary arsenides ( $RE-M-As$  and  $RE-M-M'-As$ ), whose numbers have risen dramatically over the last few years. The arsenides  $REMA_s_2$  adopting a tetragonal  $HfCuSi_2$ -type structure form for many monovalent ( $M = Cu, Ag, Au$ )<sup>42,43</sup> and divalent transition metals ( $M = Zn, Cd$  (not published)) in combination with trivalent  $RE$  metals.<sup>15</sup> The latter typically exhibit nonstoichiometry with partially occupied  $M$  sites.

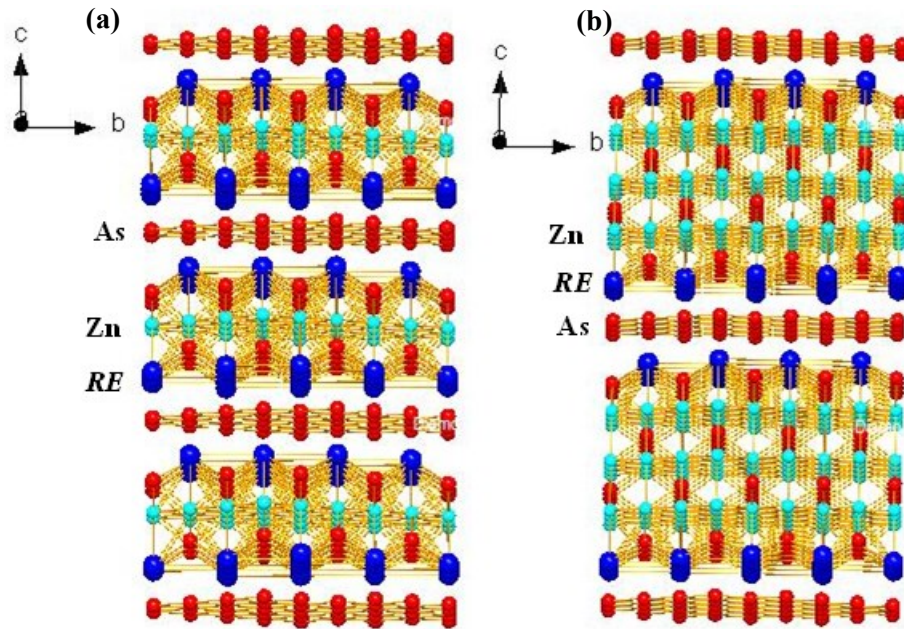


**Figure 1.2** Polyionic square net of As in the Zintl phases, (a)  $REZn_{0.67}As_2$  and (b)  $REZn_2As_3$ .

For example, in substoichiometric  $REZn_{0.67}As_2$ , the formulation  $(RE^{3+})(Zn^{2+})_{0.67}(As^{3-})(As^{1.33-})$  is consistent with the presence of tetrahedral slabs  $[Zn_2As_2]^{2-}$  containing isolated As atoms ( $As^{3-}$ ) and polyanionic square nets containing As atoms in homoatomic bonds ( $As^{1.33-}$ ).<sup>15</sup> In  $REZn_2As_3$ , a thicker anionic slab  $[Zn_{3-x}As_2]$

and similar square nets are also present (**Figure 1.2**).<sup>17</sup> Other ternary *RE–Zn–As* phases conform to the Zintl concept:  $(RE^{3+})(Zn^{2+})_3(As^{3-})_3$ ,<sup>16</sup>  $(RE^{3+})_{0.67}(Zn^{2+})_2(As^{3-})_2$ ,<sup>44</sup> and  $(RE^{3+})_4(Zn^{2+})_{2-x}(As^{3-})_{5+n}(RE^{3+})(As^{3-})$ .<sup>18</sup>

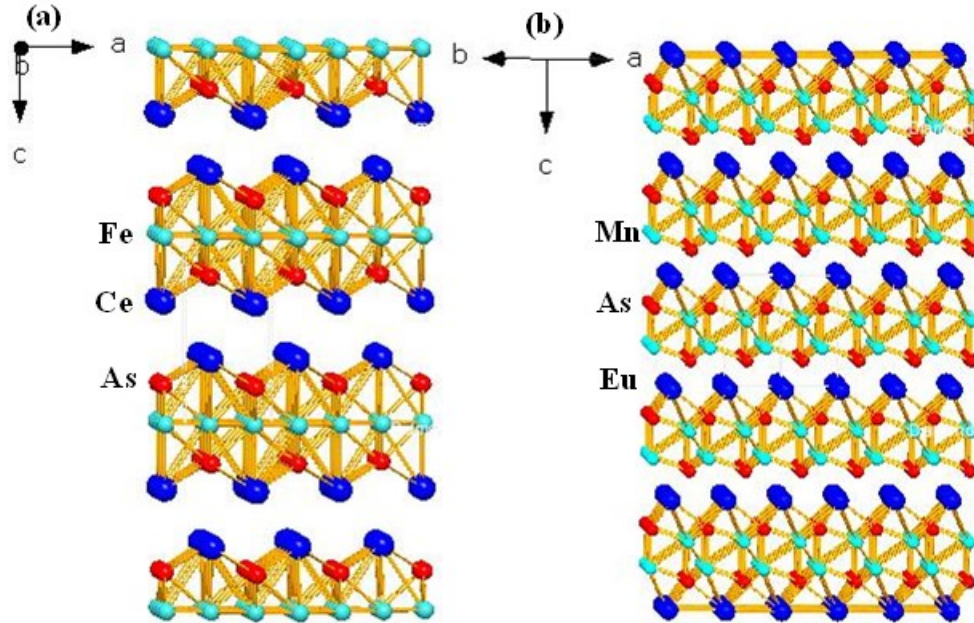


**Figure 1.3** Structure of (a) CeFeAs (double *RE* layer) and (b) EuMn<sub>2</sub>As<sub>2</sub> (one *RE* layer).

Divalent transition metals ( $M = Mn, Fe, Co, Ni, Ru, Rh, Ir, Pd, Zn, Cd, Pt$ ) form  $REM_2As_2$  phases in combination with bivalent and trivalent *RE* metals usually adopt tetragonal ThCr<sub>2</sub>Si<sub>2</sub> or trigonal CaAl<sub>2</sub>Si<sub>2</sub> types structures.<sup>45-48</sup> In case of ternary *RE*, partially occupied *RE* sites were observed.<sup>44</sup> Ternary  $AM_2As_2$  phases adopting the CaAl<sub>2</sub>Si<sub>2</sub>-type structure can be expanded to yield quaternary derivatives  $REMZnAs$  ( $M = Cu, Ag$ ) containing two different transition metals in place of one, and they can be rationalized by the formulation  $(RE^{3+})(M^{1+})(Zn^{2+})(As^{3-})_2$ .<sup>49</sup> Equiatomic *REMA*s phases are very common and found for many transition metals ( $M = Fe, Co, Ni, Cu, Rh, Pd, Ag, Pt$ , and others); they usually adopt closely related PbClF-, YPtAs-, BeZrSi-, and TiNiSi-type structures.<sup>3,50-52</sup> The compounds  $(Eu^{2+})(M^{1+})(As^{3-})$  containing monovalent metals

( $M = \text{Cu, Ag, Au}$ ) are electron-precise Zintl phases, whereas other compounds containing higher-valent metals exhibit metallic bonding. The structures of these two families of compounds (“111-type” and “122-type”) differ only in the number of transition-metal layers (**Figure 1.3**).

Less numerous are some metal-rich arsenides  $RE_2M_{12}As_7$  ( $M = \text{Co, Ni, Rh}$ ) and their quaternary variants  $RE_2(M,M')_{12}As_7$  ( $M,M' = \text{Co, Cr; W, Co; Mn, Cu}$ ).<sup>52-60</sup> Electronic structure calculations on  $RE_2Mn_3Cu_9As_{12}$  indicate metallic behavior.<sup>60</sup> Although the bonding in arsenide  $RE-M-As$  systems show transitions to increasing metallic character ( $REM_2As_2$  to  $REMA_s$  to  $RE_2M_{12}As_7$ ), there are also some other reported ternary arsenides  $RE-M-As$  and quaternary arsenides  $RE-M-M'-As$  as listed in the following table.

**Table 1.1** Reported ternary and quaternary arsenides.<sup>a,b</sup>

Transition Metal	Zintl Phase	Intermetallic
Mn	$Eu_{14}MnAs_{11}$	
Fe, Ru, Os	$REM_4As_{12}$ ( $M = \text{Fe, Ru, Os}$ )	$Ce_{12}Fe_{57.5}As_{41}$ , $RE_6Fe_{13}As$
Co, Rh, Ir	$Eu_4Ir_8As_7$ , $YbRh_6As_4$ , $Yb_4Rh_7As_6$ $Eu_3Rh_{15}As_{9.5}$	$RECo_5As_3$
Ni, Pd,	$Eu_3Pd_4As_4$	$RE_{10}Ni_{21}As_{15}$ , $RE_2NiAs_2$ , $RE_7Ni_{19}As_{13}$ , $RE_{13}Ni_{25}As_{19}$ , $RE_3Ni_7As_5$ , $RE_6Ni_{20}As_{13}$ , $RE_{10}Ni_{20}As_{15}$ , $RENi_4As_2$ , $RE_6Ni_{15}As_{10.5}$ $REPd_3As_2$
Cu, Ag	$RE_2Cu_4As_3$ ( $RE = \text{Eu, Yb}$ ), $EuAg_4As_2$	
Zn, Cd	$Eu_{11}Zn_6As_{12}$ , $Eu_2CdAs_2$ , $Eu_2Cd_2As_3$	

<sup>a</sup> $RE$ =Rare-earth element.

<sup>b</sup>Source of Compounds- Pearson’s Crystal Data.

## 1.5 Synthesis

Synthesis is an essential step not only for discovering new phases but also for processing existing phases in proper forms for applications. However, designing the synthesis of new solid state compounds is not straightforward or even possible in many cases, mainly because of a lack of understanding of mechanisms, which usually involves diffusion of atoms at high temperatures. Moreover, solid state compounds exhibit diverse types of composition, bonding, and structure, and can be complicated by features such as defects and vacancies.

In cases where compounds can be recognized to belong to a homologous series with a general formula, new compounds can be targeted by identifying potential members of this series and adjusting the modular structure.<sup>32,33</sup> In layered compounds, this corresponds to changing the number of layers. In addition, chemical substitution with other elements can always be attempted. Given the existence of a homologous series of arsenides  $REZn_{2-x}As_2 \cdot nREAs$  ( $n = 3-6$ ) containing variable thicknesses of  $REAs$  layers,<sup>18</sup> it seems reasonable to attempt syntheses of several new compounds derived from them. First, Mn can be substituted completely for Zn to result in Mn arsenides (**Chapter 3**). Second, close inspection of these structures suggests that a slight rearrangement of  $REAs$  layers may result in a different type of homologous series (**Chapter 4**). Third, we return to the simplest member  $RE_{0.67}Zn_2As_2$  and attempt partial substitution of Zn with Mn (**Chapter 2**).

All reactions were carried out at high temperatures starting from mixtures of the elements. The elements were combined in stoichiometric ratios, and pressed into pellets to increase surface contacts. To minimize the loss of volatile elements (Zn, As), the

reactions were performed at temperatures that were not too high (750 °C). Crystal growth was promoted by slow cooling to room temperature. Special precautions were taken to handle the reactants with appropriate protective gear given the toxicity of As and its compounds. Also, because *RE* and As tend to oxidize in air or moist air, they were handled inside a glove box. To minimize exposure to oxygen, the *RE* elements were freshly filed and As lumps were weighed quickly. The reactants were placed inside evacuated fused-silica tubes (**Figure 1.4**).

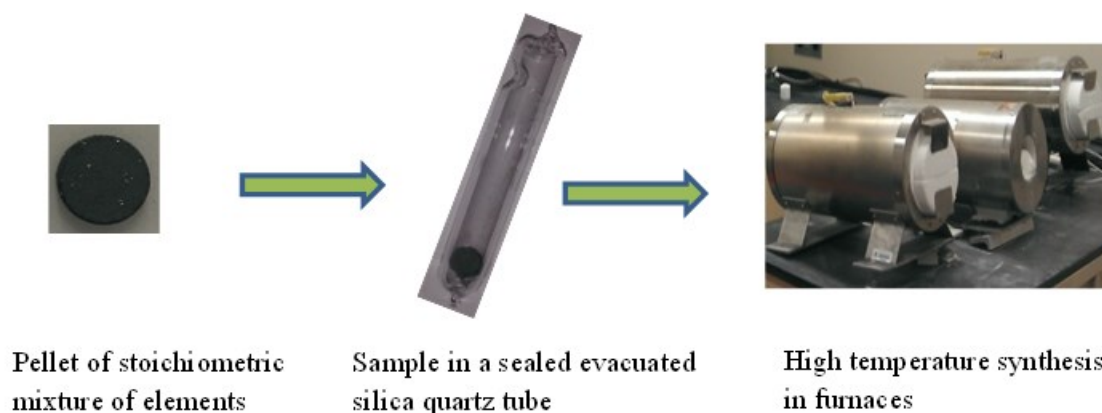


**Figure 1.4** Different steps of synthesis.

## 1.6 Characterization

### 1.6.1 X-Ray Diffraction

X-ray diffraction (XRD) provides a unique and characteristic pattern for each crystalline solid, depending on the atomic arrangement, so that it is an important nondestructive tool for both qualitative and quantitative analysis. XRD can be performed on either powder or single-crystal samples, depending on the quality of material and the type of information desired. Diffraction takes place as a result of constructive

interference of the X-rays impinging on the ordered arrangement of atoms within planes of a crystalline solid (Figure 1.5).

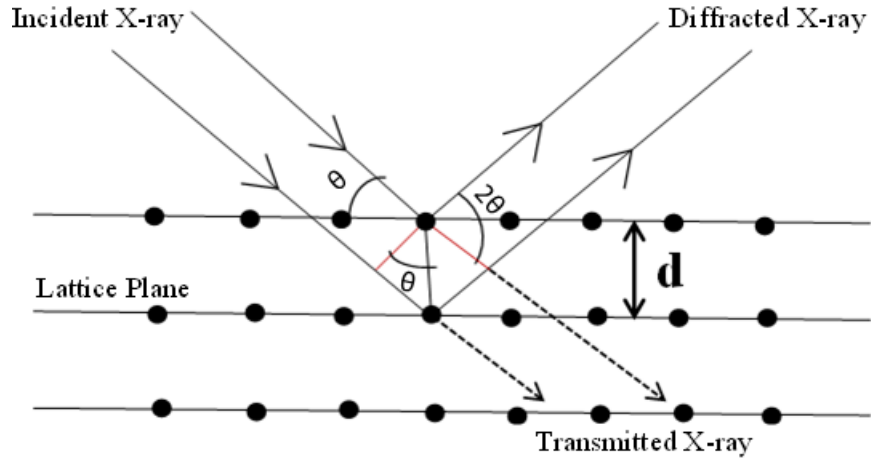


Figure 1.5 Diffraction of X-ray (Bragg's law).

If  $\lambda$  is the wavelength of incident X-ray beam,  $d$  is the interplanar distance for a group of planes ( $nh$ ,  $nk$ ,  $nl$ ) of the crystal, and  $\theta$  is diffraction angle, they are related through Bragg's law, which is the basic equation used in powder and single-crystal XRD analysis:

$$n\lambda = 2d_{hkl}\sin\theta \quad (1-1)$$

Bragg's law models the complex process of X-ray scattering through a simplified representation as "reflections" of X-rays.

### 1.6.1.1 Powder X-ray Diffraction

Powder XRD is used for various purposes, including identification of one or more phases (known or unknown) in a sample; calculation of interplanar distances, cell parameters, and crystallite sizes; and in more sophisticated cases, determination of crystal structure (through Rietveld refinement), defects, and strains. In this thesis, powder XRD

is used mainly for identifying phases, estimating the relative amounts of phases in sample, and examining the effects of substitution and doping on cell parameters.

The powder X-ray diffractometer used here consists of an X-ray source ( $\text{Cu } K\alpha_1$ ), a rotating sample holder, and a curved position sensitive (CPS) detector which collects the all scattered X-rays simultaneously from a sample as a function of  $2\theta$ , the angle between the transmitted and diffracted X-ray beams. Proper sample preparation is important in powder XRD analysis. The sample was ground to ensure a homogeneous fine powder so that crystallites are distributed in random orientations, thereby providing a reliable intensity pattern. The XRD patterns, which are plots of intensity versus  $2\theta$ , are converted to  $x-y$  files and plotted using the program PowderCell (version 2.4).<sup>61</sup> For phase identification, the experimental patterns are compared with simulated ones generated using information available in crystallographic databases (**Figure 1.6**). Once a desired phase is identified, its cell parameters are refined using the program UnitCell (WinCSD, version 2000).<sup>62</sup>

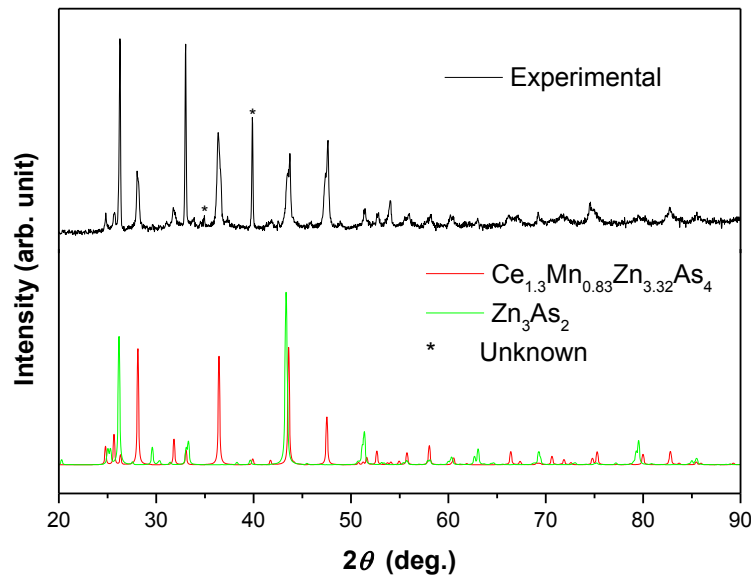


**Figure 1.6** Phase identification in powder X-ray diffraction.

### ***1.6.1.2 Single-Crystal X-ray Diffraction***

Single-crystal XRD is arguably the best method for complete determination of a crystal structure, which includes the unit cell parameters, space group, atomic positions, bond lengths, and other geometrical parameters.<sup>63</sup> In a typical procedure, a new phase is identified from the powder XRD analysis. An appropriate single crystal is then selected and its chemical composition verified by energy-dispersive X-ray (EDX) analysis on a scanning electron microscope. Normally, a crystal that shows smooth surfaces and suitable sizes (~0.5 mm) is chosen or cut from a bigger crystal. It is mounted on the tip of a glass fiber pin with help of epoxy glue and then placed on the sample holder of the goniometer in the X-ray diffractometer to collect diffraction data. A Bruker PLATFORM diffractometer, used here, consists of a Mo  $K\alpha$  X-ray source and a SMART APEX II CCD area detector. The mounted crystal is centered within the X-ray beam by adjusting its position as it is viewed through a video camera. A preliminary set of diffraction data, obtained after exposure to radiation for 30–60 minutes, is indexed to determine the cell parameters and to inspect the diffraction spots. If the cell parameters appear reasonable and the reflections appear sharp, the full set of intensities is collected using  $\omega$ -scans over 4–8 frames with widths of  $0.3^\circ$  and exposure times of 10–20 s per frame, depending on the size and quality of the crystal (**Figure 1.7**). It takes approximately 24 h to collect the whole data set. The faces and dimensions of the crystal are measured, in order to apply absorption corrections, which are essential for crystals containing many heavy elements, as is the case here. The intensity data are integrated using the program SAINT(version 8.34A ).

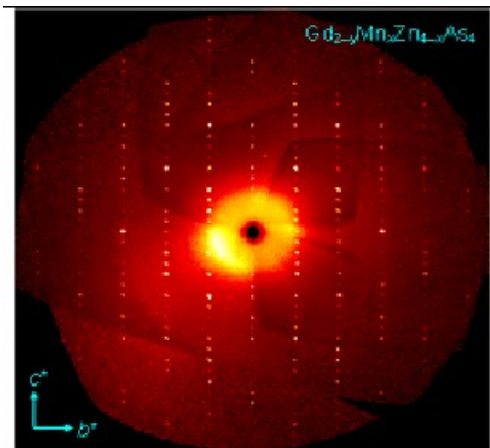


**Figure 1.7** Intensity pattern collected from single crystal X-ray diffraction.

The reflection intensities collected are related to the *structure factor*, which is a Fourier transform of the electron density function, as given by the following equations:

$$|F|^2 = I(K) \quad (1-2)$$

$$F(hkl) = \sum_{j=1}^N f_j \left[ \exp[2\pi i(hx_j + ky_j + lz_j)] \right] \quad (1-3)$$

$$\rho(x, y, z) = \frac{1}{v} \sum_h \sum_k \sum_l |F| \exp \left[ 2\pi i[(hx_j + ky_j + lz_j) - \varphi_{hkl}] \right] \quad (1-4)$$

The experimental intensities provide information about the magnitudes but not the phases of the structure factors. This inability to determine crystal structures directly from the diffraction data because of the absence of information about the phases is known as the phase problem.<sup>63</sup> The problem can be overcome with probabilistic methods (“direct methods”), as implemented in the SHELXTL software package (version 6.12),<sup>64</sup> which consists of several programs to solve and refine crystal structures. Although advances in crystallographic software have greatly accelerated structure determination, good chemical intuition is still needed to make judicious decisions, such as determining correct space groups, applying absorption corrections, assigning atoms in a particular site, and judging

geometrical parameters and vibrational motions. Agreement between the observed structure factors ( $F_o$ ) and calculated ones ( $F_c$ ) is evaluated by the following equations (where  $w$  is a weighting parameter introduced to account for statistical errors,  $n$  is the number of measured reflections, and  $p$  is the number of refined parameters) which define the weighted  $R$ -factor ( $wR_2$ ), the  $R$ -factor ( $R_1$ ), and the goodness of fit (GoF):

$$wR_2 = \left\{ \frac{\sum [w(F_o^2 - F_c^2)^2]}{\sum [w(F_o^2)^2]} \right\}^{1/2} \quad (1-5)$$

$$R_1 = \frac{\sum | |F_o| - |F_c| |}{\sum |F_o|} \quad (1-6)$$

$$GoF = S = \left\{ \frac{\sum [w(F_o^2 - F_c^2)^2]}{(n - p)} \right\}^{1/2} \quad (1-7)$$

In an acceptable structure refinement,  $R_1$  values are typically less than 0.10 and the GoF is close to one. It is helpful to standardize the atomic positions of a crystal structure, using the program STRUCTURE TIDY.<sup>65</sup> A crystallographic information file (CIF) is prepared, which can be checked using standard protocols such as the program PLATON<sup>66</sup> so that the structure is critically evaluated and examined for any problems.

### 1.6.2 Energy Dispersive X-ray (EDX) Analysis

EDX analysis involves a process in which a beam of high-energy electrons strikes a sample to eject core electrons, so that the subsequent relaxation of an electron from a higher energy level to the empty level generates X-ray radiation that is characteristic of the elements constituting the sample (**Figure 1.8**). Qualitative (identification of elements) and quantitative analysis (relative amounts of these elements) in a sample can thus be performed by measuring the energy of the X-ray radiation and their relative intensities. For this purpose, a JEOL JSM-6010 LA scanning electron microscope is used.

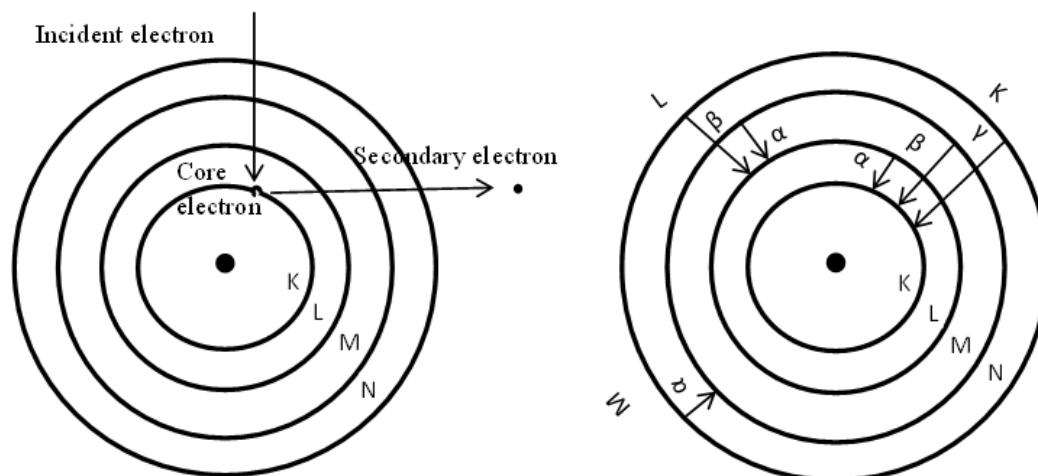


**Figure 1.8** Schematic representation of EDX process.

However, this is a simplified picture of a more complex process. When a high-energy electron beam hits the sample, different types of processes take place, including not only EDX, but also generation of secondary electrons, Auger electrons, backscattered electrons, Bremsstrahlung, and secondary X-rays. Some of these processes convey information about surface morphology (secondary electrons, SEM imaging), distribution of different elements in the sample (backscattered electrons), and chemical composition of the surface (Auger electrons). However, other processes limit the accuracy of EDX, which we typically estimate at 5% for the relative chemical composition of a given element. A *ZAF* correction (where *Z* = atomic number, *A* = absorption, and *F* = fluorescence) is applied. Peak overlap and the occurrence of other peaks (e.g., secondary fluorescence, escape, and sum peaks) also sometimes make elemental identification difficult. Despite these limitations, EDX serves as an important and often the only method to determine chemical composition in solid state compounds.<sup>67</sup>

### 1.7 Band Structure Calculations

The detailed electronic band structure of a crystalline solid is essential to understanding its properties and chemical bonding. Calculation of the band structure is

carried out by solving the time-independent Schrödinger equation with the aid of some approximations. In the simplified case of a one-dimensional solid, the equation becomes (where  $H$  is Hamiltonian operator,  $E$  is energy of state,  $h$  ( $\hbar=h/2\pi$ ) is a Planck's constant,  $m$  is the mass of electron,  $V$  is potential energy of the system,  $\Psi$  is wavefunction):

$$H\Psi = E\Psi \quad (1-8)$$

$$\left(-\frac{\hbar^2}{2m}\frac{d^2}{dx^2} + V(x)\right)\Psi(x) = E\Psi(x) \quad (1-9)$$

One approach to solving this equation is to begin with a free electron model in which a zero-ion-core potential is considered first and then the potential is gradually turned on ("nearly free-electron approximation"). Another approach is to begin with atoms and then allow electron delocalization to take place through orbital overlap ("tight-binding approximation"). In either case, the periodic potential of a crystalline solid leads to restrictions on the form of the wave functions, as dictated by Bloch's theorem and  $k$  appears as a quantized value corresponding to the wavevector (or crystal momentum),  $a$  is a periodic distance:

$$V(x + a) = V(x) \quad (1-10)$$

$$\Psi(x + a) = e^{ika}\Psi(x) \quad (1-11)$$

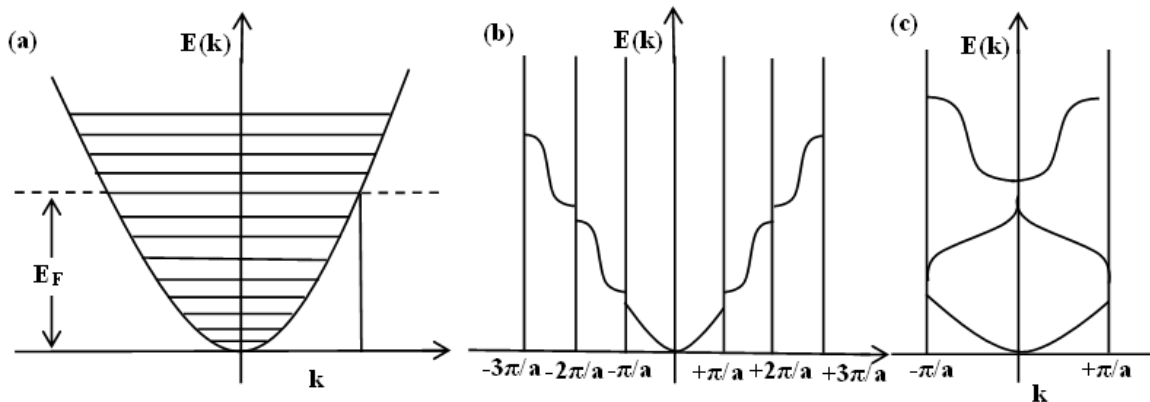


**Figure 1.9** Band structure: (a) free electron system; (b) extended form and (c) reduced form under potential.

Starting from the free-electron model, the introduction of a periodic potential causes energy gaps to be formed, as can be depicted in the extended or reduced forms of the energy dispersion ( $E$  vs.  $k$ ) diagram (**Figure 1.9**).

Starting from the tight-binding model, the wavefunctions ( $\Psi_k$ ) can be expressed as linear combinations of atomic orbitals  $\chi_n$ , which serve as basis functions, adapted to the translational symmetry, called Bloch functions:

$$\Psi_k = \sum_n e^{ikna} \chi_n \quad (1-12)$$

For example, a linear chain of equally spaced H atoms would have Bloch functions consisting of linear combinations of s-orbitals.<sup>68</sup> The wavevector  $k$  is quantized and it is sufficient to specify values of  $k$  within the range  $+\pi/a$  to  $-\pi/a$ , called the first Brillouin zone, because the functions simply repeat beyond this range. The number of  $k$ -points depends on the number of crystal translations, and the value of  $k$  corresponds to the number of nodes in the wavefunction.

The symmetry of the wavefunctions and how the atomic orbitals interact with each other dictate the band dispersion. For example, a band derived from a one-dimensional chain of s-orbitals has its lowest energy at  $k = 0$ , whereas a band derived from a similar chain of  $p_z$ -orbitals has its lowest energy at  $k = \pi/a$  (**Figure 1.10**).

The width of a band (i.e., its energy dispersion) is determined by the extent of overlap; strong overlap interactions lead to wider bands. Electrons occupy these bands up to a highest energy called the Fermi level, which is important in influencing the electronic properties of a material. An alternative way to portray a band structure is to plot the density of states (DOS) as a function of energy. The DOS is defined as the number of states lying within an energy increment  $\delta E$ , around a given energy  $E$ . The

total number of occupied states is then found by integrating the DOS up to the Fermi level.

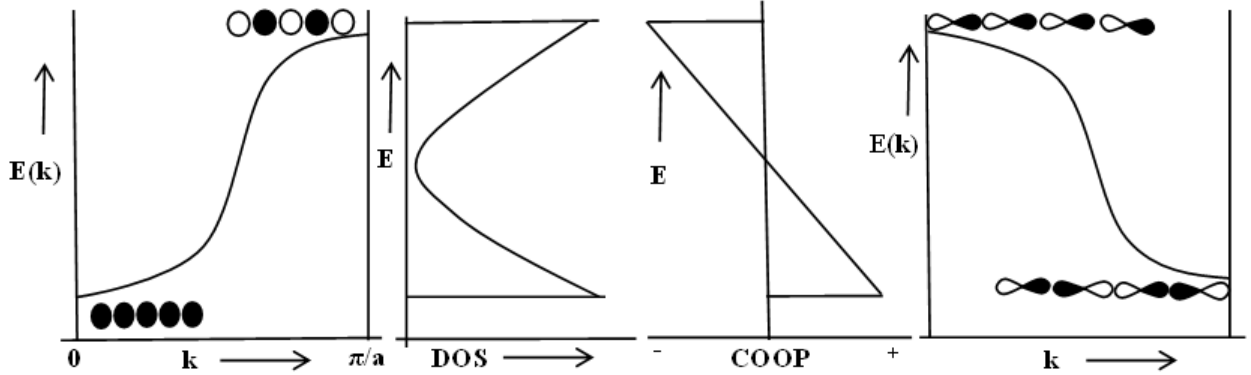


**Figure 1.10** Band structure based on LCAO and Bloch theorem.

In molecular systems, a Mulliken population analysis can be carried out to partition electrons belonging to given atoms and to specified bonds. For example, in  $H_2$  molecule, the distribution of electrons is specified by:

$$1 = \int \Psi^2 d\tau = \int (c\Psi_1 + c_2\Psi_2)^2 d\tau \quad (1-13)$$

$$1 = c_1^2 + c_2^2 + 2c_1c_2 \int \Psi_1\Psi_2 d\tau = c_1^2 + c_2^2 + 2c_1c_2S_{12} \quad (1-14)$$

The number of electrons is split evenly in half between the two H atoms, so that one has  $c_1^2 + c_1c_2S_{12}$  (and the other has  $c_2^2 + c_1c_2S_{12}$ ), where  $c_i$  are the coefficients in the linear combination of atomic orbitals used to express the molecular wavefunctions, and  $S_{12}$  is the overlap integral. The bond strength can be gauged by the quantity  $2c_1c_2S_{12}$ . In crystalline solids, a similar population analysis can be applied to evaluate electron populations and bonding interactions. The contribution of a specified atom (or orbital) is partitioned in the DOS, and integrated up to the Fermi level to give the electron population, called a projection of the DOS. Similarly, bonding interactions are measured

by the crystal orbital overlap population (COOP). These COOP curves can be positive (bonding) or negative (antibonding), and the net interaction is obtained by integrating the COOP curve up to the Fermi level.<sup>69</sup>

In this work, tight-binding linear muffin tin orbital (TB-LMTO) calculations were performed. In this method, a density functional calculation is carried out using the atomic spheres approximation (ASA) and the local density approximation (LDA).<sup>70</sup> The ASA considers spherically symmetric charge density inside the Wigner-Seitz cell around a lattice point and neglects orbital overlap. The potential near the nuclei is truncated so that it resembles a muffin tin, and the empty space between nuclei is filled with spheres with zero potential. The LDA replaces the exchange-correlation energy with that of a homogeneous electron gas. This program evaluates COHP (crystal orbital Hamilton population),<sup>69</sup> a similar quantity as COOP derived from the band energy calculation except that the interpretation of signs is reversed (negative meaning bonding and positive meaning antibonding). For this reason, plots of COHP instead of COOP are normally shown. The band structure calculation in term of DOS, COHP and integrated  $-\text{COHP}$  of  $\text{LaZn}_{0.67}\text{As}_2$  is given in **Figure 1.11**. The plot also shows atomic projection (La, Zn, As) of DOS and band structure calculation was done for both ideal formula  $\text{LaZnAs}_2$  and Zn deficient compound  $\text{LaZn}_{0.67}\text{As}_2$ .<sup>15</sup>

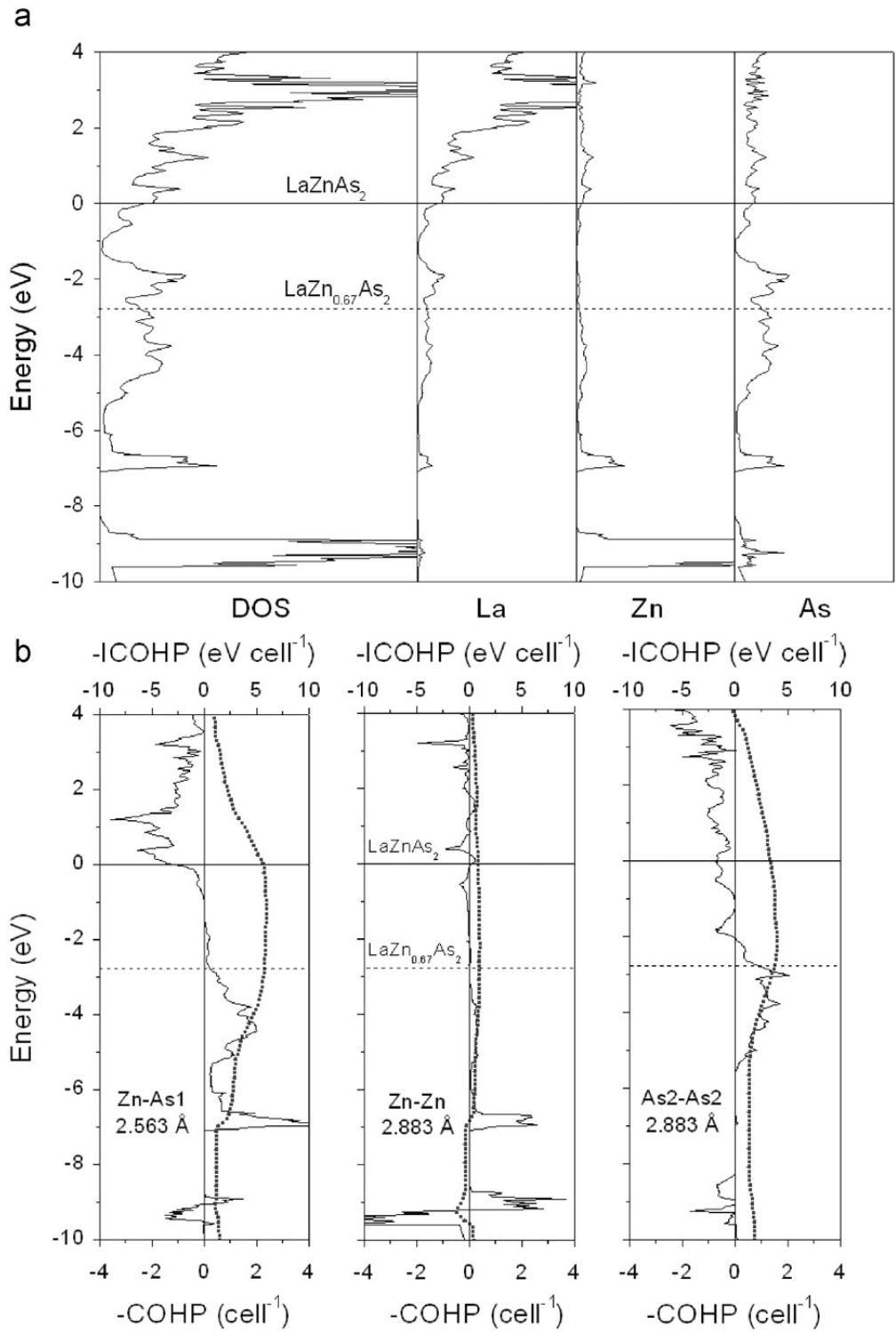


**Figure 1.11** Band structure calculations for  $\text{LaZn}_{0.67}\text{As}_2$ .

## 1.8 Target Physical Properties during Project Design

The compounds synthesized in this thesis may find importance for their electrical, magnetic, and thermoelectric properties. Brief descriptions of these properties, considered during the project design, are given below. Owing to time constraints and sample quality, property measurements were not carried out but would be useful for future work.

### 1.8.1 Superconductivity in Layered Structures

The electronic properties of a crystalline solid depend on the band structure, especially the bands near the Fermi level. In a metal, there is no energy gap at the Fermi level. In a semiconductor, there is a gap between the highest energy filled band (valence band) and the lowest energy unfilled band (conduction band), typically smaller than 3.5 eV. In an insulator, the band gap is greater and electrical conductivity becomes insignificant. The temperature dependence of the electrical conductivity (or its inverse, electrical resistivity) differs for a metal versus a semiconductor. Resistivity is usually the quantity reported in a metal, and it typically decreases as the temperature is lowered, because lattice vibrations which impede electron motion are diminished, until it reaches a residual value due to imperfections in the crystal. Conductivity is normally reported for a semiconductor, and it rises exponentially as the temperature is increased, because the main effect is thermal activation to give a greater concentration of charge carriers.

Early efforts to examine the low-temperature behavior of the electrical resistivity of metals led H. Kamerlingh Onnes to discover a new kind of phenomenon called superconductivity in 1911.<sup>71</sup> Basically, superconductivity is a state of zero resistance exhibited by certain metals and compounds below a critical temperature  $T_C$ . Some metals

and binary intermetallic compounds were known to show superconductivity at very low temperature,<sup>71</sup> but in 1986, the discovery of cuprate superconductors having  $T_c$  greater than the boiling temperature of nitrogen added a new dimension and gave great hopes in the search for new superconductors. Cuprates have layered structures in which  $[\text{CuO}_2]$  layers are found to be responsible for superconductivity. In 2008, a new type of iron-based pnictide superconductors diverted attention of researchers away from cuprates<sup>72</sup> and created an exciting direction for research. They comprise 1111-type (e.g.,  $\text{LaFeAsO}$ ), 122-type (e.g.,  $\text{BaFe}_2\text{As}_2$ ) (**Figure 1.12**) and 111-type (e.g.,  $\text{LiFeAs}$ ) materials, all exhibiting layered structures.<sup>73</sup> These results demand a systematic study of layered *RE*-based ternary and quaternary arsenides. As part of this effort, new layered arsenides have been prepared in this thesis.

### 1.8.2 Dilute Magnetic Semiconductors

Materials that combine magnetic and semiconducting properties have potential applications in spintronics.<sup>8</sup> For practical purposes, the material should exhibit ferromagnetic ordering at room temperature, maintain this ordering while functioning as a semiconductor, and be compatible with existing technology. Suitable candidates having these properties are dilute magnetic semiconductors (DMS). The most common strategy is to dope a semiconductor with a magnetic ion like  $\text{Mn}^{2+}$ . Extensively studied materials are Mn-doped II–V and III–V compounds. As reported by Ohno,  $(\text{Mn}, \text{Ga})\text{As}$  exhibits the highest Curie temperature of 110 K.<sup>12</sup> Research is ongoing to find other suitable DMS candidates. As part of this study, Mn substitution is attempted in  $\text{RE}_{0.67}\text{Zn}_2\text{As}_2$ , a ternary semiconductor, leading to a new series of quaternary arsenides.

### 1.8.3 Thermoelectricity

Thermoelectric materials can be used to generate electrical power from waste heat, or to build fluid-free refrigerators. Their suitability for an application at a temperature  $T$  is gauged by a figure of merit  $ZT = \frac{\alpha^2 \sigma T}{\kappa}$  where  $\alpha$  is the Seebeck coefficient,  $\sigma$  is the electrical conductivity, and  $\kappa$  is the thermal conductivity. To date, many research efforts have led to  $ZT$  values of nearly unity. To improve  $ZT$ , a material should have high Seebeck coefficients, high electrical conductivity, and low thermal conductivity, which is a very challenging requirement. The best candidates are narrow band gap semiconductors. To reduce thermal conductivity, different structures have been investigated. So far,  $\text{Bi}_2\text{Te}_{2.7}\text{Se}_{0.3}$  ( $n$ -type) (**Figure 1.12**) and  $\text{Bi}_{0.5}\text{Sb}_{1.5}\text{Te}_3$  ( $p$ -type) have been found to have the highest  $ZT$  values; their crystal structures consist of layers.<sup>74</sup> The layered nature of the arsenides reported in this thesis suggests that they may be potential candidates as thermoelectric materials. Moreover, most crystal structures reported in this thesis have a  $\text{CaAl}_2\text{Si}_2$ -type structure, or slabs derived from this structure, resulting in strong anisotropy which may help to reduce thermal conductivity.<sup>75</sup>

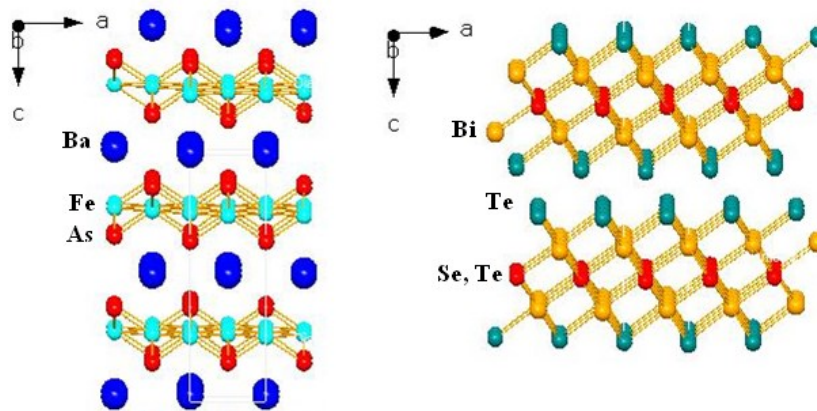


**Figure 1.12** Layered structure of superconductor,  $\text{BaFe}_2\text{As}_2$  and thermoelectric,  $\text{Bi}_2(\text{SeTe})_3$ .

## 1.9 Motivation and Objective

Our research group focuses mainly on synthetic solid state chemistry using high-temperature reactions. The aim of my research is to synthesize and characterize new ternary and quaternary arsenides. Over the last few years, the careful investigation of ternary and quaternary pnictides (other compounds of group 15 elements – P, As, Sb) has provided some intuition to design new layered arsenides which may be useful for applications as superconductors, magnetic semiconductors, and thermoelectric materials. This thesis describes successful attempts to synthesize these arsenides in combination with rare-earth and transition metals, extending the body of binary arsenides previously known to more complex ternary and quaternary arsenides. The bonding in these compounds is more complicated and is examined to help gain insight for designing materials with desired properties. Efforts were made to optimize the syntheses in hopes of obtaining suitable samples (pure phases, large single crystals) for property measurements.

## 1.10 References

1. DiSalvo, J. F. *Science* **1990**, *247*, 649-655.
2. Walsh, A. *Nature Chem.* **2015**, *7*, 274-275.
3. Villars, P.; Cenzual, K. Pearson's Crystal Data - Crystal Structure Database for Inorganic Compounds, Release **2015/16**, ASM international, Materials Park, Ohio, USA.
4. Zdanowicz, W.; Zdanowicz, L. *Annu. Rev. Mater. Sci.* **1975**, *5*, 301-328.
5. Bechstedt, F.; Belabbes, A.; *J. Phys.: Condens. Matter* **2013**, *25*, 273201-273228.
6. Blakemore, J. S. *J. Appl. Phys.* **1982**, *53*, 123-181.
7. Saparov, B.; Mitchell, J. E.; Sefat, A. S. *Supercond. Sci. Technol.* **2012**, *25*, 8-25.
8. Beach, G. *Nature Mat.* **2010**, *9*, 959-960.
9. Erwin, S. C.; Petukhov, A. G. *Phys. Rev. Lett.* **2002**, *89*, 227201-227204.
10. Dietl, T. *Nature Mat.* **2010**, *9*, 965-974.
11. Ohno, H. *Nature Mat.* **2010**, *9*, 952-954.
12. Ohno, H.; Shen, A.; Matsukura, F.; Oiwa, A.; Endo, A.; Katsumoto, S.; Iye, Y. *Appl. Phys. Lett.* **1996**, *69*, 363-365.
13. Cameron, J. M.; Hughes, R. W.; Zhao, Y.; Gregory, D. H. *Chem. Soc. Rev.* **2011**, *40*, 4099-4118.
14. Johrendt, D. *J. Mater. Chem.* **2011**, *21*, 13726-13736.
15. Stoyko, S. S.; Mar, A. *J Solid State Chem.* **2011**, *184*, 2360-2367.
16. Stoyko, S. S.; Mar, A. *Inorg. Chem.* **2011**, *50*, 11152-11161.
17. Lin, X.; Stoyko, S. S.; Mar, A. *J. Solid State Chem.* **2013**, *199*, 189-195.
18. Lin, X.; Mar, A. *Inorg. Chem.* **2013**, *52*, 7261-7270.
19. Geng, F.; Ma, R.; Sasaki, T. *Acc. Chem. Res.* **2010**, *43*, 1177-1185.

20. Zhu, Y.; Murali, S.; Cai, W.; Li, X.; Suk, J. W.; Potts, J. R.; Ruoff, R. S. *Adv. Mater.* **2010**, *22*, 3906–3924.
21. Yakimova, R.; Vasiliauskas, R.; Eriksson, J.; Syväjärvi, M. *Mater. Sci. Forum* **2012**, *711*, 3-10.
22. Pumera, M.; Sofer, Z.; Ambrosi, A. *J. Mater. Chem.* **2014**, *2*, 8981-8987.
23. Baronnet, A. *Prog. Crystal Growth Charact.* **1978**, *178*, 151–211.
24. Pandey, D.; Krishna, P. *Prog. Crystal Growth Charact.* **1983**, *7*, 213-258.
25. Magneli, A. *Acta Crystallogr.* **1953**, *6*, 495-500.
26. Ruddlesden, S. N.; Popper, P. *Acta Crystallogr.* **1957**, *10*, 538-539.
27. Ruddlesden, S. N.; Popper, P. *Acta Crystallogr.* **1958**, *11*, 54-55.
28. Dion, M.; Ganne, M.; Tournoux, M. *Mater. Res. Bull.* **1981**, *16*, 1429-1435.
29. Jacobson, A. J.; Johnson, J. W.; Lewandowski, J. T. *Inorg. Chem.* **1985**, *24*, 3727-3729.
30. Aurivillius, B. *Ark. Kemi* **1949**, *1*, 463-480.
31. Makovicky, E. *Neues. Jahrb. Miner. Abh.* **1989**, *160*, 269-297.
32. Mrotzek, A.; Kanatzidis, M.G. *Acc. Chem. Res.* **2003**, *36*, 111-119.
33. Poudeu, P. F. P.; Kanatzidis, M. G. *Chem. Commun.* **2005**, *21*, 2672-2674.
34. West, A. R. *Solid State Chemistry and its applications*, John Wiley & Sons Ltd: Chichester, **1984**.
35. Lewis, G. N. *J. Am. Chem. Soc.* **1916**, *38*, 762-785.
36. Wallace, W. E. *Annu. Rev. Phys. Chem.* **1964**, *15*, 109-130.
37. Nesper, R. *Angew. Chem. Int. Ed. Engl.* **1991**, *30*, 789-817.
38. Nesper, R. *Z. Anorg. Allg. Chem.* **2014**, *640*, 2639-2648.

39. Corbett, J. D. *Chem. Rev.* **1985**, *85*, 383-397.
40. Müller, U. *Inorganic Structural Chemistry*, 2nd ed.; Wiley: Chichester, 2007.
41. Kossel, W. *Ann. Phys.* **1916**, *49*, 229.
42. Brylak, M.; Möller, M. H.; Jeitschko, W. *J. Solid State Chem.* **1995**, *115*, 305-308.
43. Eschen, M.; Jeitschko, W. *Z. Naturforsch. B.* **2003**, *58*, 399-409.
44. Nientiedt, A. T.; Lincke, H.; Rodewald, U. C.; Pöttgen, R.; Jeitschko, W. *Z. Naturforsch.* **2011**, *66b*, 221-226.
45. Hoffmann, R.; Zheng, C. *J. Phys. Chem.* **1985**, *89*, 4175-4181.
46. Zheng, C.; Hoffmann, R.; Nesper, R.; von Schnering, H.-G. *J. Am. Chem. Soc.* **1986**, *108*, 1876-1884.
47. Zheng, C.; Hoffmann, R. *J. Solid State Chem.* **1988**, *72*, 58-71.
48. Johrendt, D.; Felser, C.; Jepsen, O.; Andersen, O. K.; Mewis, A.; Rouxel, J. *J. Solid State Chem.* **1997**, *130*, 254-265.
49. Stoyko, S. S.; Ramachandran, K. K.; Blanchard, P. E. R.; Rosmus, K. A.; Aitken, J. A.; Mar, A. *J. Solid State Chem.* **2014**, *213*, 275-286.
50. Raffius, H.; Mörsen, E.; Mosel, B. D.; Müller-Warmuth, W.; Jeitschko, W.; Terbüchte, L.; Vomhof, T. *J. Phys. Chem. Solids* **1993**, *54*, 135-144.
51. Jeitschko, W.; Terbüchte, L. J.; Rodewald, U. *Ch. Z. Naturforsch.* **2001**, *56*, 1281-1288.
52. Babizhetskyy, V.; Sénéchal, C. Le.; Bauer, J.; Députier, S.; Guérin, R. *J. Alloys Comp.* **1999**, *287*, 174-180.
53. Stoyko S. S.; Oryshchyn S.V. *Visn. Lviv. Derzh. Univ., Ser. Khim.* **2010**, *51*, 74-78.
54. Jeitschko, W.; Jaberg, B. *J. Less-Common Met.* **1981**, *79*, 311-314.

55. Babizhetskyy, V.; Guérin, R.; Simon, A. *Z. Naturforsch., B: J.Chem. Sci.* **2006**, *61*, 733-740.
56. Zelinska, M.; Zhak, O.; Oryshchyn, S.; Polianska, T.; Pivan, J.-Y. *Z. Naturforsch., B: J. Chem. Sci.* **2007**, *62*, 1143-1152.
57. Pivan, J. Y.; Guérin, R.; Sergent, M. *J. Less-Common Met.* **1985**, *107*, 249-258.
58. Wurth, A.; Keimes, V.; Johrendt, D.; Mewis, A. *Z. Anorg. Allg. Chem.* **2001**, *627*, 2183-2190.
59. Dhahri, E. *J. Phys.: Condens. Matter* **1996**, *8*, 4351-4360.
60. Stoyko, S. S.; Ramachandran, K. K.; Mullen, C. S.; Mar, A. *Inorg. Chem.* **2013**, *52*, 1040-1046.
61. Kraus, W.; Nolze, G. *J. Appl. Cryst.* **1996**, *29*, 301-303.
62. Holland, T. J. B.; Redfern, S. A. T. *Mineral. Mag.* **1997**, *61*, 65-77.
63. Massa, W. Ed.; *Crystal Structure Determination, 2nd Ed*; Springer-Verlag: Berlin, **2004**.
64. Sheldrick, G. M. SHELXTL. *Bruker AXS Inc.: Madison, WI* **2001**, *6.12*.
65. Gelato, L. M.; Parthé, E. *J. Appl. Crystallogr.* **1987**, *20*, 139-143.
66. Spek, A. L. *Acta Cryst.* **2009**, *D65*, 148-155.
67. Russ, J. C. *Fundamentals of energy dispersive X-ray analysis*, Butterworth: London, **1984**.
68. Hoffmann, R. *Angew. Chem. Int. Ed. Engl.* **1987**, *26*, 846-878.
69. Alemany P.; Canadell, E. Chemical Bonding in Solids, In *The Chemical Bond : Chemical Bonding Across the Periodic Table*, ch15; Frenking, G.; Shaik, S.; Wiley-VCH Verlag GmbH & Co. KGaA: Weinheim, Germany. **2014**.
70. Anderson, O. K. LDA, ASA. *Phys. Rev. B: Condens. Matter* **1975**, *12*, 3060-3083.

71. Hott, R.; Kleiner, R.; Wolf, T.; Zwicknagi, G. *Review on Superconducting Materials*, arXiv:1306.0429[cond-mat.supr-con].
72. Rahman, M. A.; Rahaman, M. Z.; Samsuddoha, M. N. *Am. J. Phys. Appl.* **2015**, *3*, 39-56.
73. Johrendt, D.; Hosono, H.; Hoffmann, R.-D.; Pöttgen, R. *Z. Kristallogr.* **2011**, *226*, 435–446.
74. Tritt, T. M.; Subramanian, M. A. *MRS Bulletin* **2006**, *31*, 188-194.
75. Gascoin, F.; Ottensmann, S.; Stark, D.; Haile, S. M.; Snyder, G. J. *Adv. Funct. Mater.* **2005**, *15*, 1860–1864.

## Chapter 2

### **Manganese-Substituted Rare-Earth Zinc Arsenides $RE_{1-y}Mn_xZn_{2-x}As_2$ ( $RE = Eu-Lu$ ) and $RE_{2-y}Mn_xZn_{4-x}As_4$ ( $RE = La-Nd, Sm, Gd$ )**

*A version of this chapter has been published. Lin, X.; Tabassum, D.; Rudyk, B. W.; Mar, A. Inorg. Chem. 2014, 53, 8431-8441.*

#### **2.1 Introduction**

Many ternary pnictides of the form  $AB_2X_2$  adopt either the tetragonal  $ThCr_2Si_2$ -type ( $I4/mmm$ ) or the trigonal  $CaAl_2Si_2$ -type ( $P\bar{3}m1$ ) structure. The  $ThCr_2Si_2$ -type phases form for a wide variety of  $B$  components<sup>1-3</sup> and have long been renowned for their diverse physical properties, such as superconductivity in  $BaFe_2As_2$ -based materials.<sup>4-7</sup> The  $CaAl_2Si_2$ -type phases form for a more restricted set of  $B$  components<sup>2,8-14</sup> and have been identified as possible candidates for thermoelectric materials.<sup>15-21</sup> In both cases, doping is an important strategy for optimizing and improving properties; for example, superconductivity is induced in  $BaFe_2As_2$  through hole doping (in  $K_xBa_{1-x}Fe_2As_2$ )<sup>4</sup> and thermoelectric transport properties can be tuned in  $YbZn_2Sb_2$  through isovalent doping (in  $Ca_xYb_{1-x}Zn_2Sb_2$ ).<sup>22</sup> Because subtle structural changes can often take place in the course of these chemical modifications, “substitution” is perhaps a more appropriate term than “doping”.

It is desirable to extend the versatility of  $AB_2X_2$  phases with the  $CaAl_2Si_2$ -type structure among ternary pnictides and to identify other potential applications of this class of compounds. All  $CaAl_2Si_2$ -type phases known so far appear to conform quite strictly to the requirement of  $d^0$ ,  $d^5$ , or  $d^{10}$  configurations for the  $B$  component.<sup>2,8-10</sup> There is also a

weaker condition of an ideal valence electron count of  $16 e^-/\text{f.u.}$ , corresponding to a charge-balanced formulation and, in principle, the presence of a small band gap between filled valence and empty conduction bands, leading to the semiconducting behaviour required in thermoelectric materials. This electron count is occasionally violated, as in  $REAl_2Si_2$  and  $REAl_2Ge_2$  ( $17 e^-/\text{f.u.}$ ), because the expected band gap has vanished and semimetallic behaviour develops instead.<sup>11,12</sup> Ternary pnictides satisfying both conditions are well known for  $AM_2Pn_2$  ( $A$  = alkaline-earth or divalent rare-earth metal;  $M$  = Mg, Mn, Zn, Cd;  $Pn$  = P, As, Sb, Bi).<sup>23</sup> These can be extended to phases containing rare-earth metals as the  $A$  component, while maintaining the electron count, through formation of defects in ternary arsenides  $RE_{0.67}Zn_2As_2$ <sup>24</sup> or through aliovalent substitution with two different metals as the  $B$  component in quaternary pnictides  $REMM'Pn_2$  ( $M$  = Ag, Cu;  $M'$  = Mn, Zn;  $Pn$  = P, As, Sb).<sup>25-33</sup> Through these investigations, there is now greater understanding of the influence of the chemical substituents on the size of the band gap. For example, judicious combinations of  $M$  and  $M'$  components (such as Cu–Zn) may narrow the band gap so that the valence and conduction bands just touch.<sup>33</sup> In this way, solid solutions  $GdCu_xZn_{2-x}P_2$  ( $1.0 \leq x \leq 1.3$ ) are formed in which the electron count can deviate away from  $16 e^-/\text{f.u.}$ <sup>31</sup> Similar types of limited solid solutions have been found in the related silicides  $GdMn_xAl_{2-x}Si_2$  ( $0 \leq x \leq 0.25$ ) and germanides  $GdZn_xAl_{2-x}Ge_2$  ( $0 \leq x \leq 1.0$ ).<sup>11,12</sup> Efforts are now underway to evaluate thermoelectric properties tuned through appropriate substitution in solid solutions of various phosphides  $(Ca/Yb)(Mn/Cu/Zn)_2P_2$ <sup>34,35</sup> and antimonides  $(Ca/Eu/Yb)(Mn/Zn/Cd)_2Sb_2$ .<sup>22,36-41</sup> The presence of two-dimensional slabs in  $CaAl_2Si_2$ -type phases conforms with the realization that simple layered structures with anisotropic

bonding may be favourable for exhibiting the low thermal conductivity required for good thermoelectric performance.<sup>42</sup> Substitution with Mn may impart interesting magnetic properties, although these have not yet been investigated in detail. It is worth noting, however, that  $\text{Li}_{1+y}\text{Mn}_x\text{Zn}_{1-x}\text{Pn}$  ( $\text{Pn} = \text{P}, \text{As}$ ) have recently been touted as “new-generation” dilute ferromagnetic semiconductors;<sup>43,44</sup> they adopt a filled zincblende-type structure, from which the  $\text{CaAl}_2\text{Si}_2$ -type structure can be derived.

We have been systematically investigating the ternary rare-earth zinc arsenide systems  $\text{RE-Zn-As}$ , which contain not only  $\text{CaAl}_2\text{Si}_2$ -type phases ( $\text{REZn}_2\text{As}_2$  ( $\text{RE} = \text{Eu}, \text{Yb}$ ),  $\text{RE}_{0.67}\text{Zn}_2\text{As}_2$  ( $\text{RE} = \text{La-Nd}, \text{Sm}$ ))<sup>24,27,28,45-48</sup> but also many other phases with diverse structures ( $\text{REZn}_2\text{As}_3$  ( $\text{RE} = \text{La-Pr}$ );  $\text{REZn}_{0.67}\text{As}_2$ ,  $\text{REZn}_3\text{As}_3$ ,  $\text{REZn}_{2-x}\text{As}_2 \cdot n(\text{REAs})$  ( $n = 3, 4, 5, 6$ ) for  $\text{RE} = \text{La-Nd}, \text{Sm}$ ;  $\text{Eu}_2\text{Zn}_2\text{As}_3$ ,  $\text{Eu}_{11}\text{Zn}_6\text{As}_{12}$ ).<sup>49-54</sup> Manganese substitution appears to be viable in these systems, as suggested by the formation of the two compounds  $\text{Ce}_4(\text{Mn},\text{Zn})_{2-x}\text{As}_5$  and  $\text{Ce}_6(\text{Mn},\text{Zn})_{2-x}\text{As}_7$  within the homologous series  $\text{REZn}_{2-x}\text{As}_2 \cdot n(\text{REAs})$ , which is derived from the intergrowth of  $\text{CaAl}_2\text{Si}_2$ -type slabs with rocksalt-type slabs [ $\text{REAs}$ ] of variable thickness.<sup>52</sup> Herein we report the preparation of quaternary arsenides in which the partial substitution of Mn for Zn leads to two distinct series forming for the earlier ( $\text{RE}_{2-y}\text{Mn}_x\text{Zn}_{4-x}\text{As}_4$ ;  $\text{RE} = \text{La-Nd}, \text{Sm}, \text{Gd}$ ) versus later rare-earth members ( $\text{RE}_{1-y}\text{Mn}_x\text{Zn}_{2-x}\text{As}_2$ ;  $\text{RE} = \text{Eu-Lu}$ ). The  $\text{RE}_{1-y}\text{Mn}_x\text{Zn}_{2-x}\text{As}_2$  series is closely related to the parent  $\text{RE}$ -defective arsenides  $\text{RE}_{0.67}\text{Zn}_2\text{As}_2$ , but the  $\text{RE}_{2-y}\text{Mn}_x\text{Zn}_{4-x}\text{As}_4$  series has a doubled trigonal  $c$ -parameter. The structural effects of Mn substitution are more complicated than anticipated, and are explored within the series  $\text{Gd}_{0.67}\text{Mn}_x\text{Zn}_{2-x}\text{As}_2$ . Band structure calculations were carried out to examine how the

band gap is influenced by this Mn substitution. X-ray photoelectron spectra (XPS) were collected to probe the valence state of the Mn atoms in these compounds.

## 2.2 Experimental Section

### 2.2.1 Synthesis

Starting materials were freshly filed *RE* pieces (99.9%, Hefa), Mn powder (99.99%, Aldrich), Zn shot (99.99%, Aldrich), and As lumps (99.999%, Alfa-Aesar). These elements were initially combined on a 0.3-g scale with the loading composition “ $RE_{0.67}MnZnAs_2$ ” to target the preparation of defective  $CaAl_2Si_2$ -type phases for various *RE* components. Subsequent energy-dispersive X-ray (EDX) analysis suggested slightly different compositions than loaded for some crystals resulting from the syntheses, corresponding to approximately 10% *RE*, 10% Mn, 40% Zn, and 40% As. Ultimately, the *RE*/Mn/Zn/As ratios used in obtaining the title compounds were 0.67:1:1:2 for the  $RE_{1-y}Mn_xZn_{2-x}As_2$  (*RE* = Eu–Lu) series and 1:1:4:4 for the  $RE_{2-y}Mn_xZn_{4-x}As_4$  (*RE* = La–Nd, Sm, Gd) series. The mixtures were loaded into fused-silica tubes, which were evacuated and sealed. The tubes were heated at 500 °C for 2 d, heated to 750 °C over 20 h, held at this temperature for 7 d, and then cooled to room temperature over 10 h. The preheating step at 500 °C was included to minimize loss of the volatile components (Zn and As). Powder X-ray diffraction (XRD) patterns were collected on an Inel powder diffractometer equipped with a curved position-sensitive detector (CPS 120) and a Cu  $K\alpha_1$  radiation source operated at 40 kV and 20 mA. The products consisted of the title compounds as the major phases, with binary arsenides and small amounts of other ternary arsenides as minor phases, as shown in representative powder XRD patterns (**Figures A 1.1 and A 1.2**). Phase relationships in arsenide systems remain poorly understood and

further work is in progress to elucidate them. To promote the growth of crystals suitable for structure determination, the as-prepared samples were reheated at 800 °C for 2 d, heated to 1050 °C over 20 h, held at this temperature for 7 d, slowly cooled to 500 °C at a rate of 3 °C/h, and then cooled to room temperature over 2 d. Crystals tended to grow as thinner plates in the  $RE_{2-y}Mn_xZn_{4-x}As_4$  ( $RE = La-Nd, Sm, Gd$ ) series than in the  $RE_{1-y}Mn_xZn_{2-x}As_2$  ( $RE = Eu-Lu$ ) series. Crystals obtained from these reactions were examined by EDX analysis on a JEOL JSM-6010LA scanning electron microscope. Mn is distributed uniformly within these crystals, as seen in elemental maps for a representative sample (**Figure A 1.3**). These analyses generally agree with the expected chemical compositions based on the formulas deduced from the single-crystal structure determinations below (**Table A 1.1**). However, the observed Mn content in some of the  $RE_{1-y}Mn_xZn_{2-x}As_2$  members was somewhat larger than the expected value of 9 atom % based on the average formula  $RE_{0.5}Mn_{0.4}Zn_{1.6}As_2$ . This discrepancy can be attributed to systematic errors in the EDX analysis caused by partial peak overlap of Mn  $K$  and  $RE L$  lines for some of these compounds; it may also reflect an actual variation in composition depending on the  $RE$  member or inaccuracies in occupancy refinements in the structure determinations.

### 2.2.2 Structure Determination

Intensity data were collected at room temperature on a Bruker PLATFORM diffractometer equipped with a SMART APEX II CCD area detector and a graphite-monochromated Mo  $K\alpha$  radiation source, using  $\omega$  scans in 5–8 batches at different  $\phi$  angles with a frame width of 0.3° and an exposure time of 12–20 s per frame. Face-

indexed absorption corrections were applied. Structure solution and refinement were carried out with use of the SHELXTL (version 6.12) program package.<sup>55</sup>

For the series  $RE_{1-y}Mn_xZn_{2-x}As_2$  ( $RE = Eu-Lu$ ), the unit cell parameters ( $a = \sim 4$  Å,  $c = \sim 7$  Å) and the intensity symmetry were consistent with the centrosymmetric trigonal space group  $P\bar{3}m1$  adopted by the expected  $CaAl_2Si_2$ -type structure.<sup>56</sup> For the divalent  $RE$  members of this series ( $RE = Eu, Yb$ ), direct methods revealed the locations of the three sites within this structure:  $1a$  (0, 0, 0) occupied by  $RE$  atoms,  $2d$  (1/3, 2/3,  $\sim 0.63$ ) occupied by a statistical mixture of Mn and Zn atoms, and  $2d$  (1/3, 2/3,  $\sim 0.26$ ) occupied by As atoms. When the occupancies of the transition-metal site were allowed to vary, with the constraint that they sum to unity, they converged to 0.22(2) Mn / 0.78(2) Zn in the Eu member and 0.16(3) Mn / 0.84(3) Zn in the Yb member. The  $RE$  and As sites were found to be fully occupied, although a slight Yb substoichiometry of 0.95(1) was found in the Yb member. The resulting formulas,  $EuMn_{0.4}Zn_{1.6}As_2$  and  $YbMn_{0.3}Zn_{1.7}As_2$ , are electron-precise or very nearly so, with the assumption that Mn and Zn atoms are divalent. For the trivalent  $RE$  members of this series ( $RE = Gd-Tm, Lu$ ), refinement of similar models based on the  $CaAl_2Si_2$ -type structure led to elevated displacement parameters for the  $RE$  sites ( $U_{eq} = \sim 0.03$  Å<sup>2</sup>), implying that they are partially occupied. When freed, the occupancies of the  $RE$  sites converged to 0.51–0.53 for most members ( $RE = Gd-Er$ ) but to slightly lower values of 0.42–0.43 for two later ones ( $RE = Tm, Lu$ ). Inspection of the difference Fourier maps revealed residual electron density at  $2d$  (1/3, 2/3,  $\sim 0.82$ ), typically  $\sim 10$  e<sup>-</sup>/Å<sup>3</sup>, that is close to the original transition-metal site at  $2d$  (1/3, 2/3,  $\sim 0.63$ ). Because these two sites are within  $\sim 1.3$  Å from each other, they were each allowed to contain a disordered mixture of Mn and Zn atoms, with

the constraint that the total occupancy over both sites sum to unity. In general, these refinements led to occupancy ranges of 0.0(1) to 0.1(1) Mn and 0.7(1) to 0.8(1) Zn in the site at  $1/3, 2/3, \sim 0.63$ , in contrast to ranges of 0.0(1) to 0.3(1) Mn and  $-0.1(1)$  to 0.1(1) Zn in the site at  $1/3, 2/3, \sim 0.82$ . That is, there is a primary site that is clearly preferred by Zn atoms, and a secondary site that shows a slight preference for Mn atoms. To treat subsequent refinements on a consistent basis, we applied a simplified structural model containing only Zn atoms in the primary site and Mn atoms in the secondary site, constrained such that their occupancies sum to unity, while the *RE* site was allowed to be partially occupied. The resulting formulas, generally  $RE_{0.5}Mn_{0.4}Zn_{1.6}As_2$  for most members, suggest slightly more pronounced *RE* deficiencies relative to the electron-precise ones assumed for the related ternary arsenides  $RE_{0.67}Zn_2As_2$ . As a test of the consistency of this refinement procedure, two datasets for separate crystals of the Gd-containing member obtained from the same reaction batch were collected. The resulting formulas from the structure refinements on these crystals were  $Gd_{0.52(1)}Mn_{0.40(1)}Zn_{1.60(1)}As_2$  and  $Gd_{0.51(1)}Mn_{0.43(2)}Zn_{1.57(2)}As_2$ , in good agreement with each other.

For the series  $RE_{2-y}Mn_xZn_{4-x}As_4$  ( $RE = La-Nd, Sm, Gd$ ), the intensity symmetry also suggested the trigonal space group  $P\bar{3}m1$  but there is a doubling in the unit cell *c*-parameter to  $\sim 14$  Å. This doubling can be clearly seen in a comparison of the *0kl* nets for crystals of  $Gd_{1-y}Mn_xZn_{2-x}As_2$  versus  $Gd_{2-y}Mn_xZn_{4-x}As_4$ , which was found to occur in both possible forms (**Figure 2.1**).

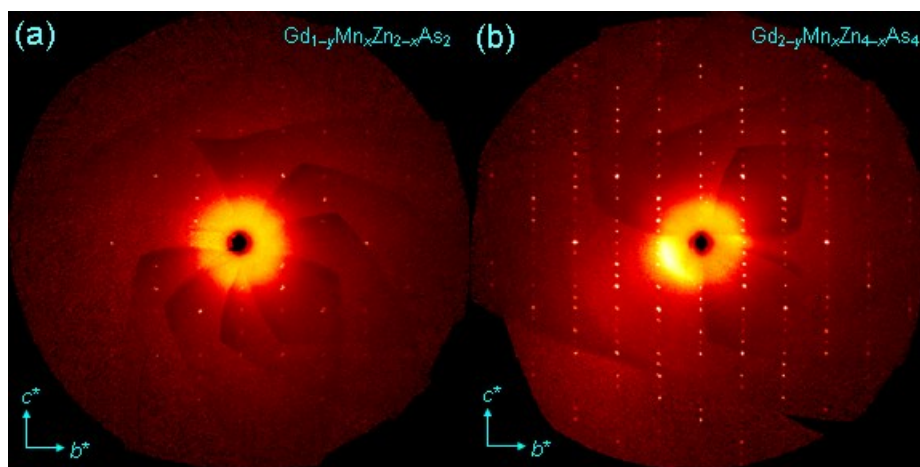


**Figure 2.1** The  $0kl$  nets for crystals of (a)  $\text{Gd}_{1-y}\text{Mn}_x\text{Zn}_{2-x}\text{As}_2$  and (b)  $\text{Gd}_{2-y}\text{Mn}_x\text{Zn}_{4-x}\text{As}_4$ .

Direct methods provided a model corresponding to a superstructure of the  $\text{CaAl}_2\text{Si}_2$ -type (with two  $RE$ , two transition-metal, and two As sites). Refinement of this model indicated full occupancy for the  $RE$  site at  $1a$  (0, 0, 0) but partial occupancy of  $\sim 0.2$ – $0.3$  for the  $RE$  site at  $1b$  (0, 0,  $\frac{1}{2}$ ). Inspection of difference Fourier maps revealed residual electron density corresponding to a third transition-metal site close (within  $\sim 1.2$  Å) to an existing one. Each of these sites was allowed to be occupied by a mixture of Mn and Zn atoms, with the constraint that the occupancies of the two closely spaced ones (at  $1/3, 2/3, \sim 0.33$  and  $1/3, 2/3, \sim 0.41$ ) sum to unity. These refinements led to occupancies of 0.0(2) Mn / 0.6(2) Zn (at  $1/3, 2/3, \sim 0.33$ ), 0.2(2) Mn / 0.2(2) Zn (at  $1/3, 2/3, \sim 0.41$ ), and 0.1(1) Mn / 0.9(1) Zn (at  $1/3, 2/3, \sim 0.80$ ). Again, to simplify the structural analysis, we applied an ordered model in which Mn atoms exclusively occupy the site at  $1/3, 2/3, \sim 0.41$  and Zn atoms occupy the other two sites. For most members, subsequent refinements gave resulting formulas of  $RE_{1.3}\text{Mn}_{0.9}\text{Zn}_{3.1}\text{As}_4$ , essentially in agreement with expectations according to charge balance. For a couple of the structures, such as the Nd-containing member, this simplification leads to slightly worse agreement factors and

slightly higher residual electron density in the difference map; however, for ease of comparison, we prefer to retain this ordered structural model for all members.

Atomic positions were standardized with the program STRUCTURE TIDY.<sup>57</sup> The compounds  $RE_{1-y}Mn_xZn_{2-x}As_2$  ( $RE = \text{Gd-Tm, Lu}$ ) contain an extra transition-metal site relative to the  $\text{CaAl}_2\text{Si}_2$ -type structure; because this standardization changes the choice of equivalent positions, we have opted to retain coordinates to match with the parent structure in these cases. Abbreviated crystallographic data are summarized in **Table 2.1** and **Table 2.2**, positional and displacement parameters are listed in **Table 2.3** and **Table 2.4**, and selected interatomic distances are listed in **Table 2.5** and **Table 2.6**. Full crystallographic details are listed in **Tables A 1.2** and **A 1.3** in **Appendix**. Further data, in the form of crystallographic information files (CIFs), are available as Supporting Information.

**Table 2.1** Crystallographic Data for  $RE_{1-y}Mn_xZn_{2-x}As_2$  ( $RE = Eu-Lu$ ).<sup>a</sup>

Formula	<b>EuMn<sub>0.44(6)</sub>Zn<sub>1.56(6)</sub>As<sub>2</sub></b>	<b>Gd<sub>0.52(1)</sub>Mn<sub>0.40(1)</sub>Zn<sub>1.60(1)</sub>As<sub>2</sub></b>	<b>Tb<sub>0.52(1)</sub>Mn<sub>0.42(1)</sub>Zn<sub>1.58(1)</sub>As<sub>2</sub></b>
fw (amu)	427.95	355.03	355.03
$a$ (Å)	4.234(2)	4.109(3)	4.1135(4)
$c$ (Å)	7.198(4)	6.703(5)	6.7246(7)
$V$ (Å <sup>3</sup> )	111.74(14)	98.02(13)	98.54(2)
$\rho_c$ (gcm <sup>-3</sup> )	6.360	6.014	5.997
$\mu$ (mm <sup>-1</sup> )	37.86	35.88	36.25
$R(F)$ <sup>b</sup>	0.026	0.034	0.025
$R_w(F_o^2)$ <sup>c</sup>	0.043	0.060	0.050
Formula	<b>Dy<sub>0.53(1)</sub>Mn<sub>0.42(1)</sub>Zn<sub>1.58(1)</sub>As<sub>2</sub></b>	<b>Ho<sub>0.53(1)</sub>Mn<sub>0.39(1)</sub>Zn<sub>1.61(1)</sub>As<sub>2</sub></b>	<b>Er<sub>0.51(1)</sub>Mn<sub>0.38(1)</sub>Zn<sub>1.62(1)</sub>As<sub>2</sub></b>
fw (amu)	362.32	363.93	360.04
$a$ (Å)	4.1023(9)	4.091(3)	4.103(5)
$c$ (Å)	6.7197(16)	6.700(11)	6.722(7)
$V$ (Å <sup>3</sup> )	97.93(4)	97.1(2)	98.02(19)
$\rho_c$ (gcm <sup>-3</sup> )	6.143	6.223	6.099
$\mu$ (mm <sup>-1</sup> )	37.49	38.50	38.13
$R(F)$ <sup>b</sup>	0.031	0.032	0.031
$R_w(F_o^2)$ <sup>c</sup>	0.062	0.072	0.045
Formula	<b>Tm<sub>0.43(1)</sub>Mn<sub>0.21(1)</sub>Zn<sub>1.79(1)</sub>As<sub>2</sub></b>	<b>Yb<sub>0.95(1)</sub>Mn<sub>0.32(6)</sub>Zn<sub>1.68(6)</sub>As<sub>2</sub></b>	<b>Lu<sub>0.42(1)</sub>Mn<sub>0.20(1)</sub>Zn<sub>1.80(1)</sub>As<sub>2</sub></b>
fw (amu)	351.03	441.84	348.48
$a$ (Å)	4.0980(18)	4.1682(6)	4.0932(9)
$c$ (Å)	6.664(3)	6.9478(10)	6.6433(14)
$V$ (Å <sup>3</sup> )	96.91(7)	104.54(3)	96.39(4)
$\rho_c$ (gcm <sup>-3</sup> )	6.015	7.018	6.003
$\mu$ (mm <sup>-1</sup> )	38.16	47.12	38.75
$R(F)$ <sup>b</sup>	0.021	0.018	0.021
$R_w(F_o^2)$ <sup>c</sup>	0.021	0.040	0.050

<sup>a</sup>For all structures,  $Z = 1$ ,  $T = 296(2)$  K,  $\lambda = 0.71073$  Å, space group  $P\bar{3}m1$  (No. 164).

<sup>b</sup> $R(F) = \sum ||F_o| - |F_c|| / \sum |F_o|$  for  $F_o^2 > 2\sigma(F_o^2)$ .

<sup>c</sup> $R_w(F_o^2) = [\sum [w(F_o^2 - F_c^2)^2] / \sum wF_o^4]^{1/2}$ ;  $w^{-1} = [\sigma^2(F_o^2) + (Ap)^2 + Bp]$ , where  $p = [\max(F_o^2, 0) + 2F_c^2] / 3$ .

**Table 2.2** Crystallographic Data for  $RE_{2-y}Mn_xZn_{4-x}As_4$  ( $RE = La-Nd, Sm, Gd$ ).<sup>a</sup>

Formula	La <sub>1.25(1)</sub> Mn <sub>0.93(2)</sub> Zn <sub>3.07(2)</sub> As <sub>4</sub>	Ce <sub>1.30(1)</sub> Mn <sub>0.83(3)</sub> Zn <sub>3.17(3)</sub> As <sub>4</sub>	Pr <sub>1.25(1)</sub> Mn <sub>0.95(2)</sub> Zn <sub>3.05(2)</sub> As <sub>4</sub>
Formula	722.33	734.66	727.39
mass (amu)			
$a$ (Å)	4.159(2)	4.156(5)	4.1533(4)
$c$ (Å)	13.639(7)	13.569(16)	13.5629(13)
$V$ (Å <sup>3</sup> )	204.3(2)	204.3(2)	202.61(4)
$\rho_c$ (gcm <sup>-3</sup> )	5.870	6.010	5.961
$\mu$ (mm <sup>-1</sup> )	32.53	33.69	33.81
$R(F)$ <sup>b</sup>	0.052	0.044	0.044
$R_w(F_o^2)$ <sup>c</sup>	0.113	0.125	0.097
Formula	Nd <sub>1.25(1)</sub> Mn <sub>0.95(3)</sub> Zn <sub>3.05(3)</sub> As <sub>4</sub>	Sm <sub>1.24(1)</sub> Mn <sub>0.87(4)</sub> Zn <sub>3.13(4)</sub> As <sub>4</sub>	Gd <sub>1.24(1)</sub> Mn <sub>0.93(3)</sub> Zn <sub>3.07(3)</sub> As <sub>4</sub>
Formula	731.55	738.52	746.45
mass (amu)			
$a$ (Å)	4.1283(17)	4.1240(19)	4.1180(14)
$c$ (Å)	13.513(6)	13.507(6)	13.500(5)
$V$ (Å <sup>3</sup> )	199.45(14)	198.9(2)	198.27(15)
$\rho_c$ (gcm <sup>-3</sup> )	6.091	6.164	6.252
$\mu$ (mm <sup>-1</sup> )	34.84	36.04	37.27
$R(F)$ <sup>b</sup>	0.067	0.051	0.048
$R_w(F_o^2)$ <sup>c</sup>	0.144	0.153	0.135

<sup>a</sup> For all structures,  $Z = 1$ ,  $T = 296(2)$  K,  $\lambda = 0.71073$  Å, space group  $P\bar{3}m1$  (No. 164).

<sup>b</sup>  $R(F) = \sum||F_o| - |F_c|| / \sum|F_o|$  for  $F_o^2 > 2\sigma(F_o^2)$ .

<sup>c</sup>  $R_w(F_o^2) = [\sum[w(F_o^2 - F_c^2)^2] / \sum w F_o^4]^{1/2}$ ;  $w^{-1} = [\sigma^2(F_o^2) + (Ap)^2 + Bp]$ , where  $p = [\max(F_o^2, 0) + 2F_c^2] / 3$ .

**Table 2.3** Atomic Coordinates and Equivalent Isotropic Displacement Parameters ( $\text{\AA}^2$ )<sup>a</sup>  
for  $RE_{1-y}Mn_xZn_{2-x}As_2$  ( $RE = \text{Eu-Lu}$ ).

	<b>EuMn<sub>0.44(6)</sub>Zn<sub>1.56(6)</sub>As<sub>2</sub></b>	<b>Gd<sub>0.52(1)</sub>Mn<sub>0.40(1)</sub>Zn<sub>1.60(1)</sub>As<sub>2</sub></b>	<b>Tb<sub>0.52(1)</sub>Mn<sub>0.42(1)</sub>Zn<sub>1.58(1)</sub>As<sub>2</sub></b>
<i>RE</i> in 1 <i>a</i> (0, 0, 0)			
occupancy	1	0.517(4)	0.516(4)
$U_{\text{eq}}$	0.0123(3)	0.0164(5)	0.0167(3)
Mn in 2 <i>d</i> (1/3, 2/3, <i>z</i> )			
occupancy	0.22(3)	0.195(6)	0.209(5)
<i>z</i>	0.6283(2)	0.825(2)	0.816(2)
$U_{\text{eq}}$	0.0138(5)	0.042(4)	0.058(4)
Zn in 2 <i>d</i> (1/3, 2/3, <i>z</i> )			
occupancy	0.78(3)	0.805(6)	0.791(5)
<i>z</i>	0.6283(2)	0.6262(3)	0.6259(2)
$U_{\text{eq}}$	0.0138(5)	0.0214(6)	0.0225(4)
As in 2 <i>d</i> (1/3, 2/3, <i>z</i> )			
<i>z</i>	0.26553(15)	0.24252(18)	0.24267(12)
$U_{\text{eq}}$	0.0105(3)	0.0141(4)	0.0137(3)
	<b>Dy<sub>0.53(1)</sub>Mn<sub>0.42(1)</sub>Zn<sub>1.58(1)</sub>As<sub>2</sub></b>	<b>Ho<sub>0.53(1)</sub>Mn<sub>0.39(1)</sub>Zn<sub>1.61(1)</sub>As<sub>2</sub></b>	<b>Er<sub>0.51(1)</sub>Mn<sub>0.38(1)</sub>Zn<sub>1.62(1)</sub>As<sub>2</sub></b>
<i>RE</i> in 1 <i>a</i> (0, 0, 0)			
occupancy	0.526(4)	0.526(4)	0.511(3)
$U_{\text{eq}}$	0.0192(4)	0.0223(5)	0.0203(4)
Mn in 2 <i>d</i> (1/3, 2/3, <i>z</i> )			
occupancy	0.210(6)	0.194(6)	0.190(5)
<i>z</i>	0.818(3)	0.818(3)	0.821(2)
$U_{\text{eq}}$	0.052(5)	0.053(5)	0.052(5)
Zn in 2 <i>d</i> (1/3, 2/3, <i>z</i> )			
occupancy	0.790(6)	0.806(6)	0.810(5)
<i>z</i>	0.6262(3)	0.6269(3)	0.6274(3)
$U_{\text{eq}}$	0.0250(6)	0.0258(6)	0.0244(5)
As in 2 <i>d</i> (1/3, 2/3, <i>z</i> )			
<i>z</i>	0.24278(16)	0.24212(17)	0.24177(15)
$U_{\text{eq}}$	0.0160(3)	0.0181(4)	0.0168(3)

	<b>Tm<sub>0.43(1)</sub>Mn<sub>0.21(1)</sub>Zn<sub>1.79(1)</sub>As<sub>2</sub></b>	<b>Yb<sub>0.95(1)</sub>Mn<sub>0.32(6)</sub>Zn<sub>1.68(6)</sub>As<sub>2</sub></b>	<b>Lu<sub>0.42(1)</sub>Mn<sub>0.20(1)</sub>Zn<sub>1.80(1)</sub>As<sub>2</sub></b>
<i>RE</i> in $1a$ (0, 0, 0)			
occupancy	0.434(3)	0.945(4)	0.419(3)
$U_{\text{eq}}$	0.0207(4)	0.01103(18)	0.0213(3)
<i>Mn</i> in $2d$ (1/3, 2/3, $z$ )			
occupancy	0.105(5)	0.16(3)	0.098(4)
$z$	0.830(4)	0.63102(15)	0.836(6)
$U_{\text{eq}}$	0.068(8)	0.0122(3)	0.076(9)
<i>Zn</i> in $2d$ (1/3, 2/3, $z$ )			
occupancy	0.895(5)	0.84(3)	0.902(4)
$z$	0.62910(16)	0.63102(15)	0.62957(16)
$U_{\text{eq}}$	0.0195(3)	0.0122(3)	0.0202(3)
<i>As</i> in $2d$ (1/3, 2/3, $z$ )			
$z$	0.23759(10)	0.25508(11)	0.23669(10)
$U_{\text{eq}}$	0.0137(2)	0.0094(3)	0.0139(2)

<sup>a</sup> $U_{\text{eq}}$  is defined as one-third of the trace of the orthogonalized  $U_{ij}$  tensor.

**Table 2.4** Atomic Coordinates and Equivalent Isotropic Displacement Parameters ( $\text{\AA}^2$ )  
for  $RE_{2-y}Mn_xZn_{4-x}As_4$  ( $RE = \text{La-Nd, Sm, Gd}$ ).<sup>a</sup>

	$\text{La}_{1.25(1)}\text{Mn}_{0.93(2)}\text{Zn}_{3.07(2)}\text{As}_4$	$\text{Ce}_{1.30(1)}\text{Mn}_{0.83(3)}\text{Zn}_{3.17(3)}\text{As}_4$	$\text{Pr}_{1.25(1)}\text{Mn}_{0.95(2)}\text{Zn}_{3.05(2)}\text{As}_4$
<i>RE1</i> in <i>1b</i> (0, 0, 1/2)			
occupancy	0.246(10)	0.300(10)	0.253(8)
$U_{\text{eq}}$	0.039(3)	0.036(2)	0.035(2)
<i>RE2</i> in <i>1a</i> (0, 0, 0)			
occupancy	1	1	1
$U_{\text{eq}}$	0.0165(4)	0.0185(4)	0.0147(3)
<i>Mn</i> in <i>2d</i> (1/3, 2/3, <i>z</i> )			
occupancy	0.466(12)	0.414(13)	0.477(10)
<i>z</i>	0.4095(8)	0.4099(10)	0.4087(7)
$U_{\text{eq}}$	0.034(3)	0.037(3)	0.038(2)
<i>Zn1</i> in <i>2d</i> (1/3, 2/3, <i>z</i> )			
occupancy	0.534(12)	0.586(13)	0.523(10)
<i>z</i>	0.3364(4)	0.3324(4)	0.3331(3)
$U_{\text{eq}}$	0.0230(16)	0.0225(15)	0.0215(11)
<i>Zn2</i> in <i>2d</i> (1/3, 2/3, <i>z</i> )			
occupancy	1	1	1
<i>z</i>	0.79987(16)	0.80160(18)	0.80174(13)
$U_{\text{eq}}$	0.0186(5)	0.0174(6)	0.0169(4)
<i>As1</i> in <i>2d</i> (1/3, 2/3, <i>z</i> )			
<i>z</i>	0.13326(12)	0.13196(14)	0.13056(9)
$U_{\text{eq}}$	0.0125(4)	0.0114(4)	0.0100(3)
<i>As2</i> in <i>2d</i> (1/3, 2/3, <i>z</i> )			
<i>z</i>	0.61635(14)	0.61568(16)	0.61690(11)
$U_{\text{eq}}$	0.0180(4)	0.0162(5)	0.0162(3)

	Nd <sub>1.25(1)</sub> Mn <sub>0.95(3)</sub> Zn <sub>3.05(3)</sub> As <sub>4</sub>	Sm <sub>1.24(1)</sub> Mn <sub>0.87(4)</sub> Zn <sub>3.13(4)</sub> As <sub>4</sub>	Gd <sub>1.24(1)</sub> Mn <sub>0.93(3)</sub> Zn <sub>3.07(3)</sub> As <sub>4</sub>
<i>RE1</i> in <i>1b</i> (0, 0, 1/2)			
occupancy	0.249(14)	0.240(10)	0.242(9)
$U_{\text{eq}}$	0.044(5)	0.031(3)	0.033(3)
<i>RE2</i> in <i>1a</i> (0, 0, 0)			
occupancy	1	1	1
$U_{\text{eq}}$	0.0132(5)	0.0226(6)	0.0166(4)
Mn in <i>2d</i> (1/3, 2/3, <i>z</i> )			
occupancy	0.476(17)	0.436(18)	0.468(15)
<i>z</i>	0.4097(12)	0.4086(14)	0.4079(11)
$U_{\text{eq}}$	0.031(4)	0.034(4)	0.034(3)
Zn1 in <i>2d</i> (1/3, 2/3, <i>z</i> )			
occupancy	0.524(17)	0.564(18)	0.533(15)
<i>z</i>	0.3339(7)	0.3324(7)	0.3318(6)
$U_{\text{eq}}$	0.020(2)	0.024(2)	0.0220(18)
Zn2 in <i>2d</i> (1/3, 2/3, <i>z</i> )			
occupancy	1	1	1
<i>z</i>	0.8020(2)	0.8035(2)	0.8037(2)
$U_{\text{eq}}$	0.0157(7)	0.0196(8)	0.0186(6)
As1 in <i>2d</i> (1/3, 2/3, <i>z</i> )			
<i>z</i>	0.12920(18)	0.12714(19)	0.12611(15)
$U_{\text{eq}}$	0.0091(5)	0.0132(6)	0.0105(4)
As2 in <i>2d</i> (1/3, 2/3, <i>z</i> )			
<i>z</i>	0.6176(2)	0.6185(2)	0.61946(17)
$U_{\text{eq}}$	0.0153(6)	0.0186(6)	0.0177(5)

<sup>a</sup> $U_{\text{eq}}$  is defined as one-third of the trace of the orthogonalized  $U_{ij}$  tensor.

**Table 2.5** Interatomic Distances (Å) for  $RE_{1-y}Mn_xZn_{2-x}As_2$  ( $RE = Eu-Lu$ ).

	$EuMn_{0.4}Zn_{1.6}As_2$	$Gd_{0.5}Mn_{0.4}Zn_{1.6}As_2$	$Tb_{0.5}Mn_{0.4}Zn_{1.6}As_2$
$RE-As$ ( $\times 6$ )	3.103(1)	2.876(2)	2.882(1)
$RE-Mn$ ( $\times 6$ )	3.624(2)	2.647(7)	2.678(7)
$Mn-As$ ( $\times 3$ )	2.561(1)	2.415(3)	2.408(3)
$Mn-As$	2.612(2)	2.799(15)	2.869(16)
$Zn-As$ ( $\times 3$ )	2.561(1)	2.530(2)	2.534(1)
$Zn-As$	2.612(2)	2.572(3)	2.577(2)
$Zn-Zn$ ( $\times 3$ )	3.064(2)	2.914(3)	2.917(2)
	$Dy_{0.5}Mn_{0.4}Zn_{1.6}As_2$	$Ho_{0.5}Mn_{0.4}Zn_{1.6}As_2$	$Er_{0.5}Mn_{0.4}Zn_{1.6}As_2$
$RE-As$ ( $\times 6$ )	2.876(1)	2.865(2)	2.873(2)
$RE-Mn$ ( $\times 6$ )	2.667(8)	2.660(10)	2.658(7)
$Mn-As$ ( $\times 3$ )	2.403(3)	2.396(4)	2.406(4)
$Mn-As$	2.857(18)	2.84(2)	2.830(16)
$Zn-As$ ( $\times 3$ )	2.527(1)	2.520(2)	2.527(3)
$Zn-As$	2.576(2)	2.578(5)	2.592(3)
$Zn-Zn$ ( $\times 3$ )	2.913(2)	2.910(3)	2.924(3)
	$Tm_{0.4}Mn_{0.2}Zn_{1.8}As_2$	$Yb_{1.0}Mn_{0.3}Zn_{1.7}As_2$	$Lu_{0.4}Mn_{0.2}Zn_{1.8}As_2$
$RE-As$ ( $\times 6$ )	2.847(1)	2.989(1)	2.838(1)
$RE-Mn$ ( $\times 6$ )	2.623(13)	3.516(1)	2.602(15)
$Mn-As$ ( $\times 3$ )	2.409(6)	2.533(1)	2.412(7)
$Mn-As$	2.72(3)	2.612(1)	2.66(4)
$Zn-As$ ( $\times 3$ )	2.527(1)	2.533(1)	2.525(1)
$Zn-As$	2.609(2)	2.612(1)	2.610(1)
$Zn-Zn$ ( $\times 3$ )	2.926(2)	3.018(1)	2.924(1)

**Table 2.6** Interatomic Distances (Å) for  $RE_{2-y}Mn_xZn_{4-x}As_4$  ( $RE = La-Nd, Sm, Gd$ ).

	$La_{1.2}Mn_{0.9}Zn_{3.1}As_4$	$Ce_{1.3}Mn_{0.8}Zn_{3.2}As_4$	$Pr_{1.2}Mn_{1.0}Zn_{3.0}As_4$
$RE1-As2$ ( $\times 6$ )	2.878(2)	2.867(3)	2.875(1)
$RE1-Mn$ ( $\times 6$ )	2.700(5)	2.693(7)	2.698(4)
$RE2-As1$ ( $\times 6$ )	3.012(2)	2.994(3)	2.981(1)
$Mn-As2$ ( $\times 3$ )	2.427(2)	2.425(4)	2.423(1)
$Mn-As2$	2.821(11)	2.792(14)	2.823(9)
$Zn1-As2$ ( $\times 3$ )	2.486(2)	2.501(3)	2.492(1)
$Zn1-As1$	2.771(6)	2.719(7)	2.747(5)
$Zn2-As2$	2.503(3)	2.523(4)	2.507(2)
$Zn2-As1$ ( $\times 3$ )	2.569(2)	2.563(3)	2.568(1)
$Zn1-Zn2$ ( $\times 3$ )	3.037(4)	3.010(5)	3.016(3)
	$Nd_{1.2}Mn_{1.0}Zn_{3.0}As_4$	$Sm_{1.2}Mn_{0.9}Zn_{3.1}As_4$	$Gd_{1.2}Mn_{0.9}Zn_{3.1}As_4$
$RE1-As2$ ( $\times 6$ )	2.864(2)	2.869(2)	2.873(2)
$RE1-Mn$ ( $\times 6$ )	2.677(7)	2.682(9)	2.683(7)
$RE2-As1$ ( $\times 6$ )	2.955(2)	2.936(2)	2.924(1)
$Mn-As2$ ( $\times 3$ )	2.412(3)	2.409(3)	2.406(2)
$Mn-As2$	2.808(16)	2.835(19)	2.856(14)
$Zn1-As2$ ( $\times 3$ )	2.472(3)	2.472(3)	2.467(2)
$Zn1-As1$	2.766(9)	2.772(10)	2.777(8)
$Zn2-As2$	2.493(4)	2.499(4)	2.488(3)
$Zn2-As1$ ( $\times 3$ )	2.558(2)	2.559(2)	2.559(1)
$Zn1-Zn2$ ( $\times 3$ )	3.009(6)	3.006(7)	3.000(5)

### 2.2.3 Band Structure Calculation

Tight-binding linear muffin tin orbital band structure calculations were performed within the local density and atomic spheres approximation with use of the Stuttgart TB-LMTO-ASA program (version 4.7).<sup>58</sup> With cell parameters and atomic coordinates taken from the experimental crystal structure of  $La_{1.3}Mn_{0.9}Zn_{3.1}As_4$ , an idealized model “ $La_{1.33}MnZn_3As_4$ ” was considered, based on a hypothetical  $\sqrt{3}a \times \sqrt{3}a$  superstructure in the lower-symmetry space group  $P31m$  (no. 157) and an ordered

distribution of the partially occupied La1 (33%), Mn (50%), and Zn1 (50%) sites. The basis set consisted of La 6s/6p/5d/4f, Mn 4s/4p/3d, Zn 4s/4p/3d, and As 4s/4p orbitals, with the La 6p and As 4d orbitals being downfolded. Integrations in reciprocal space were carried out with an improved tetrahedron method over 384 irreducible  $k$ -points with the first Brillouin zone. The calculations were performed initially without spin polarization and then repeated with spin polarization included.

#### 2.2.4 XPS Analysis

$\text{YbMn}_{0.3}\text{Zn}_{1.7}\text{As}_2$ ,  $\text{Er}_{0.5}\text{Mn}_{0.4}\text{Zn}_{1.6}\text{As}_2$ , and  $\text{Nd}_{1.2}\text{Mn}_{1.0}\text{Zn}_{3.0}\text{As}_4$  were chosen as representative samples to be examined by XPS.  $\text{Yb}_2\text{O}_3$  was also measured as a standard sample containing trivalent Yb. XPS spectra were collected on a Kratos AXIS Ultra spectrometer equipped with a monochromatic Al  $K\alpha$  X-ray source (operated at 12 mA and 12 kV) and a hybrid lens (with spot size of  $700 \mu\text{m} \times 400 \mu\text{m}$ ). The samples were finely ground, pressed into pellets (6 mm diameter, 1–3 mm thickness), and secured onto a sample bar with double-sided tape. The samples were transferred via a load-lock into the analysis chamber, which was held at a pressure between  $10^{-7}$  and  $10^{-9}$  Pa. The samples were sputter-cleaned with an  $\text{Ar}^+$ -ion beam (4 kV, 10 mA) until the intensity of the O 1s peak remained constant, indicating that no further surface oxides could be removed.  $\text{Yb}_2\text{O}_3$ ,  $\text{Er}_{0.5}\text{Mn}_{0.4}\text{Zn}_{1.6}\text{As}_2$ , and  $\text{Nd}_{1.2}\text{Mn}_{1.0}\text{Zn}_{3.0}\text{As}_4$  were each sputtered for five minutes, whereas  $\text{YbMn}_{0.3}\text{Zn}_{1.7}\text{As}_2$  required an additional five minutes of sputtering to reduce background noise levels. The presence of a shoulder in the Mn 2p spectra indicated that slight reduction occurred as a result of this  $\text{Ar}^+$  sputtering procedure. Survey spectra were collected with pass energy of 80 eV, step size of 0.4 eV, and dwell time of 0.1 s over the range of 1100 to 0 eV. They confirmed the presence of all

expected elements. High resolution Yb 4d and Mn 2p spectra were collected with pass energy of 20 eV, step size of 0.1 eV, and dwell time of 0.2 s over ranges determined from the survey spectra. These spectra were calibrated to the C 1s peak located at 284.8 eV arising from adventitious carbon. Because the Mn 2p signal for  $\text{YbMn}_{0.3}\text{Zn}_{1.7}\text{As}_2$  was found to be weaker than the others, this spectrum was collected with a step size of 0.05 eV. All spectra were analyzed with use of the CasaXPS software package.<sup>59</sup> The background was removed through a Shirley function and the peaks were fitted to pseudo-Voigt (70% Gaussian and 30% Lorentzian) profiles to account for instrumental and experimental broadening effects. The uncertainty of this spectrometer is generally estimated as better than  $\pm 0.1$  eV on the basis of previous measurements, but this must be counterbalanced by the relatively low concentration of Mn in these samples. Charge neutralization was required only for the  $\text{Yb}_2\text{O}_3$  standard and was applied to maximize signal intensity and minimize peak width.

### 2.3 Results and Discussion

Within ternary  $RE\text{-Zn-As}$  systems,  $\text{CaAl}_2\text{Si}_2$ -type phases were previously restricted to  $RE\text{Zn}_2\text{As}_2$  ( $RE = \text{Eu, Yb}$ ), containing divalent  $RE$  components only.<sup>27,28,45-48</sup> They have been recently extended to  $RE_{0.67}\text{Zn}_2\text{As}_2$  ( $RE = \text{La-Nd, Sm}$ ), containing early trivalent  $RE$  components but with formation of defects to satisfy the ideal electron count of  $16 e^-/\text{f.u.}$ <sup>24</sup> We initially attempted to prepare the defective  $RE_{0.67}\text{Zn}_2\text{As}_2$  phases containing later trivalent  $RE$  components ( $RE = \text{Gd-Tm, Lu}$ ), using various synthetic conditions ranging from 750 °C to 1050 °C, but were unsuccessful. Given the existence of the Mn-containing counterparts  $RE\text{Mn}_2\text{As}_2$  ( $RE = \text{Eu, Yb}$ ),<sup>60</sup> we also attempted to prepare defective  $RE_{0.67}\text{Mn}_2\text{As}_2$  phases containing various trivalent  $RE$  components, to no

avail. Thus, it was surprising to discover that *partial* Mn substitution enables the preparation of two extensive series of quaternary arsenides,  $RE_{1-y}Mn_xZn_{2-x}As_2$  ( $RE =$  Eu-Lu) and  $RE_{2-y}Mn_xZn_{4-x}As_4$  ( $RE =$  La-Nd, Sm, Gd), for all possible  $RE$  components (except Pm, of course). The syntheses of these compounds are beset by difficulties posed by volatilization of Zn and As at high temperatures, so that the products normally contain admixtures of binary arsenides such as  $Zn_3As_2$ . However, slow cooling from 1050 °C to 500 °C was successful in the growth of single crystals to permit detailed structural analysis. Further optimization of synthetic conditions is in progress to improve the phase purity of these samples.

Individual  $RE$  members from these series were characterized by single-crystal structure determinations. The average compositions obtained from structure refinements were  $RE_{1.3}Mn_{0.9}Zn_{3.1}As_4$  ( $RE =$  Eu, Yb),  $RE_{0.5}Mn_{0.4}Zn_{1.6}As_2$  ( $RE =$  Gd-Tm, Lu), and  $RE_{1.3}Mn_{0.9}Zn_{3.1}As_4$  ( $RE =$  La-Nd, Sm, Gd). For concreteness and simplicity, we use these average formulas in subsequent discussion when referring to these sets of compounds. They crystallize in the trigonal space group  $P\bar{3}m1$ , but the  $c$ -axis is doubled in  $RE_{1.3}Mn_{0.9}Zn_{3.1}As_4$ , which can be regarded as a superstructure of  $RE_{0.5}Mn_{0.4}Zn_{1.6}As_2$ . A plot of the cell parameters (with  $c$ -axis and cell volume  $V$  halved in  $RE_{1.3}Mn_{0.9}Zn_{3.1}As_4$  for comparison to the subcell) illustrates the expected lanthanide contraction, but with deviations observed for members containing the larger divalent Eu and Yb components (**Figure 2.2**).

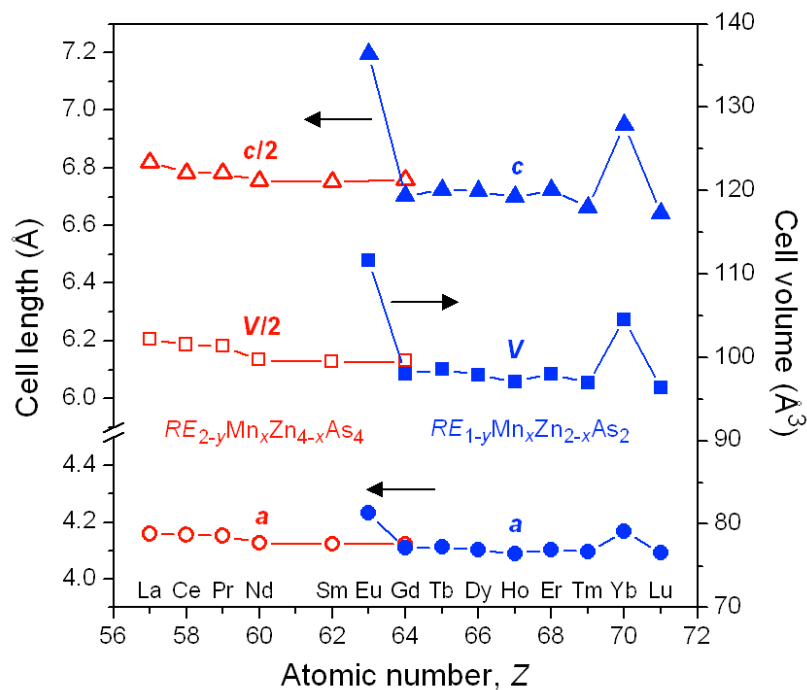


**Figure 2.2** Plots of cell parameters for  $RE\text{Mn}_{0.5}\text{Zn}_{1.5}\text{As}_2$  ( $RE = \text{Eu}, \text{Yb}$ ),  $RE_{0.5}\text{Mn}_{0.4}\text{Zn}_{1.6}\text{As}_2$  ( $RE = \text{Gd-Tm}, \text{Lu}$ ), and  $RE_{1.3}\text{Mn}_{0.9}\text{Zn}_{3.1}\text{As}_4$  ( $RE = \text{La-Nd}, \text{Sm}, \text{Gd}$ ).

The parent  $\text{CaAl}_2\text{Si}_2$ -type structure is retained for  $RE\text{Mn}_{0.4}\text{Zn}_{1.6}\text{As}_2$  ( $RE = \text{Eu}, \text{Yb}$ ), in which a disordered mixture of Mn and Zn atoms occupy the unique transition-metal site, surrounded by As atoms forming  $M$ -centred tetrahedra that share their edges to build up  $[M_2\text{As}_2]$  slabs. These slabs are interleaved with hexagonal nets of fully occupied  $RE$  sites, each surrounded by As atoms in octahedral geometry (**Figure 2.3a**). These quaternary arsenides may be assumed to be members of solid solutions formed between the known parent ternary arsenides  $RE\text{Mn}_2\text{As}_2$ <sup>60</sup> and  $RE\text{Zn}_2\text{As}_2$  (for  $RE = \text{Eu}, \text{Yb}$ ).<sup>27,28,45-48</sup> Indeed, for the Eu-containing quaternary compound, the cell parameters ( $a = 4.234(2)$  Å,  $c = 7.198(4)$  Å) are intermediate between those of  $\text{EuMn}_2\text{As}_2$  ( $a = 4.287(1)$  Å,  $c = 7.225(1)$  Å)<sup>60</sup> and  $\text{EuZn}_2\text{As}_2$  ( $a = 4.211(1)$  Å,  $c = 7.181(1)$  Å).<sup>27</sup> If a linear relationship is assumed between cell parameters and concentration (Vegard's law), a composition of

30% Mn and 70% Zn is obtained, in good agreement with the precise composition of  $\text{EuMn}_{0.5}\text{Zn}_{1.5}\text{As}_2$  determined in the structure refinement. However, comparison of the cell parameters for the Yb-containing quaternary compound ( $a = 4.168(1) \text{ \AA}$ ,  $c = 6.948(1) \text{ \AA}$ ) with those of  $\text{YbMn}_2\text{As}_2$  ( $a = 4.226(3) \text{ \AA}$ ,  $c = 6.964(5) \text{ \AA}$ )<sup>60</sup> and  $\text{YbZn}_2\text{As}_2$  ( $a = 4.157(1) \text{ \AA}$ ,  $c = 6.954(1) \text{ \AA}$ )<sup>48</sup> reveals anomalous behavior. Although the  $a$ -parameter is intermediate and suggests a composition of 83% Zn, in agreement with the refined formula  $\text{YbMn}_{0.3}\text{Zn}_{1.7}\text{As}_2$ , the  $c$ -parameter is even lower than for the end-members (i.e., a negative deviation from Vegard's law). Mixed valency of Yb has been proposed in  $\text{YbZn}_2\text{As}_2$ , with evidence taken from magnetic measurements.<sup>48</sup> The introduction of smaller  $\text{Yb}^{3+}$  species, whose concentration could conceivably vary within a solid solution, would then act to contract the unit cell parameters more than expected. Alternatively, there may be subtle effects related to the competition between inequivalent Zn–As vs. Mn–As bonds within the tetrahedral sites, as discussed below, that are responsible for this anomaly. Elucidation of the full solid solutions  $\text{REMn}_x\text{Zn}_{2-x}\text{As}_2$  ( $RE = \text{Eu}, \text{Yb}$ ) and determination of the crystal structures of additional members will be helpful in clarifying these effects.

The formation of these quaternary arsenides  $\text{REMn}_{0.4}\text{Zn}_{1.6}\text{As}_2$  ( $RE = \text{Eu}, \text{Yb}$ ) also tests an important structural feature of  $\text{CaAl}_2\text{Si}_2$ -type phases. Within the  $M$ -centred tetrahedra, there is an inequivalence between the three lateral or “rib” bonds and the one vertical or “handle” bond. Both experimental observations and theoretical studies indicate that the three rib bonds are normally shorter than the handle bond for  $M$  atoms with  $d^0$  (e.g., Mg, Al) and  $d^{10}$  configurations (e.g., Zn, Cd),<sup>9</sup> whereas the trend is more muted or even reversed for  $M$  atoms with  $d^5$  configurations (e.g., Mn).<sup>2</sup> Although full

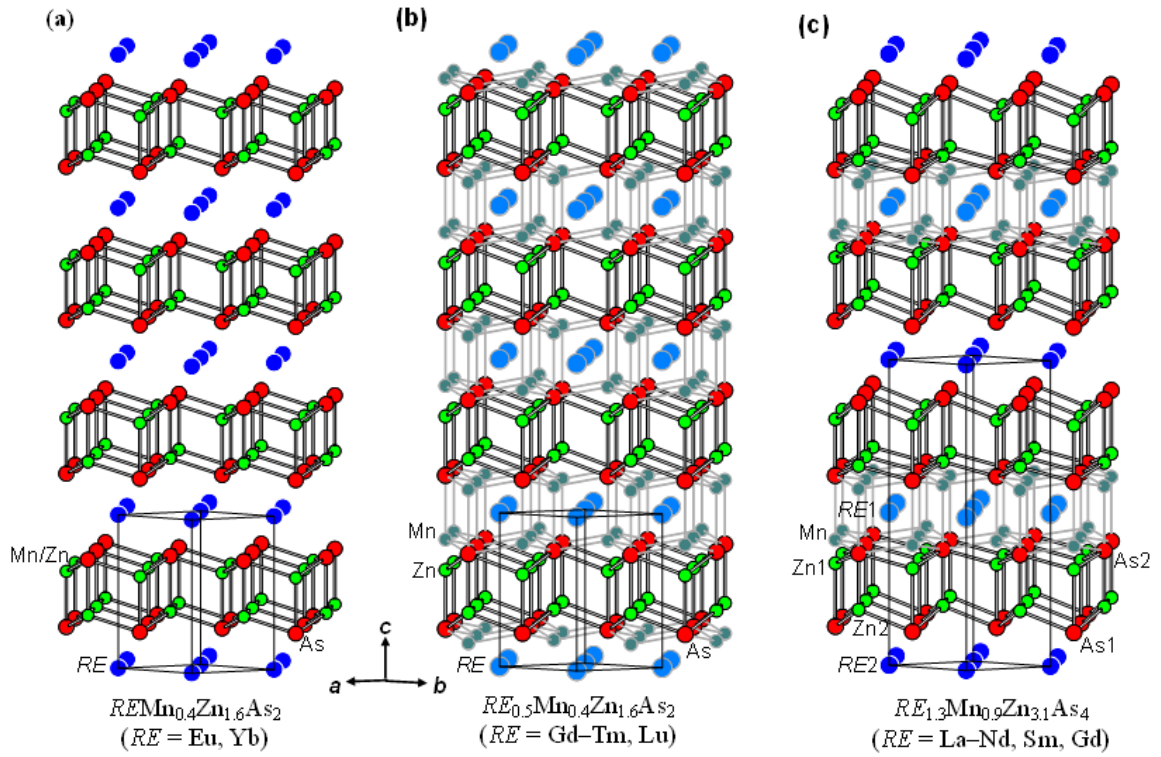


**Figure 2.3** (a)  $RE_{0.4}Mn_{0.4}Zn_{1.6}As_2$  ( $RE = Eu, Yb$ ) with  $CaAl_2Si_2$ -type structure, (b)  $RE_{0.5}Mn_{0.4}Zn_{1.6}As_2$  ( $RE = Gd-Tm, Lu$ ) with defect  $CaAl_2Si_2$ -type structure, and (c)  $RE_{1.3}Mn_{0.9}Zn_{3.1}As_4$  ( $RE = La-Nd, Sm, Gd$ ) with partially ordered defect  $CaAl_2Si_2$ -type structure; all contain  $[M_2As_2]$  slabs alternately stacked with nets of  $RE$  atoms. The  $RE$  sites are either fully (dark blue) or partially occupied (faded blue). The interstitial Mn sites are partially occupied (faded blue-green). The Zn sites in (b) and the Zn1 sites in (c) are partially occupied (green).

crystal structures are not available for all the parent ternary arsenides  $RE_{2}MnAs_2$  and  $REZn_2As_2$  ( $RE = Eu, Yb$ ), their bond lengths can be estimated with the assumption of atomic coordinates taken from related  $CaAl_2Si_2$ -type structures. The distinction predicted for these two types of  $M-As$  bonds, depending on the d-configuration of  $M$ , is demonstrated clearly in  $EuMn_2As_2$  (2.622 Å ribs, 2.601 Å handle) vs.  $EuZn_2As_2$  (2.549 Å ribs, 2.614 Å handle) (**Figure 2.4**), and in  $YbMn_2As_2$  (2.579 Å ribs, 2.507 Å handle) vs.  $YbZn_2As_2$  (2.520 Å ribs, 2.595 Å handle). The driving force for this bond inequivalence

is the filling of some antibonding states for the handle bonds near the Fermi level, which can be avoided in the  $d^5$  case if a low-spin configuration is adopted.<sup>2,9</sup> In the quaternary arsenides, the larger concentration of Zn atoms and the greater electronic flexibility of Mn atoms together result in the normal situation of shorter rib than handle bonds (i.e., 2.561(2) Å ribs, 2.612(2) Å handle in  $\text{EuMn}_{0.5}\text{Zn}_{1.5}\text{As}_2$  (**Figure 2.4**); 2.533(1) Å ribs, 2.612(1) Å handle in  $\text{YbMn}_{0.3}\text{Zn}_{1.7}\text{As}_2$ ).

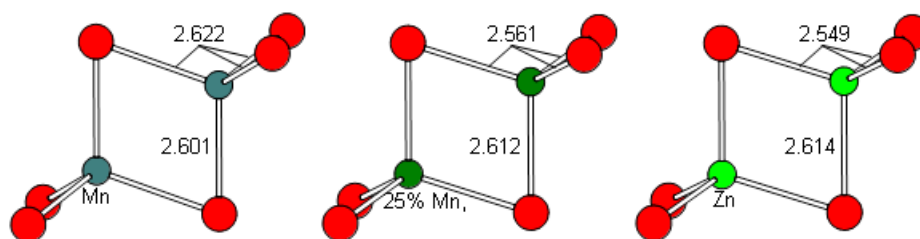


**Figure 2.4** Lengths (Å) of rib and handle bonds within metal-centred tetrahedra in  $\text{EuMn}_2\text{As}_2$  (left),  $\text{EuMn}_{0.4}\text{Zn}_{1.6}\text{As}_2$  (centre), and  $\text{EuZn}_2\text{As}_2$  (right).

Replacing the divalent *RE* with late trivalent *RE* metals results in the series of quaternary arsenides  $\text{RE}_{0.5}\text{Mn}_{0.4}\text{Zn}_{1.6}\text{As}_2$  ( $\text{RE} = \text{Gd-Tm, Lu}$ ) containing deficiencies in the *RE* site as well as a secondary transition-metal site close to the original one. Because refinements suggest a preference of Zn atoms for the primary site and Mn atoms for the secondary site, we have assumed an ordered model. The Zn atoms reside within  $[\text{Zn}_{1.6}\text{As}_2]$  slabs, whereas the Mn atoms partially occupy ( $\sim 0.2$ ) interstitial sites located above and below these slabs, in the space made available by the *RE* vacancies (**Figure 2.3b**). The Zn-centred tetrahedra within the slabs exhibit shorter rib (2.52–2.53 Å) than handle Zn–As bonds (2.57–2.61 Å), in accordance with expectations; the As–Zn–As angles around the base of these tetrahedra (108.3–108.6°) remain similar to those (110.7–

111.5°) in  $RE\text{Mn}_{0.4}\text{Zn}_{1.6}\text{As}_2$  ( $RE = \text{Eu}, \text{Yb}$ ). The Mn atoms are also surrounded in tetrahedral geometry by three As atoms capping one  $[\text{Zn}_{1.6}\text{As}_2]$  slab and a fourth As atom capping the adjacent  $[\text{Zn}_{1.6}\text{As}_2]$  slab. These Mn-centred tetrahedra are more distorted, with much shorter Mn–As (2.40–2.42 Å) than Mn–Mn (2.66–2.87 Å) and wider As–Mn–As angles (116.1–117.4°) around the base of these tetrahedra. Perhaps a better description of the Mn coordination is CN3+1.

The appearance of  $RE$  defects in quaternary arsenides  $RE_{0.5}\text{Mn}_{0.4}\text{Zn}_{1.6}\text{As}_2$  ( $RE = \text{Gd–Tm}, \text{Lu}$ ) can be rationalized in the same way as in the previously reported ternary arsenides  $RE_{0.67}\text{Zn}_2\text{As}_2$  ( $RE = \text{La–Nd}, \text{Sm}$ ),<sup>24</sup> namely to reduce the number of valence electrons to satisfy charge balance requirements when trivalent  $RE$  components are introduced. If divalent Mn and Zn atoms are assumed, the ideal charge-balanced formula should be “ $RE_{0.67}\text{Mn}_{0.4}\text{Zn}_{1.6}\text{As}_2$ ”, but the observed  $RE$  deficiencies are somewhat more pronounced. It should be noted that a slight deviation was also seen in  $\text{Ce}_{0.63}\text{Zn}_2\text{As}_2$ , the only member of  $RE_{0.67}\text{Zn}_2\text{As}_2$  that has been structurally refined.<sup>24</sup> Alternatively, the formula  $RE_{0.5}\text{Mn}_{0.4}\text{Zn}_{1.6}\text{As}_2$  would be almost perfectly charge-balanced if  $\text{Mn}^{3+}$  species are assumed instead. In any event, these chemical formulas should be accepted cautiously because structural refinements of occupancies may be correlated with other factors (such as absorption corrections). Moreover, as mentioned in the introduction, exceptions to the ideal electron count are permissible when there is no band gap at the Fermi level, a notion to be tested by a band structure calculation discussed further below. As in  $RE_{0.67}\text{Zn}_2\text{As}_2$  ( $RE = \text{La–Nd}, \text{Sm}$ ), no vacancy ordering was apparent in  $RE_{0.5}\text{Mn}_{0.4}\text{Zn}_{1.6}\text{As}_2$  ( $RE = \text{Gd–Tm}, \text{Lu}$ ), as evaluated by the absence of superstructure reflections or diffuse scattering in the X-ray diffraction patterns (**Figure A 1.1** and

**Figure 2.1).** In the related ternary sulphides  $RE_{0.67}Cu_2S_2$  which also adopt defect  $CaAl_2Si_2$ -type structures, there is evidence that short-range ordering may take place.<sup>61,62</sup> Various stacking sequences can be envisioned for the hexagonal  $RE$  nets, each containing an ordered distribution of 33% vacancies (and 67% occupied sites), such that proximity of  $RE$  vacancies in adjacent nets is avoided. Long-range ordering within these sequences is frustrated by the occurrence of frequent stacking faults. The situation in  $RE_{0.5}Mn_{0.4}Zn_{1.6}As_2$  ( $RE = Gd-Tm, Lu$ ) is complicated by the occurrence of vacancies not only in the  $RE$  sites, but also in the Mn and Zn sites.

It is thus remarkable that partial long-range ordering does occur, in a different manner than described above, through substitution with the early trivalent  $RE$  metals in the series  $RE_{1.3}Mn_{0.9}Zn_{3.1}As_4$  ( $RE = La-Nd, Sm, Gd$ ). The formula is nearly twice that of  $RE_{0.5}Mn_{0.4}Zn_{1.6}As_2$ , reflecting a doubling of the  $c$ -parameter. In this superstructure, hexagonal nets of completely filled  $RE_2$  sites alternately stack with nets of partially filled ( $\sim 0.3$ )  $RE_1$  sites (**2.3c**). Within the  $[Zn_{1.6}As_2]$  slabs, there is now a differentiation between fully occupied Zn2 sites adjacent to the filled  $RE_2$  nets and partially occupied ( $\sim 0.6$ ) Zn1 sites adjacent to the defective  $RE_1$  nets. As before, the Mn atoms reside in interstitial sites within the defective layers. Curiously, although the Zn1-centred tetrahedra retain the expected distinction of bonds to the surrounding As atoms (shorter ribs, 2.47–2.50 Å; longer handle, 2.72–2.78 Å), the Zn2-centred tetrahedra show a reversal (longer ribs, 2.56–2.57 Å; shorter handle, 2.49–2.52 Å). Although the structure refinements do indicate clear site preferences for the Mn and Zn atoms, partial disorder cannot be completely ruled out, which may account for this bond length reversal. We think that the combination of substitutional and positional disorder (Mn vs. Zn) and the

presence of *RE* defects present many competing size and electronic factors that complicate the structural analysis. For example, an alternative explanation for the rather short Zn1–As2 and Mn–As2 distances of  $\sim 2.5$  Å is that they compensate for the “underbonding” of the As2 atoms next to vacant *RE1* sites. Moreover, there is growing recognition that in  $AB_2X_2$  compounds with the  $\text{CaAl}_2\text{Si}_2$ -type structure, the *A* cations may participate in covalent interactions with the  $[B_2X_2]$  slabs, notwithstanding earlier assumptions that their role was not significant.<sup>14</sup> The contrast between the partially ordered series  $RE_{1.3}\text{Mn}_{0.9}\text{Zn}_{3.1}\text{As}_4$  (formed for the earlier *RE* metals) and the disordered series  $RE_{0.5}\text{Mn}_{0.4}\text{Zn}_{1.6}\text{As}_2$  (formed for the later *RE* metals) suggests that such interactions may indeed be important. Note that the *RE1*–As2 distances straddling the interstitial Mn sites are nearly invariant (2.86–2.88 Å), whereas the *RE2*–As1 distances decrease gradually (from 3.01 Å in the La member to 2.92 Å in the Gd member); these observations suggest that Mn–As bonds dictate the spacing between one pair of  $[\text{Zn}_{1.6}\text{As}_2]$  slabs, while *RE*–As bonds are optimal between the other pair of  $[\text{Zn}_{1.6}\text{As}_2]$  slabs.

With slightly different loading compositions used in the syntheses of the Gd-containing compounds, members belonging to both series,  $\text{Gd}_{0.5}\text{Mn}_{0.4}\text{Zn}_{1.6}\text{As}_2$  and  $\text{Gd}_{1.2}\text{Mn}_{0.9}\text{Zn}_{3.1}\text{As}_4$ , could be obtained. In principle, vacancy ordering could be promoted through use of extended annealing times and slow cooling. Although these procedures do improve crystal quality (as gauged by sharpness of X-ray diffraction peaks), they did not alleviate the disorder even in the  $\text{Gd}_{1.2}\text{Mn}_{0.9}\text{Zn}_{3.1}\text{As}_4$  superstructure. We have investigated the possibility for the existence of a solid solution through preliminary experiments with loading compositions “ $\text{Gd}_{0.67}\text{Mn}_x\text{Zn}_{2-x}\text{As}_2$ ” (for  $x = 0, 0.05, 0.1, 0.3,$

0.5, 1.0, 1.5, 2.0) adhering to the ideal electron count. The products were not single-phase and contained admixtures of various binary arsenides, probably because of problems with volatilization described earlier. It appears that  $\text{CaAl}_2\text{Si}_2$ -type phases can be formed up to a Mn loading composition of  $x = 1.0$  (i.e., 50% Mn), and evidence for superstructure peaks occurs for loading compositions of  $x = 0.3$ – $1.0$  (i.e., 15–50% Mn) (**Figure A 1.4**); the true compositions undoubtedly contain lower Mn concentrations. The ternary end-member “ $\text{Gd}_{0.67}\text{Mn}_2\text{As}_2$ ” did not form. In addition to the disorder of Mn and Zn atoms, there is also the possibility for a homogeneity range in the Gd content, which will require future investigations on  $\text{Gd}_{1-y}\text{Mn}_x\text{Zn}_{2-x}\text{As}_2$  to probe the extent of Gd deficiencies ( $y$ ).

The partial substitution of Mn ( $d^5$ ) for Zn ( $d^{10}$ ) presents an interesting scenario for the electronic structure. A small band gap is expected for most  $AB_2X_2$  phases with the  $\text{CaAl}_2\text{Si}_2$ -type structure when the  $B$  component has a  $d^{10}$  (or  $d^0$ ) configuration. However, the Fermi level will necessarily cross a d-band when the  $B$  component has a  $d^5$  configuration, as previously shown for a  $[\text{Mn}_2\text{P}_2]^{2-}$  slab.<sup>2</sup> Taking the idealized formula

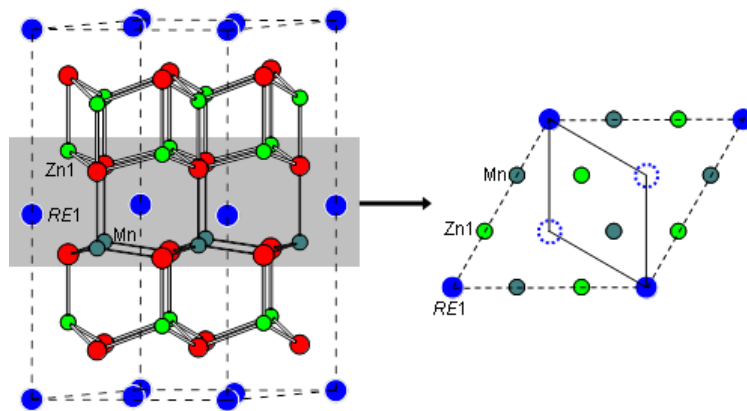


**Figure 2.5** Possible  $\sqrt{3}a \times \sqrt{3}a$  superstructure (with unit cell outlined in dashed lines) for idealized model “ $\text{La}_{1.33}\text{MnZn}_3\text{As}_4$ ” containing ordered occupation of 33% La, 50% Mn, and 50% Zn1 sites.

“La<sub>1.33</sub>MnZn<sub>3</sub>As<sub>4</sub>”, which would be electron-precise if divalent Mn and Zn atoms are assumed, we can propose a  $\sqrt{3}a \times \sqrt{3}a$  superstructure (**Figure 2.5**).

The La1 nets contain an ordered distribution of the 33% filled sites. The Mn and Zn1 sites, each 50% occupied, are within  $\sim 1.0$  Å of each other and cannot be simultaneously occupied within the same slab (**Figure 2.3c**). Instead, we imagine that they segregate into [MnZnAs<sub>2</sub>] and [Zn<sub>2</sub>As<sub>2</sub>] slabs, with long 2.8 Å Mn–As bonds connecting them. The density of states (DOS) curve for this hypothetical superstructure was determined from band structure calculations (**Figure 2.6**). The features of the DOS curve are generally consistent with the formulation “(La<sup>3+</sup>)<sub>1.33</sub>(Mn<sup>2+</sup>)(Zn<sup>2+</sup>)<sub>3</sub>(As<sup>3-</sup>)<sub>4</sub>” derived from the Zintl concept in which the electropositive La atoms fully transfer their valence electrons to the anionic slabs. Thus, empty La-based states are mostly found above the Fermi level, and filled As 4s and 4p states are found below. The Zn 3d states are completely filled (–8 eV) whereas the Mn 3d states are partially filled (–1 to +1 eV).

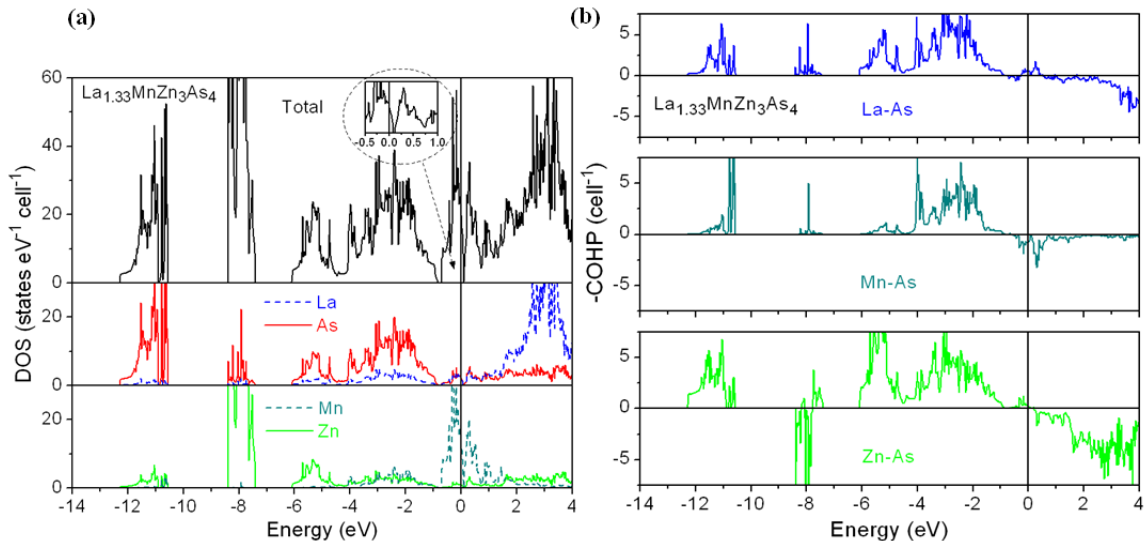


**Figure 2.6** (a) Density of states (DOS) and its atomic projections for “La<sub>1.33</sub>MnZn<sub>3</sub>As<sub>4</sub>”. (b) Crystal orbital Hamilton population (COHP) curves for La–As, Mn–As, and Zn–As interactions. The Fermi level is at 0 eV.

Most of the bonding stability comes from the occupation of Mn–As and Zn–As bonding levels, derived from significant mixing of Mn 3d or Zn 3d with As 4s/4p states, but there are also important covalent contributions to La–As bonding, as seen in the crystal orbital Hamilton population (COHP) curves (**Figure 2.6**). The integrated COHP values (–ICOHP) are 2.4 eV/bond for Mn–As, 1.7 eV/bond for Zn–As, and 1.0 eV/bond for La–As interactions. Note that the states near the Fermi level are antibonding for the Mn–As interactions, but only weakly bonding for the Zn–As and La–As interactions. Thus the possibility exists to alleviate the antibonding Mn–As interactions by reducing the electron count to lower the Fermi level slightly. This partial oxidation could be manifested experimentally through greater La or Mn deficiencies, as suggested by the formula  $\text{La}_{1.2}\text{Mn}_{0.9}\text{Zn}_{3.1}\text{As}_4$  refined in the structure determination, or by invoking the presence of some  $\text{Mn}^{3+}$  species.

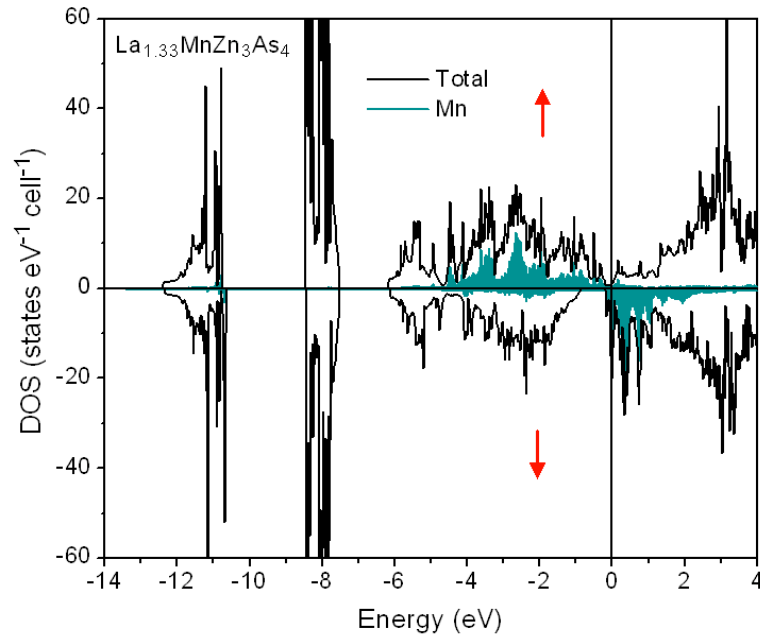


**Figure 2.7** DOS curve for spin-polarized “ $\text{La}_{1.33}\text{MnZn}_3\text{As}_4$ ”, with contributions from Mn states identified by the shaded regions.

Low-spin Mn is implicit in the filling of the d-band near the Fermi level, but the conclusions are unchanged if high-spin Mn is assumed, for which there would be an even greater driving force to reduce the electron count. The large spike in the DOS near the Fermi level is derived from mostly Mn 3d states and suggests an electronic instability. In a spin-polarized calculation of  $\text{La}_{1.33}\text{MnZn}_3\text{As}_4$ , the DOS curve reveals that such a high polarization is indeed predicted (**Figure 2.7**), with a large energy stabilization of 2.6 eV/cell. The magnetic moment is calculated to be  $3.6 \mu_B$ . This compound is nearly a ferromagnetic half-metal: for the spin-up electrons, the Fermi level falls in a pseudogap with almost zero DOS, whereas for the spin-down electrons, it intersects the bottom of the conduction band.

To acquire experimental evidence for the valence state assignments, XPS spectra were collected for  $\text{YbMn}_{0.3}\text{Zn}_{1.7}\text{As}_2$ ,  $\text{Er}_{0.5}\text{Mn}_{0.4}\text{Zn}_{1.6}\text{As}_2$ , and  $\text{Nd}_{1.2}\text{Mn}_{1.0}\text{Zn}_{3.0}\text{As}_4$ , as representative members of the different series of quaternary arsenides. Among the *RE* components, only the Yb valence is really subject to question. The Yb 4d spectrum for  $\text{YbMn}_{0.3}\text{Zn}_{1.7}\text{As}_2$ , obtained after a sputtering procedure had been applied to eliminate surface oxides, reveals the presence of both  $\text{Yb}^{2+}$  and  $\text{Yb}^{3+}$  (**Figure 2.8a**). The Yb  $4d_{5/2}$  core-line peak at 184.9 eV is identical to that in  $\text{Yb}_2\text{O}_3$ , measured as a  $\text{Yb}^{3+}$ -containing standard. Many of the undulations in the fine structure for  $\text{YbMn}_{0.3}\text{Zn}_{1.7}\text{As}_2$  are also found in  $\text{Yb}_2\text{O}_3$ , with the exception of a prominent low-energy shoulder at 181.3 eV that is consistent with the 4d core-line peak for  $\text{Yb}^{2+}$ .<sup>63</sup> In a similar XPS study on the related antimonide  $\text{YbZn}_2\text{Sb}_2$ , both  $\text{Yb}^{2+}$  and  $\text{Yb}^{3+}$  were also found to be present but it was suggested that formation of  $\text{Yb}_2\text{O}_3$  within grain boundaries is likely responsible for the

residual  $\text{Yb}^{3+}$  signature.<sup>19</sup> Given this caveat, the occurrence of mixed-valent Yb in  $\text{YbMn}_{0.3}\text{Zn}_{1.7}\text{As}_2$  remains inconclusive.

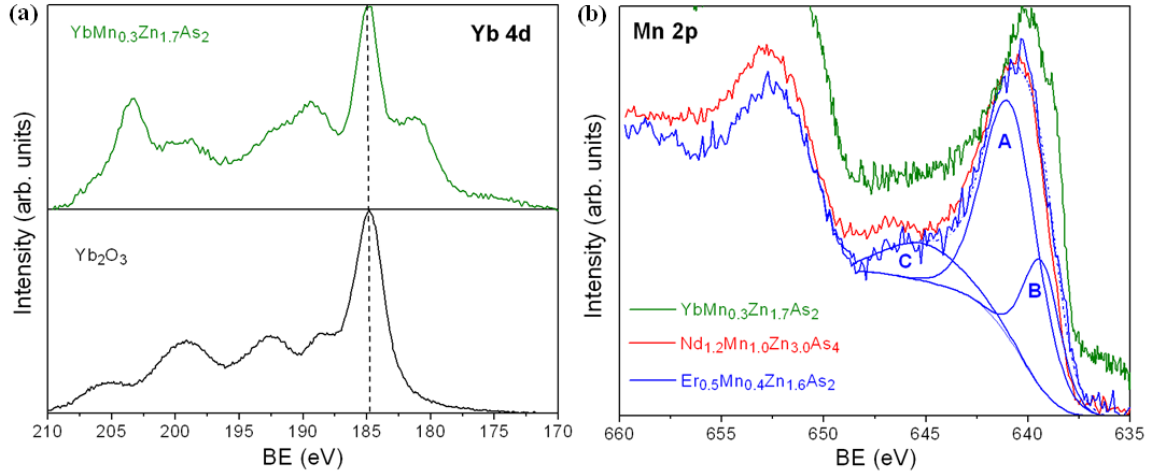


**Figure 2.8** (a) Yb 4d XPS spectra for  $\text{YbMn}_{0.3}\text{Zn}_{1.7}\text{As}_2$  and  $\text{Yb}_2\text{O}_3$ . (b) Mn 2p XPS spectra for  $\text{YbMn}_{0.3}\text{Zn}_{1.7}\text{As}_2$ ,  $\text{Nd}_{1.2}\text{Mn}_{1.0}\text{Zn}_{3.0}\text{As}_4$ , and  $\text{Er}_{0.5}\text{Mn}_{0.4}\text{Zn}_{1.6}\text{As}_2$ . The components marked A–C are discussed in the text.

The formal assignments of  $\text{Zn}^{2+}$  and  $\text{As}^{3-}$  are hardly disputable, but it is unclear if  $\text{Mn}^{2+}$  is exclusively present in all cases. The Mn 2p spectra for  $\text{YbMn}_{0.3}\text{Zn}_{1.7}\text{As}_2$ ,  $\text{Er}_{0.5}\text{Mn}_{0.4}\text{Zn}_{1.6}\text{As}_2$ , and  $\text{Nd}_{1.2}\text{Mn}_{1.0}\text{Zn}_{3.0}\text{As}_4$  confirm that  $\text{Mn}^{2+}$  is indeed the dominant species present (**Figure 2.8b**). The spectra can be resolved into three component peaks (A–C), consistent with other  $\text{Mn}^{2+}$ -containing compounds.<sup>64,65</sup> Peak A, the main Mn  $2p_{3/2}$  core line peak, occurs at 640.1 eV for  $\text{YbMn}_{0.3}\text{Zn}_{1.7}\text{As}_2$ , 641.0 eV for  $\text{Nd}_{1.2}\text{Mn}_{1.0}\text{Zn}_{3.0}\text{As}_4$ , and 640.9 eV for  $\text{Er}_{0.5}\text{Mn}_{0.4}\text{Zn}_{1.6}\text{As}_2$ . These binding energies (BE) are higher than in elemental Mn (639.7(8) eV), within the ranges exhibited by various  $\text{Mn}^{2+}$ -containing compounds (MnS, 640.5–642.1 eV; MnO, 641.2(5) eV; (Ga,Mn)As, 641.0 eV), and lower than in  $\text{Mn}^{3+}$ -containing compounds ( $\text{Mn}_2\text{O}_3$ , 641.6(2) eV).<sup>66–72</sup> The BE of 640.1 eV in  $\text{YbMn}_{0.3}\text{Zn}_{1.7}\text{As}_2$  is noticeably shifted relative to the others (as

seen in the spectrum, offset vertically for clarity, in **Figure 2.8b**), but we attribute this observation to a slight reduction caused by Ar<sup>+</sup> sputtering procedure, which had to be performed for a longer time to improve the poor signal quality in this sample containing low Mn concentrations. Peak B is located to slighter lower BE from the core-line peak; this shoulder results from the Ar<sup>+</sup> sputtering procedure and is commonly found in Mn<sup>2+</sup> systems.<sup>64,65</sup> Peak C is an important diagnostic feature: it is a metal-to-ligand shake-up satellite peak that occurs only for Mn<sup>2+</sup> and is absent for Mn<sup>3+</sup> and Mn<sup>4+</sup>.<sup>72-76</sup> It is found at 645.8 eV for Nd<sub>1.2</sub>Mn<sub>1.0</sub>Zn<sub>3.0</sub>As<sub>4</sub> and 645.2 eV for Er<sub>0.5</sub>Mn<sub>0.4</sub>Zn<sub>1.6</sub>As<sub>2</sub>, but is difficult to locate for YbMn<sub>0.3</sub>Zn<sub>1.7</sub>As<sub>2</sub> probably because it is buried beneath the large background caused by the increased sputtering time. The XPS results do strongly imply that Mn<sup>2+</sup> is present in these compounds.

## 2.4 Conclusions

Many subtle factors are at play in the partial substitution of Mn for Zn in these rare-earth zinc arsenides with the CaAl<sub>2</sub>Si<sub>2</sub>-type structure. In the simplest case involving the divalent *RE* components, the compounds *RE*Mn<sub>0.4</sub>Zn<sub>1.6</sub>As<sub>2</sub> (*RE* = Eu, Yb) keep the parent structure; the Mn and Zn atoms disorder within the same tetrahedral site, and the distinction between rib and handle bonds in this site is controlled by the Zn atoms. In the more complex cases involving the trivalent *RE* components, the vacancies introduced into the hexagonal nets permit Mn atoms to occupy alternative tetrahedral sites close to the original Zn sites. For *RE*<sub>0.5</sub>Mn<sub>0.4</sub>Zn<sub>1.6</sub>As<sub>2</sub> (*RE* = Gd–Tm, Lu), considerable disorder ensues from the occurrence of *RE* vacancies, probably in the form of stacking faults of the hexagonal *RE* nets, as well as from the split Mn/Zn sites. For *RE*<sub>1.3</sub>Mn<sub>0.9</sub>Zn<sub>3.1</sub>As<sub>4</sub> (*RE* = La–Nd, Sm, Gd), the disorder is partially resolved through the segregation of

completely filled *RE* nets and 33% occupied *RE* nets. The distinction between these two series, for the early versus late trivalent *RE* members, supports the proposal that the A-cation in  $AB_2X_2$  phases with the  $CaAl_2Si_2$ -type structure does participate in bonding with the  $[B_2X_2]$  slabs and can thus indirectly influence electronic properties. Given the relatively high concentration of Mn in these quaternary arsenides, the electronic structure is dominated by a partially filled Mn-based d-band near the Fermi level, as shown for “ $La_{1.33}MnZn_3As_4$ ”, so that metallic behavior is predicted. We believe that Mn can likely be introduced at lower concentrations while a band gap is retained, so that the resulting compounds may be good candidates as magnetic semiconductors. Attempts to prepare Gd-containing solid solutions suggest that the Mn concentration can indeed be varied, but further efforts are required to optimize phase purity before magnetic measurements can be performed.

## References

1. Hoffmann, R.; Zheng, C. *J. Phys. Chem.* **1985**, *89*, 4175-4181.
2. Zheng, C.; Hoffmann, R. *J. Solid State Chem.* **1988**, *72*, 58-71.
3. Johrendt, D.; Felser, C.; Jepsen, O.; Andersen, O. K.; Mewis, A.; Rouxel, J. *J. Solid State Chem.* **1997**, *130*, 254-265.
4. Rotter, M.; Pangerl, M.; Tegel, M.; Johrendt, D. *Angew. Chem. Int. Ed.* **2008**, *47*, 7949-7952.
5. Johrendt, D.; Pöttgen, R. *Physica C* **2009**, *469*, 332-339.
6. Mandrus, D.; Sefat, A. S.; McGuire, M. A.; Sales, B. C. *Chem. Mater.* **2010**, *22*, 715-723.
7. Paglione, J.; Greene, R. L. *Nat. Phys.* **2010**, *6*, 645-658.
8. Klüfers, P.; Mewis, A. *Z. Kristallogr.* **1984**, *169*, 135-147.
9. Zheng, C.; Hoffmann, R.; Nesper, R.; von Schnering, H.-G. *J. Am. Chem. Soc.* **1986**, *108*, 1876-1884.
10. Burdett, J. K.; Miller, G. J. *Chem. Mater.* **1990**, *2*, 12-26.
11. Kranenberg, C.; Johrendt, D.; Mewis, A. *Z. Anorg. Allg. Chem.* **1999**, *625*, 1787-1793.
12. Kranenberg, C.; Johrendt, D.; Mewis, A. *Solid State Sci.* **2002**, *4*, 261-265.
13. Wartenberg, F.; Kranenberg, C.; Pocha, R.; Johrendt, D.; Mewis, A.; Hoffmann, R.-D.; Mosel, B. D.; Pöttgen, R. *Z. Naturforsch. B: J. Chem. Sci.* **2002**, *57*, 1270-1276.
14. Alemany, P.; Llunell, M.; Canadell, E. *J. Comput. Chem.* **2008**, *29*, 2144-2153.
15. Kauzlarich, S. M.; Brown, S. R.; Snyder, G. J. *Dalton Trans.* **2007**, 2099-2107.
16. Toberer, E. S.; May, A. F.; Snyder, G. J. *Chem. Mater.* **2010**, *22*, 624-634.

17. Zhang, H.; Zhao, J.-T.; Grin, Yu.; Wang, X.-J.; Tang, M.-B.; Man, Z.-Y.; Chen, H.-H.; Yang, X.-X. *J. Chem. Phys.* **2008**, *129*, 164713-1-164713-5.
18. Zhang, H.; Fang, L.; Tang, M.-B.; Chen, H.-H.; Yang, X.-X.; Guo, X.; Zhao, J.-T.; Grin, Yu. *Intermetallics* **2010**, *18*, 193-198.
19. Flage-Larsen, E.; Diplas, S.; Prytz, Ø.; Toberer, E. S.; May, A. F. *Phys. Rev. B* **2010**, *81*, 205204-1-205204-7.
20. May, A. F.; McGuire, M. A.; Singh, D. J.; Ma, J.; Delaire, O.; Huq, A.; Cai, W.; Wang, H. *Phys. Rev. B* **2012**, *85*, 035202-1-035202-10.
21. Pomrehn, G. S.; Zevalkink, A.; Zeier, W. G.; van de Walle, A.; Snyder, G. J. *Angew. Chem. Int. Ed.* **2014**, *53*, 3422-3426.
22. Gascoin, F.; Ottensmann, S.; Stark, D.; Haïle, S. M.; Snyder, G. J. *Adv. Funct. Mater.* **2005**, *15*, 1860-1864.
23. Villars, P.; Cenzual, K. *Pearson's Crystal Data – Crystal Structure Database for Inorganic Compounds, release 2010/11*; ASM International: Materials Park, OH, 2010.
24. Nientiedt, A. T.; Lincke, H.; Rodewald, U. Ch.; Pöttgen, R.; Jeitschko, W. *Z. Naturforsch. B: J. Chem. Sci.* **2011**, *66*, 221-226.
25. Klüfers, P.; Mewis, A.; Schuster, H.-U. *Z. Kristallogr.* **1979**, *149*, 211-225.
26. Mewis, A. *Z. Naturforsch. B: Anorg. Chem., Org. Chem.* **1980**, *35*, 939-941.
27. Klüfers, P.; Neumann, H.; Mewis, A.; Schuster, H.-U. *Z. Naturforsch. B: Anorg. Chem., Org. Chem.* **1980**, *35*, 1317-1318.
28. Zwiener, G.; Neumann, H.; Schuster, H.-U. *Z. Naturforsch. B: Anorg. Chem., Org. Chem.* **1981**, *36*, 1195-1197.

29. Mahan, A.; Mewis, A. Z. *Naturforsch. B: Anorg. Chem., Org. Chem.* **1983**, *38*, 1041-1045.
30. Tejedor, P.; Stacy, A. M. *J. Solid State Chem.* **1990**, *89*, 227-236.
31. Blanchard, P. E. R.; Stoyko, S. S.; Cavell, R. G.; Mar, A. *J. Solid State Chem.* **2011**, *184*, 97-103.
32. Nateprov, A. N.; Kravtsov, V. Ch.; Moshnyaga, V.; Schorr, S. *Elektron. Obrab. Mater.* **2012**, *48*, 94-98.
33. Stoyko, S. S.; Ramachandran, K. K.; Blanchard, P. E. R.; Rosmus, K. A.; Aitken, J. A.; Mar, A. *J. Solid State Chem.* **2014**, *213*, 275-286.
34. Ponnambalam, V.; Lindsey, S.; Xie, W.; Thompson, D.; Drymiotis, F.; Tritt, T. M. *J. Phys. D: Appl. Phys.* **2011**, *44*, 155406-1-155406-6.
35. Ponnambalam, V.; Morelli, D. T. *J. Electron. Mater.* **2014**, *43*, 1875-1880.
36. Yu, C.; Zhu, T. J.; Zhang, S. N.; Zhao, X. B.; He, J.; Su, Z.; Tritt, T. M. *J. Appl. Phys.* **2008**, *104*, 013705-1-013705-5.
37. Wang, X.-J.; Tang, M.-B.; Chen, H.-H.; Yang, X.-X.; Zhao, J.-T.; Burkhardt, U.; Grin, Yu. *Appl. Phys. Lett.* **2009**, *94*, 092106-1-092106-3.
38. Zhang, H.; Baitinger, M.; Tang, M.-B.; Man, Z.-Y.; Chen, H.-H.; Yang, X.-X.; Liu, Y.; Chen, L.; Grin, Yu.; Zhao, J.-T. *Dalton Trans.* **2010**, *39*, 1101-1104.
39. Cao, Q.-G.; Zhang, H.; Tang, M.-B.; Chen, H.-H.; Yang, X.-X.; Grin, Yu.; Zhao, J.-T. *J. Appl. Phys.* **2010**, *107*, 053714-1-053714-5.
40. Zhang, H.; Fang, L.; Tang, M.-B.; Man, Z.-Y.; Chen, H.-H.; Yang, X.-X.; Baitinger, M.; Grin, Yu.; Zhao, J.-T. *J. Chem. Phys.* **2010**, *133*, 194701-1-194701-5.

41. Guo, K.; Cao, Q.-G.; Feng, X.-J.; Tang, M.-B.; Chen, H.-H.; Guo, X.; Chen, L.; Grin, Yu.; Zhao, J.-T. *Eur. J. Inorg. Chem.* **2011**, 4043-4048.
42. Zhao, L.-D.; Lo, S.-H.; Zhang, Y.; Sun, H.; Tan, G.; Uher, C.; Wolverton, C.; Dravid, V. P.; Kanatzidis, M. G. *Nature* **2014**, *508*, 373-377.
43. Deng, Z.; Jin, C. Q.; Liu, Q. Q.; Wang, X. C.; Zhu, J. L.; Feng, S. M.; Chen, L. C.; Yu, R. C.; Arguello, C.; Goko, T.; Ning, F.; Zhang, J.; Wang, Y.; Aczel, A. A.; Munsie, T.; Williams, T. J.; Luke, G. M.; Kakeshita, T.; Uchida, S.; Higemoto, W.; Ito, T. U.; Gu, B.; Maekawa, S.; Morris, G. D.; Uemura, Y. J. *Nat. Commun.* **2011**, *2*, 422-1-422-5.
44. Deng, Z.; Zhao, K.; Gu, B.; Han, W.; Zhu, J. L.; Wang, X. C.; Li, X.; Liu, Q. Q.; Yu, R. C.; Goko, T.; Frandsen, B.; Liu, L.; Zhang, J.; Wang, Y.; Ning, F. L.; Maekawa, S.; Uemura, Y. J.; Jin, C. Q. *Phys. Rev. B* **2013**, *88*, 081203-1-081203-5.
45. Altshuler, T. S.; Goryunov, Yu. V.; Nateprov, A. V. *J. Phys.: Conf. Ser.* **2011**, *324*, 012020-1-012020-5.
46. Goryunov, Yu.; Fritsch, V.; von Löhneysen, H.; Nateprov, A. *J. Phys.: Conf. Ser.* **2012**, *391*, 012015-1-012015-4.
47. Goryunov, Yu. V.; Levchenko, A. V.; Nateprov, A. N. *J. Phys.: Conf. Ser.* **2012**, *400*, 032013-1-032013-4.
48. Nateprov, A.; Cisowski, J.; Heimann, J.; Mirebeau, I. *J. Alloys Compd.* **1999**, *290*, 6-9.
49. Lin, X.; Stoyko, S. S.; Mar, A. *J. Solid State Chem.* **2013**, *199*, 189-195.
50. Stoyko, S. S.; Mar, A. *J. Solid State Chem.* **2011**, *184*, 2360-2367.
51. Stoyko, S. S.; Mar, A. *Inorg. Chem.* **2011**, *50*, 11152-11161.
52. Lin, X.; Mar, A. *Inorg. Chem.* **2013**, *52*, 7261-7270.

53. Stoyko, S. S.; Khatun, M.; Mar, A. *Inorg. Chem.* **2012**, *51*, 2621-2628.
54. Saparov, B.; Bobev, S. *Acta Crystallogr., Sect. E* **2010**, *66*, i24.
55. Sheldrick, G. M. *SHELXTL*, version 6.12; Bruker AXS Inc.: Madison, WI, 2001.
56. Gladyshevskii, E. I.; Kripyakevich, P. I.; Bodak, O. I. *Ukr. Fiz. Zh.* **1967**, *12*, 447-452.
57. Gelato, L. M.; Parthé, E. *J. Appl. Crystallogr.* **1987**, *20*, 139-143.
58. Tank, R.; Jepsen, O.; Burkhardt, A.; Andersen, O. K. *TB-LMTO-ASA Program*, version 4.7; Max Planck Institut für Festkörperforschung: Stuttgart, Germany, 1998.
59. Fairley, N. *CasaXPS*, version 2.3.9; Casa Software Ltd.: Teighnmouth, Devon, UK, 2003, <http://www.casaxps.com>.
60. Rühl, R.; Jeitschko, W. *Mater. Res. Bull.* **1979**, *14*, 513-517.
61. Guymont, M.; Tomas, A.; Julien-Pouzol, M.; Jaulmes, S.; Guittard, M. *Phys. Status Solidi A* **1990**, *121*, 21-28.
62. Onoda, M.; Chen, X.; Sato, A.; Wada, H. *J. Solid State Chem.* **2000**, *152*, 332-339.
63. Suga, S.; Ogawa, S.; Namatame, H.; Taniguchi, M.; Kakizaki, A.; Ishii, T.; Fujimori, A.; Oh, S.-J.; Kato, H.; Miyahara, T.; Ochiai, A.; Suzuki, T.; Kasuya, T. *J. Phys. Soc. Jpn.* **1989**, *58*, 4534-4543.
64. Iwanowski, R. J.; Heinonen, M. H.; Janik, E. *Chem. Phys. Lett.* **2004**, *387*, 110-115.
65. Iwanowski, R. J.; Heinonen, M. H.; Janik, E. *Appl. Surf. Sci.* **2005**, *249*, 222-230.
66. Wagner, C. D.; Naumkin, A. V.; Kraut-Vass, A.; Allison, J. W.; Powell, C. J.; Rumble, J. R., Jr. *NIST X-ray Photoelectron Spectroscopy Database*, version 3.5 (web version); National Institute of Standards and Technology: Gaithersburg, MD, 2003, <http://srdata.nist.gov/xps>.

67. Carver, J. C.; Schweitzer, G. K.; Carlson, T. A. *J. Chem. Phys.* **1972**, *57*, 973-982.
68. Aoki, A. *Jpn. J. Appl. Phys.* **1976**, *15*, 305-311.
69. Franzen, H. F.; Umaña, M. X.; McCreary, J. R.; Thorn, R. J. *J. Solid State Chem.* **1976**, *18*, 363-368.
70. Franzen, H. F.; Sterner, C. *J. Solid State Chem.* **1978**, *25*, 227-230.
71. Di Castro, V.; Polzonetti, G. *J. Electron Spectrosc. Relat. Phenom.* **1989**, *48*, 117-123.
72. Eid, K. F.; Stone, M. B.; Maksimov, O.; Shih, T. C.; Ku, K. C.; Fadgen, W.; Palstrøm, C. J.; Schiffer, P.; Samarth, N. *J. Appl. Phys.* **2005**, *97*, 10D304-1-10D304-6.
73. Brisk, M. A.; Baker, A. D. *J. Electron Spectrosc. Relat. Phenom.* **1975**, *7*, 197-213.
74. Jeng, S.-P.; Lad, R. J.; Heinrich, V. E. *Phys. Rev. B* **1991**, *43*, 11971-11977.
75. Stranick, M. A. *Surf. Sci. Spectra* **1999**, *6*, 31-38.
76. Stranick, M. A. *Surf. Sci. Spectra* **1999**, *6*, 39-46.

## Chapter 3

### Rare-earth manganese arsenides $RE_4Mn_2As_5$ ( $RE = La\text{--}Pr$ )

*A version of this chapter has been published. Tabassum, D.; Lin, X.; Mar, A. J. Alloys Comp. 2015, 636, 187–190*

#### 3.1 Introduction

Given the current interest in ternary arsenides, driven by the discovery of superconductivity in  $BaFe_2As_2$  and related compounds,<sup>1,2</sup> it is important to examine the formation of phases within ternary arsenide systems in general. Among ternary rare-earth transition-metal arsenides  $RE\text{--}M\text{--}As$ , there are over 200 phases known when  $M$  is a late transition-metal (groups 8–12) but only a handful when  $M$  is an early one (groups 3–7),<sup>3</sup> being restricted to representatives containing Nb and Mn in combination with a divalent  $RE$  metal:  $Eu_{13}NbAs_{11}$  (defect  $Ca_{14}AlSb_{11}$ -type),<sup>4</sup>  $Eu_{14}MnAs_{11}$  ( $Ca_{14}AlSb_{11}$ -type),<sup>5,6</sup> and  $REMn_2As_2$  ( $RE = Eu, Yb; CaAl_2Si_2$ -type).<sup>7</sup> These four compounds may be considered to be Zintl phases containing metals with  $d^0$  ( $Nb^{5+}$ ) and  $d^5$  ( $Mn^{2+}$ ) configurations; some isotopic counterparts such as  $REZn_2As_2$  are found containing metals with  $d^{10}$  ( $Zn^{2+}$ ) configurations.<sup>8</sup> In fact, partial substitution of Mn for Zn is commonly used as a strategy to introduce magnetic properties, as has been exploited to develop dilute ferromagnetic semiconductors, for instance.<sup>9,10</sup> Recently, two Mn-substituted series,  $RE_{1-y}Mn_xZn_{2-x}As_2$  ( $RE = Eu\text{--}Lu$ ) and  $RE_{2-y}Mn_xZn_{4-x}As_4$  ( $RE = La\text{--}Nd, Sm, Gd$ ), have been shown to adopt structures derived from an idealized  $REZn_2As_2$  model ( $CaAl_2Si_2$ -type), but with subtle differences originating from partial ordering of Mn and Zn atoms.<sup>11</sup>  $REZn_2As_2$  is just the first member ( $n = 0$ ) of a more extensive homologous

series with formula  $REZn_{2-x}As_{2\cdot n}(REAs)$  ( $RE = La-Nd, Sm; n = 3, 4, 5, 6$ ) in which the parent  $CaAl_2Si_2$ -type structure is intergrown with increasingly thicker rocksalt-type slabs [ $REAs$ ] and the Zn atoms are deficient.<sup>12</sup> The characterization of two quaternary compounds,  $Ce_4Mn_{0.6}Zn_{1.2}As_5$  ( $n = 3$ ) and  $Ce_6Mn_{0.4}Zn_{1.3}As_7$  ( $n = 5$ ),<sup>12</sup> suggested that Mn can also be substituted into these series. Is it possible to elucidate an analogous all-Mn-containing homologous series  $REMn_{2-x}As_{2\cdot n}(REAs)$ ?

Here we describe the preparation and structural characterization of  $RE_4Mn_2As_5$  ( $RE = La-Pr$ ), corresponding to the  $n = 3$  member of a putative homologous series  $REMn_2As_{2\cdot n}(REAs)$ . Unlike the Zn-containing series, there appears to be no evidence for Mn deficiencies. The implications of Mn substitution to the electronic band structure are examined.

## 3.2 Experimental

### 3.2.1 Synthesis

The title compounds were originally detected in reactions with the loading composition “ $REMnGa_3As_4$ ” ( $RE = La-Pr$ ), with the added Ga intended to act as a flux to promote crystal growth. Starting materials were freshly filed  $RE$  pieces (99.9%, Hefa), Mn powder (99.99%, Aldrich), Ga shot (99.99%, Alfa-Aesar), and As lumps (99.999%, Alfa-Aesar). These elements were combined on a 0.3-g scale, cold-pressed into pellets, and loaded into fused-silica tubes, which were evacuated and sealed. The tubes were heated at 800 °C for 2 d, heated to 1050 °C for 50 h, held at this temperature for 4 d, cooled to 500 °C over 7 d, and then cooled to room temperature over 2 d. Crystals obtained from these reactions were examined on a JEOL JSM-6010LA scanning electron microscope. Energy-dispersive X-ray (EDX) analysis revealed that these crystals are

ternary phases free of Ga. From examination of multiple points (> 20) on each crystal, the average chemical compositions (36(2)% La, 19(2)% Mn, 45(2)% As; 36(1)% Ce, 22(1)% Mn, 42(1)% As; 40(1)% Pr, 17(1)% Mn, 43(1)% As) were in good agreement with the formula  $RE_4Mn_2As_5$  (36% RE, 18% Mn, 45% As). Although the errors in these compositions are sample dependent, they typically do not exceed ~5% and are usually more precise, through comparison with known phases such as binary arsenides. Powder X-ray diffraction (XRD) patterns were collected on an Inel powder diffractometer equipped with a curved position-sensitive detector (CPS 120) and a Cu  $K\alpha_1$  radiation source. In general, the products contain mixtures of ternary (RE–Mn–As) and various binary phases. Cell parameters for  $RE_4Mn_2As_5$  refined from these patterns are listed in

**Table 3.1.**

**Table 3.1** Cell parameters for  $RE_4Mn_2As_5$  ( $RE = La\text{--}Pr$ )<sup>a</sup>

Compound	$a$ (Å)	$c$ (Å)	$V$ (Å <sup>3</sup> )
La <sub>4</sub> Mn <sub>2</sub> As <sub>5</sub>	4.321(3)	17.757(8)	287.1(2)
Ce <sub>4</sub> Mn <sub>2</sub> As <sub>5</sub>	4.266(1)	17.507(6)	275.9(1)
Pr <sub>4</sub> Mn <sub>2</sub> As <sub>5</sub>	4.246(2)	17.403(9)	271.7(2)

<sup>a</sup>Refined from powder XRD data.

Subsequently, stoichiometric reactions on a 0.3-g scale with the loading composition  $RE_4Mn_2As_5$  ( $RE = La\text{--}Nd, Sm$ ) were carried out in the absence of Ga. The reactants were initially heated at 500 °C for 2 d (this low-temperature treatment was applied to minimize loss of volatile As), heated to 750 °C for 20 h, held at this temperature for 7 d, and then cooled to room temperature for 10 h. To improve homogeneity, the products were reground, pressed into pellets, and subjected to a second heating treatment at 750 °C for 10 d. Powder XRD patterns indicated that these reactions resulted in formation of  $RE_4Mn_2As_5$  only for  $RE = Pr$ . Other members of the hypothetical homologous series  $RE_nMn_2As_{2\cdot n}(REAs)$ , likely  $RE_6Mn_2As_7$  ( $n = 5$ ), appear to

be formed for the other *RE* components (La, Ce, Nd, Sm); however, because the powder XRD patterns of different members of this series would be very similar, full confirmation requires detailed structure determination from single crystals, which were not obtained from these reactions. Other synthetic conditions such as higher temperatures (1050 °C, without Ga) and addition of I<sub>2</sub> as a vapour transport agent were attempted, but these led to decomposition into binary phases. Further investigations are ongoing to optimize the synthetic conditions for *RE*<sub>4</sub>Mn<sub>2</sub>As<sub>5</sub> for different *RE* components.

### 3.2.2 Structure determination

Suitable crystals were available for La<sub>4</sub>Mn<sub>2</sub>As<sub>5</sub> and Pr<sub>4</sub>Mn<sub>2</sub>As<sub>5</sub>. Intensity data were collected at room temperature on a Bruker PLATFORM diffractometer equipped with a SMART APEX II CCD area detector and a graphite-monochromated Mo *K*α radiation source, using  $\omega$  scans in 5–8 batches at different  $\phi$  angles with a frame width of 0.3° and an exposure time of 15 s per frame. Face-indexed absorption corrections were applied. Structure solution and refinement were carried out with use of the SHELXTL (version 6.12) program package.<sup>13</sup> The centrosymmetric trigonal space group  $P\bar{3}m1$  was chosen. Direct methods confirmed a structural model analogous to the previously known Zn-containing phases *RE*<sub>4</sub>Zn<sub>2–*x*</sub>As<sub>5</sub>. The atomic positions were standardized with the program STRUCTURE TIDY.<sup>14</sup> Refinements generally proceeded in a straightforward fashion, with the main complication being the possibility of partial occupancy of the Mn site at *2d* (1/3, 2/3, 0.55). When refined, the occupancy of this Mn site converges to 1.03(2) for the La-member and 0.97(1) for the Pr-member, with reasonable displacement parameters. The agreement factors from these on models with unconstrained Mn occupancies remain unchanged at R1= 0.043 (La-member) and 0.026 (Pr-member)

relative to the fully stoichiometry models, and they did not depend on the order of refining the occupancy or displacement parameters. Because these results Mn deficiency are either nonexistence or at best, not significant, we assumed a strictly stoichiometric formula  $RE_4Mn_2As_5$  in the final refinements.

The final difference electron density map for  $La_4Mn_2As_5$  contained a small peak ( $\sim 8 \text{ e}/\text{\AA}^3$ ) that is 0.8  $\text{\AA}$  away from Mn atom and located at chemically unmeaningful distances (1.8  $\text{\AA}$  and 2.9  $\text{\AA}$ ) to surrounding As atoms. Modeling this peak as a partially occupied Mn atom did not lead to convergence. We attribute the somewhat worse agreement factors in the structure determination of  $La_4Mn_2As_5$  to weakly diffracting quality of the crystal ( $\langle I/\sigma \rangle = 20$ ).

Crystal data and experimental details are summarized in **Table 3.2**, positional and displacement parameters are listed in **Table 3.3**, and selected interatomic distances are listed in **Table 3.4**. Further data, in CIF format, have been sent to Fachinformationszentrum Karlsruhe, Abt. PROKA, 76344 Eggenstein-Leopoldshafen, Germany, as supplementary material No. CSD-429102 and 429103, and can be obtained by contacting FIZ (quoting the article details and the corresponding CSD numbers).

**Table 3.2** Crystallographic data for  $RE_4Mn_2As_5$  ( $RE = La, Pr$ ).

Formula	La <sub>4</sub> Mn <sub>2</sub> As <sub>5</sub>	Pr <sub>4</sub> Mn <sub>2</sub> As <sub>5</sub>
Formula mass (amu)	1040.12	1048.12
Space group	$P\bar{3}m1$ (No. 164)	$P\bar{3}m1$ (No. 164)
$a$ (Å)	4.3275(14)	4.2526(12)
$c$ (Å)	17.792(6)	17.427(5)
$V$ (Å <sup>3</sup> )	288.6(2)	272.9(2)
$Z$	1	1
$\rho_{\text{calcd}}$ (g cm <sup>-3</sup> )	5.986	6.377
Crystal dimensions (mm)	0.04 × 0.04 × 0.03	0.10 × 0.04 × 0.04
Radiation	graphite monochromated Mo $K\alpha$ , $\lambda = 0.71073$ Å	
$\mu$ (Mo $K\alpha$ ) (mm <sup>-1</sup> )	30.75	34.71
Transmission factors	0.404–0.508	0.156–0.403
$2\theta$ limits	4.58–66.21°	4.67–66.31°
Data collected	$-6 \leq h \leq 6,$ $-6 \leq k \leq 6,$ $-26 \leq l \leq 27$	$-6 \leq h \leq 6,$ $-6 \leq k \leq 6,$ $-26 \leq l \leq 26$
No. of data collected	4010	4005
No. of unique data, including $F_o^2 < 0$	500 ( $R_{\text{int}} = 0.143$ )	481 ( $R_{\text{int}} = 0.020$ )
No. of unique data, with $F_o^2 > 2\sigma(F_o^2)$	277	404
No. of variables	18	18
$R(F)$ for $F_o^2 > 2\sigma(F_o^2)$ <sup>a</sup>	0.043	0.026
$R_w(F_o^2)$ <sup>b</sup>	0.117	0.058
Goodness of fit	0.95	1.31
$(\Delta\rho)_{\text{max}}, (\Delta\rho)_{\text{min}}$ (e Å <sup>-3</sup> )	7.88, -3.90	3.76, -2.62

$$^a R(F) = \frac{\sum ||F_o| - |F_c||}{\sum |F_o|}$$

$$^b R_w(F_o^2) = \frac{[\sum [w(F_o^2 - F_c^2)^2] / \sum w F_o^4]^{1/2}}{w^{-1} = [\sigma^2(F_o^2) + (Ap)^2 + Bp]},$$

where  $p = [\max(F_o^2, 0) + 2F_c^2] / 3$ .

**Table 3.3** Atomic coordinates and equivalent isotropic displacement parameters for  $RE_4Mn_2As_5$  ( $RE = La, Pr$ ).

Atom	Wyckoff position	$x$	$y$	$z$	$U_{eq}$ ( $\text{\AA}^2$ ) <sup>a</sup>
<b>La<sub>4</sub>Mn<sub>2</sub>As<sub>5</sub></b>					
La1	2 <i>d</i>	1/3	2/3	0.09916(7)	0.0096(3)
La2	2 <i>c</i>	0	0	0.29720(8)	0.0125(3)
Mn	2 <i>d</i>	1/3	2/3	0.5495(2)	0.0186(8)
As1	2 <i>d</i>	1/3	2/3	0.40509(13)	0.0118(5)
As2	2 <i>d</i>	1/3	2/3	0.79834(12)	0.0084(5)
As3	1 <i>a</i>	0	0	0	0.0094(6)
<b>Pr<sub>4</sub>Mn<sub>2</sub>As<sub>5</sub></b>					
Pr1	2 <i>d</i>	1/3	2/3	0.09864(3)	0.0068(1)
Pr2	2 <i>c</i>	0	0	0.29548(3)	0.0090(1)
Mn	2 <i>d</i>	1/3	2/3	0.54997(9)	0.0134(3)
As1	2 <i>d</i>	1/3	2/3	0.40244(5)	0.0087(2)
As2	2 <i>d</i>	1/3	2/3	0.79952(5)	0.0071(2)
As3	1 <i>a</i>	0	0	0	0.0073(2)

<sup>a</sup>  $U_{eq}$  is defined as one-third of the trace of the orthogonalized  $U_{ij}$  tensor.

**Table 3.4** Interatomic distances ( $\text{\AA}$ ) for  $RE_4Mn_2As_5$  ( $RE = La, Pr$ ).

	<b>La<sub>4</sub>Mn<sub>2</sub>As<sub>5</sub></b>	<b>Pr<sub>4</sub>Mn<sub>2</sub>As<sub>5</sub></b>
$RE1-As3$ ( $\times 3$ )	3.059(1)	2.997(1)
$RE1-As2$ ( $\times 3$ )	3.093(2)	3.029(1)
$RE2-As2$ ( $\times 3$ )	3.022(2)	2.961(1)
$RE2-As1$ ( $\times 3$ )	3.151(2)	3.083(1)
Mn-As1	2.569(4)	2.571(2)
Mn-As1 ( $\times 3$ )	2.626(2)	2.592(1)
Mn-Mn ( $\times 3$ )	3.056(5)	3.010(2)

### 3.2.3 Band structure calculations

Tight-binding linear muffin tin orbital (TB-LMTO) band structure calculations were performed on  $\text{La}_4\text{Mn}_2\text{As}_5$  within the local density and atomic spheres approximation with use of the Stuttgart TB-LMTO program.<sup>15</sup> The basis set consisted of La 6s/6p/5d/4f, Mn 4s/4p/3d, and As 4s/4p/4d orbitals, with the La 6p and As 4d orbitals being downfolded. Integrations in reciprocal space were carried out with an improved tetrahedron method over 202 irreducible  $k$  points within the first Brillouin zone.

### 3.3 Results and discussion

Prior to this work, the only known ternary  $RE$ -Mn-As phases were those containing divalent  $RE$  metals:  $\text{Eu}_{14}\text{MnAs}_{11}$ ,  $\text{EuMn}_2\text{As}_2$ , and  $\text{YbMn}_2\text{As}_2$ .<sup>5-7</sup> We initially attempted to synthesize defect  $RE_{0.67}\text{Mn}_2\text{As}_2$  containing trivalent  $RE$  metals, in analogy to  $RE_{0.67}\text{Zn}_2\text{As}_2$ ,<sup>16</sup> but did not succeed. The new compounds presented here,  $RE_4\text{Mn}_2\text{As}_5$  ( $RE = \text{La}-\text{Pr}$ ), containing trivalent  $RE$  metals, are isotypic to  $RE_4\text{Zn}_{2-x}\text{As}_5$  ( $RE = \text{La}-\text{Nd}, \text{Sm}$ )<sup>12</sup> and  $\text{Ce}_4\text{Zn}_{2-x}\text{P}_5$ <sup>17</sup> except that there is no evidence for a significant Mn deficiency. Single crystal X-ray diffraction studies on  $\text{La}_4\text{Mn}_2\text{As}_5$  and  $\text{Pr}_4\text{Mn}_2\text{As}_5$  confirmed that there was no improvement in agreement factors if the occupancy of Mn site was refined; by extension  $\text{Ce}_4\text{Mn}_2\text{As}_5$  is also assumed to attain ideal stoichiometry even though no suitable single crystals were available for structure determination. The trigonal structure (space group  $P\bar{3}m1$ ) of  $RE_4\text{Mn}_2\text{As}_5$  can be described by a stacking along the  $c$ -axis of four-layer-thick rocksalt-type  $[\text{REAs}]$  slabs, built up of edge-sharing  $\text{REAs}_6$  octahedra, alternating with  $[\text{Mn}_2\text{As}_2]$  slabs, built up of edge-sharing  $\text{MnAs}_6$  tetrahedra (**Figure 3.1**).

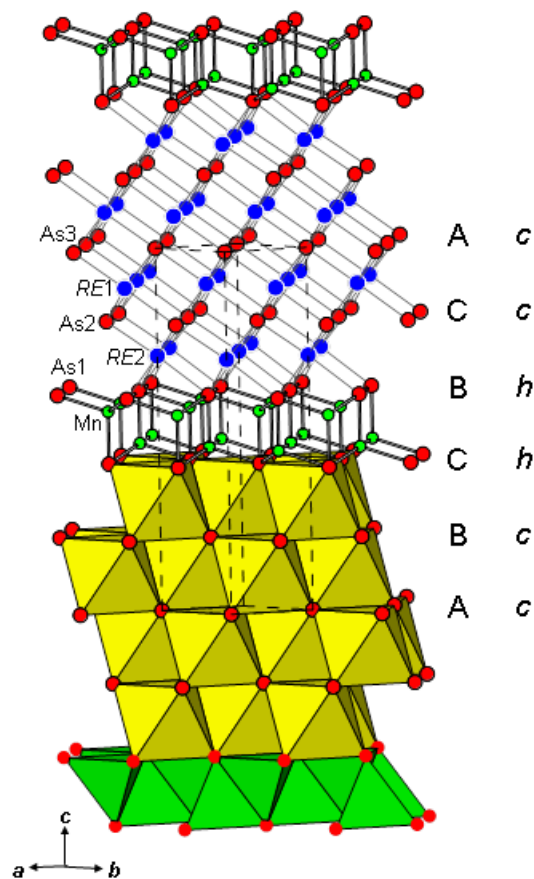


**Figure 3.1** Structure of  $RE_4Mn_2As_5$  ( $RE = La\text{--}Pr$ ) built up of slabs of  $RE$ -centred octahedra (yellow) and  $Mn$ -centred tetrahedra (green). The stacking sequence of  $As$  atoms in close-packed layers is noted.

The  $As$  atoms are arranged in close-packed nets in the stacking sequence ABCBC (or  $h^2c^3$  in Jagodzinski notation). Within four pairs of these nets, all octahedral sites are filled by  $RE$  atoms; within the fifth pair of nets, all tetrahedral sites are filled by  $Mn$  atoms. Because there are twice as many tetrahedral as octahedral sites in an arrangement of close-packed atoms, this means that the  $RE$  atoms fill 4/5 of the octahedral sites and the  $Mn$  atoms fill 1/5 of the tetrahedral sites within the overall structure.

Bond distances (**Table 3.4**) are consistent with expectations. The  $RE\text{--}As$  distances of 3.0–3.1 Å within the  $REAs_6$  octahedra are the same as in the binary rocksalt-

type arsenides  $REAs$ .<sup>18</sup> The Mn–As distances split into two inequivalent sets with the three ribs longer than the handle of the  $MnAs_4$  tetrahedra, similar to what is found in  $RE Mn_2As_2$  containing divalent  $RE$  (cf., 2.626 Å ribs and 2.569 Å handle in  $La_4Mn_2As_5$ ; 2.622 Å ribs and 2.601 Å handle in  $EuMn_2As_2$ ). There are no As–As contacts and the closest Mn–Mn contacts are just over 3.0 Å, too long to be bonding. These observations imply that  $RE^{3+}$ ,  $Mn^{2+}$ , and  $As^{3-}$  species are present, if an ionic model is assumed, which would lead to the formulation  $(RE^{3+})_4(Mn^{2+})_2(As^{3-})_5(e^-)$  containing an electron excess. A similar formulation was proposed for the  $RE_4Zn_{2-x}As_5$  except that the electron excess can be alleviated through Zn deficiencies.<sup>12</sup>

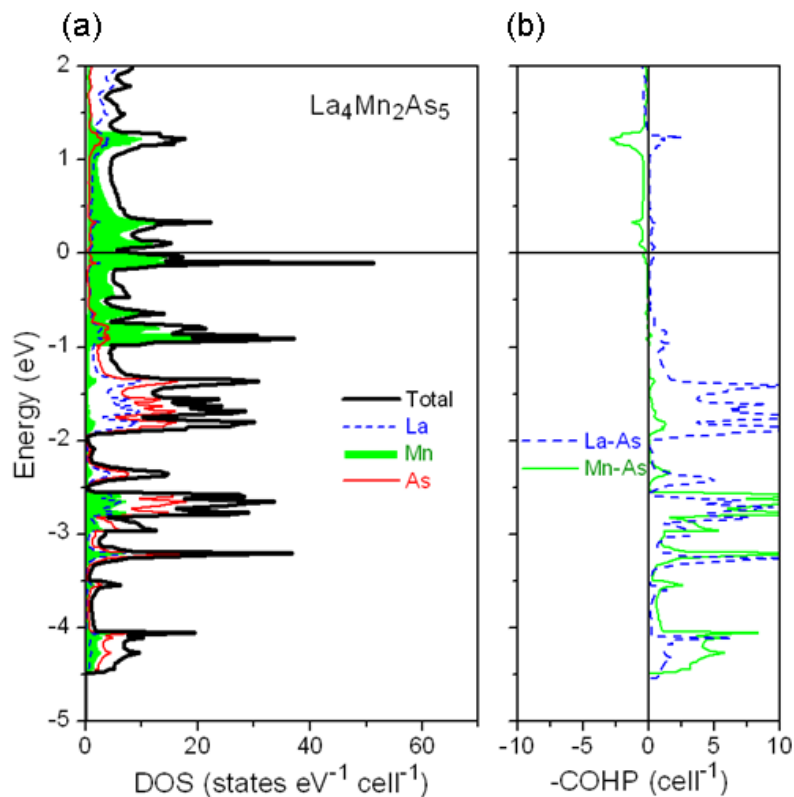


**Figure 3.2** (a) Density of states (DOS) and its atomic projections for  $La_4Mn_2As_5$ . (b) Crystal orbital Hamilton population ( $-COHP$ ) curves for La–As and Mn–As interactions.

However, the Zn content in the experimentally observed compositions,  $RE_4Zn_{1.7-1.8}As_5$ , is not as low as predicted by the charge-balanced formulation  $(RE^{3+})_4(Zn^{2+})_{1.5}(As^{3-})_5$ , which corresponds to lowering the Fermi level to a pseudogap in the electronic band structure. In contrast, because there is no pseudogap in the case of  $RE_4Mn_2As_5$ , as seen in the band structure for  $La_4Mn_2As_5$  (**Figure 3.2a**), a fully stoichiometric formula can be attained. The density of states (DOS) near the Fermi level is dominated by Mn 3d states, but these are essentially nonbonding, as confirmed by the crystal orbital Hamilton population (COHP) curve (**Figure 3.2b**). The most likely way that a gap might open in the DOS is through the occurrence of magnetic ordering. To test this possibility, a spin-polarized calculation on a ferromagnetic model was performed (**Figure 3.3**).

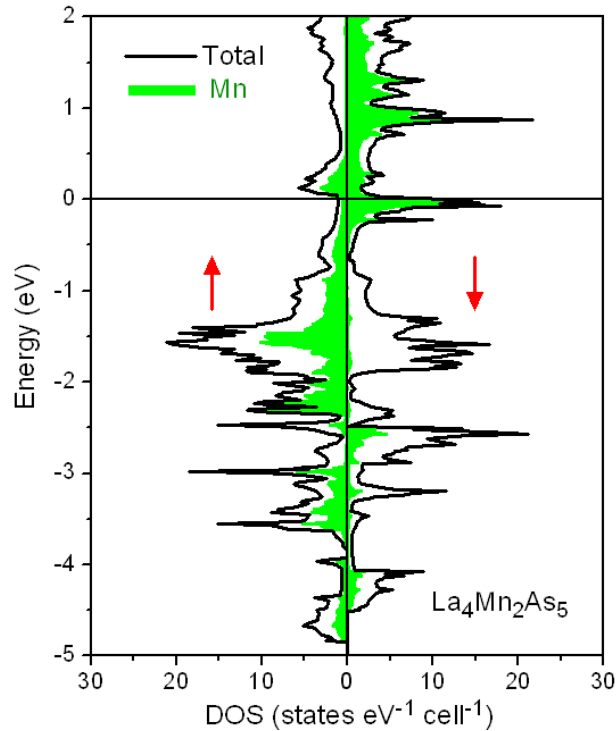


**Figure 3.3** DOS curve for spin-polarized  $La_4Mn_2As_5$  in a hypothetical ferromagnetic model, with contributions from Mn atoms shown by shaded region.

The magnetic model is more stable than the non-magnetic one by 1.4 eV/cell because the Mn 3d states become strongly split (by 2.5 eV), resulting in a magnetic moment of 3.2  $\mu_B$  per Mn atom. Nevertheless, no gap or pseudo gap forms in the DOS near or below the Fermilevel even after this spin-polarization. We have attempted to investigate the possibility of a homogeneity range in  $\text{Pr}_4\text{Mn}_{2-x}\text{As}_5$  by performing reactions with various loading compositions ( $x = 0-0.4$  in increments of 0.1). For  $x = 0-0.1$ , the ternary phase  $\text{Pr}_4\text{Mn}_{2-x}\text{As}_5$  was formed (65–70%) but with admixtures of other binary phases because the As content is difficult to control owing to its volatility; thus, the results are inconclusive. Mixing of Mn 3d and As 4p states gives rise to strong Mn–As bonding interactions found mostly between  $-4.5$  and  $-2.0$  eV, corresponding to an integrated COHP value (–ICOHP) of 2.1 eV/bond. Notwithstanding the ionic formulation above, the La–As interactions also have some covalent bonding character through mixing of states between  $-4.5$  and  $-0.5$  eV, with –ICOHP of 0.9 eV/bond.

The preparation of  $\text{RE}_4\text{Mn}_2\text{As}_5$ , together with the previous identification of  $\text{RE}_4\text{Zn}_{2-x}\text{As}_5$  and a few quaternary phases such as  $\text{Ce}_4\text{Mn}_{0.6}\text{Zn}_{1.2}\text{As}_5$ ,<sup>12</sup> suggests that complete mixing of Mn and Zn atoms may be possible over the entire range. However, we have recently shown that complex phenomena involving partial ordering and deficiencies of Mn and Zn atoms can take place in the parent  $\text{CaAl}_2\text{Si}_2$ -type series  $\text{RE}_{1-y}(\text{Mn,Zn})_{2-x}\text{As}_2$ .<sup>11</sup> Thus, a careful study of  $\text{RE}_4(\text{Mn,Zn})_{2-x}\text{As}_5$  is warranted.

### 3.4 Conclusions

$\text{RE}_4\text{Mn}_2\text{As}_5$  ( $\text{RE} = \text{La-Pr}$ ) are the first examples of  $n = 3$  members of a hypothetical homologous series  $\text{RE}_n\text{Mn}_2\text{As}_2 \cdot n(\text{REAs})$  series, for which only the  $n = 0$  members ( $\text{RE}_n\text{Mn}_2\text{As}_2$  ( $\text{RE} = \text{Eu, Yb}$ )) were previously known. Unlike the analogous Zn-

containing members, there is no deficiency in the Mn sites so that fully stoichiometric formulas can be attained. The absence of a pseudogap and the large Mn 3d contribution to the DOS at the Fermi level leads to the prediction that these compounds should exhibit metallic conductivity and likely magnetic ordering.

### 3.5 References

1. Mandrus, D.; Sefat, A. S.; McGuire, M. A.; Sales, B.C. *Chem. Mater.* **2010**, *22*, 715-723.
2. Paglione, J.; Greene, R. L. *Nat. Phys.* **2010**, *6*, 645-658.
3. Villars, P.; Cenzual, K. Pearson's Crystal Data-Crystal Structure Database for Inorganic Compounds, ASM International, Materials Park, OH, **2010**.
4. Vidyasagar, K.; Hönlle, W.; von Schnering, H. G. *Z. Anorg. Allg. Chem.* **1996**, *622*, 518-524.
5. Payne, A. C.; Olmstead, M. M.; Kauzlarich, S. M.; Webb, D. J. *Chem. Mater.* **2001**, *13*, 1398-1406.
6. Hermann, R. P.; Grandjean, F.; Kauzlarich, S. M.; Jiang, J.; Brown, S.; Long, G. J. *Inorg. Chem.* **2004**, *43*, 7005-7013.
7. Rühl, R.; Jeitschko, W. *Mater. Res. Bull.* **1979**, *14*, 513-517.
8. Klüfers, P.; Neumann, H.; Mewis, A.; Schuster, H.-U. *Z. Naturforsch. B: Anorg. Chem., Org. Chem.* **1980**, *35*, 1317-1318.
9. Denissen, C. J. M.; Sun, D.; Kopinga, K.; de Jonge, W. J. M.; Nishihara, H.; Sakakibara, T.; Goto, T. *Phys. Rev. B* **1987**, *36*, 5316-5325.
10. Deng, Z.; Zhao, K.; Gu, B.; Han, W.; Zhu, J. L.; Wang, X. C.; Li, X.; Liu, Q. Q.; Yu, R. C.; Goko, T.; Frandsen, B.; Liu, L.; Zhang, J.; Wang, Y.; Ning, F. L.; Maekawa, S.; Uemura, Y. J.; Jin, C. Q. *Phys. Rev. B* **2013**, *88*, 081203-1-081203-5.
11. Lin, X.; Tabassum, D.; Rudyk, B. W.; Mar, A. *Inorg. Chem.* **2014**, *53*, 8341-8441.
12. Lin, X.; Mar, A. *Inorg. Chem.* **2013**, *52*, 7261-7270.
13. Sheldrick, G. M. SHELXTL, version 6.12, Bruker AXS Inc., Madison, WI, **2001**.

14. Gelato, L. M.; Parthé, E. *J. Appl. Crystallogr.* **1987**, *20*, 139-143.
15. Tank, R.; Jepsen, O.; Burkhardt, A.; Andersen, O. K. TB-LMTO-ASA Program, version 4.7, Max Planck Institut für Festkörperforschung, Stuttgart, Germany, **1998**.
16. Nientiedt, A. T.; Lincke, H.; Rodewald, U. Ch.; Pöttgen, R.; Jeitschko, W. Z. *Naturforsch. B: J. Chem. Sci.* **2011**, *66*, 221-226.
17. Lincke, H.; Hermes, W.; Nilges, T.; Pöttgen, R. *Solid State Sci.* **2008**, *10*, 1480-1484.
18. Taylor, J. B.; Calvert, L. D.; Despault, J. G.; Gabe, E. J.; Murray, J. J. *Less-Common Met.* **1974**, *37*, 217-232.

## Chapter 4

### **Narrowing the gap: From semiconductor to semimetal in the homologous series of rare-earth zinc arsenides $RE_{2-y}Zn_4As_4 \cdot n(REAs)$ and Mn-substituted derivatives $RE_{2-y}Mn_xZn_{4-x}As_4 \cdot n(REAs)$ ( $RE = La-Nd, Sm, Gd$ ).**

*A version of this chapter has been published. Lin, X.; Tabassum, D.; Mar, A. Dalton Trans. 2015, 44, 20254-20264*

#### **4.1 Introduction**

The ambitious goal for synthetic chemists to “design” new compounds with tunable properties must be tempered with the understanding that there are a limited number of experimental parameters under control and constraints on what is allowed by thermodynamic requirements.<sup>1</sup> Within these limitations, the idea of a homologous series does provide a convenient framework to systematize closely related compounds and to predict the existence of new members. In solid state chemistry, for example, many layered structures built up by stacking different types and numbers of slabs can be defined in terms of such homologous series and are found among oxides, chalcogenides, pnictides, and intermetallic compounds.<sup>2-6</sup> More complicated frameworks can be constructed through the condensation of modules or blocks of different sizes and shapes.<sup>7-9</sup> Of practical consequence, the physical and chemical properties are expected to vary gradually among members of a given homologous series; superconductivity and magnetic ordering are two examples of applications where small changes in crystal structure can have profound influence on properties.<sup>10-12</sup>

As part of an ongoing program to characterize ternary rare-earth transition-metal arsenides, which are of interest for their electrical and magnetic properties, investigations of *RE–Zn–As* systems have revealed many new phases:  $REZn_{0.67}As_2$  ( $RE = La-Nd, Sm$ ),<sup>13,14</sup>  $RE_{0.67}Zn_2As_2$  ( $RE = La-Nd, Sm$ ),<sup>15</sup>  $REZn_3As_3$  ( $RE = La-Nd, Sm$ ),<sup>16</sup>  $REZn_2As_3$  ( $RE = La-Pr$ ),<sup>17</sup>  $REZn_{2-x}As_2 \cdot n(REAs)$  ( $RE = La-Nd, Sm; n = 3, 4, 5, 6$ ),<sup>18</sup>  $REZn_2As_2$  ( $RE = Eu, Yb$ ),<sup>19-21</sup>  $Eu_2Zn_2As_3$ ,<sup>22</sup> and  $Eu_{11}Zn_6As_{12}$ .<sup>23</sup> Except for  $LaZn_3As_3$  and  $Eu_{11}Zn_6As_{12}$ , all of these compounds adopt structures derived by stacking Zn–As slabs in different sequences. The clearest manifestation of a homologous series is seen in  $REZn_{2-x}As_2 \cdot n(REAs)$ , for which successive members ( $n = 3, 4, 5, 6$ ) have trigonal structures built up by intergrowing [*REAs*] slabs of increasing thickness between zinc-deficient [ $Zn_2As_2$ ] slabs.<sup>18</sup> In fact,  $REZn_2As_2$  or the rare-earth-deficient  $RE_{0.67}Zn_2As_2$  can be considered to be the parent member ( $n = 0$ ) of this series.<sup>15,19-21</sup> As  $n$  increases, the electronic structure evolves from a small band-gap semiconductor to a semimetal. A parallel but less extensive homologous series of tetragonal structures with the general formula  $RE_2As_3 \cdot n(Zn_{2-x}As)$  can be expressed for  $REZn_{0.67}As_2$  ( $n = 1$ ) and  $REZn_2As_3$  ( $n = 3$ ), in which successive members exhibit increasingly thicker Zn-containing slabs.<sup>13,14,17</sup> Exploiting the richness of these *RE–Zn–As* systems and extending the emerging structural patterns observed, we posit that other homologous series can be prepared with different stacking sequences and thereby expand on our ability to control the electronic structure. There is also growing evidence that Mn can successfully substitute for Zn in these and related compounds,<sup>24</sup> which could impart interesting magnetic properties.

Through the directed synthesis of deliberately targeted compositions, three new series of ternary arsenides  $RE_{4-y}Zn_4As_6$  ( $RE = La-Nd$ ),  $RE_{5-y}Zn_4As_7$  ( $RE = Pr, Nd, Sm$ ,

Gd), and  $RE_{6-y}Zn_4As_8$  ( $RE = La-Nd, Sm, Gd$ ) have now been prepared, revealing the evolution of a different homologous series  $RE_{2-y}Zn_4As_4 \cdot n(REAs)$  ( $n = 2, 3, 4$ ) which is rare-earth-deficient instead of zinc-deficient. Quaternary arsenides  $RE_{2-y}Mn_xZn_{4-x}As_4 \cdot n(REAs)$  in which Mn partially substitutes for Zn were also prepared. We attempt to understand the nature of  $RE$  deficiencies in these compounds through entropy considerations, and examine the bonding and electronic structure through band structure calculations.

## 4.2 Experimental

### 4.2.1 Synthesis

Starting materials were freshly filed  $RE$  pieces (99.9%, Hefa), Mn powder (99.6%, Alfa-Aesar), Zn shot (99.99%, Aldrich), and As lumps (99.999%, Alfa-Aesar). The ternary arsenides were initially identified in the course of preliminary syntheses with various loading compositions. After the chemical compositions were established, including the occurrence of  $RE$  deficiencies, the loading compositions  $RE_{3.3}Zn_4As_6$ ,  $RE_{4.3}Zn_4As_7$ , and  $RE_{5.3}Zn_4As_8$  were systematically prepared from mixtures of the elements on a 0.3-g scale for a broad range of trivalent  $RE$  components ( $La-Nd, Sm, Gd$  and beyond). The mixtures were loaded into fused-silica tubes, which were evacuated and sealed. The tubes were heated at 500 °C for 2 d, heated to 750 °C over 20 h, held at this temperature for 7 d, and then cooled to room temperature over 2 d. The volatility of Zn and As poses a major problem in the synthesis of ternary  $RE-Zn-As$  phases in general; the preheating step at 500 °C helps minimize, but does not completely eliminate, loss of these components through sublimation. The existence of many competing phases with similar compositions, such as  $REZn_{0.67}As_2$ ,<sup>14</sup> also makes phase-pure samples

difficult to obtain, as evaluated from powder X-ray diffraction (XRD) patterns collected on an Inel diffractometer equipped with a curved position-sensitive detector (CPS 120) and a Cu  $K\alpha_1$  radiation source operated at 40 kV and 20 mA (**Figure A 2.1- A 2.3**). Substitution tends to be limited to the earlier *RE* components ( $RE_{4-y}Zn_4As_6$  (*RE* = La–Nd),  $RE_{5-y}Zn_4As_7$  (*RE* = Pr, Nd, Sm, Gd),  $RE_{6-y}Zn_4As_8$  (*RE* = La–Nd, Sm, Gd)) and further substitution beyond Gd was unsuccessful. Unit cell parameters refined from the powder XRD patterns are listed in **Table 4.1**. In separate experiments intended to investigate transition-metal substitution in the different arsenides  $REZn_3As_3$ ,<sup>16</sup> we had obtained quaternary phases  $RE_{4-y}Mn_xZn_{4-x}As_6$  (*RE* = Ce, Nd) which were subsequently recognized to belong to one of the three homologous series described above. Further attempts in Mn substitution within the other series resulted in two more examples,  $RE_{6-y}Mn_xZn_{4-x}As_8$  (*RE* = Sm, Gd).

**Table 0.1** Cell parameters for  $RE_{2-y}Zn_4As_4 \cdot n(REAs)$  ( $n = 2, 3, 4$ ) in powder samples obtained by reaction of the elements at 750 °C.

Compound	a(Å)	b(Å)	c(Å)
La <sub>4-y</sub> Zn <sub>4</sub> As <sub>6</sub>	4.1915(3)	62.637(6)	953.0(1)
Ce <sub>4-y</sub> Zn <sub>4</sub> As <sub>6</sub>	4.1947(3)	62.267(6)	948.9(1)
Pr <sub>4-y</sub> Zn <sub>4</sub> As <sub>6</sub>	4.1639(3)	62.660(6)	940.8(1)
Nd <sub>4-y</sub> Zn <sub>4</sub> As <sub>6</sub>	4.1570(3)	62.065(6)	928.8(1)
Pr <sub>5-y</sub> Zn <sub>4</sub> As <sub>7</sub>	4.1868(3)	24.161(1)	366.80(5)
Nd <sub>5-y</sub> Zn <sub>4</sub> As <sub>7</sub>	4.1804(3)	24.075(1)	364.36(5)
Sm <sub>5-y</sub> Zn <sub>4</sub> As <sub>7</sub>	4.1842(3)	23.906(1)	362.47(5)
Gd <sub>5-y</sub> Zn <sub>4</sub> As <sub>7</sub>	4.1710(3)	23.925(1)	360.47(5)
La <sub>6-y</sub> Zn <sub>4</sub> As <sub>8</sub>	4.2001(2)	83.028(6)	1268.5(1)
Ce <sub>6-y</sub> Zn <sub>4</sub> As <sub>8</sub>	4.1990(2)	82.863(6)	1265.2(1)
Pr <sub>6-y</sub> Zn <sub>4</sub> As <sub>8</sub>	4.1956(2)	82.113(6)	1251.8(1)
Nd <sub>6-y</sub> Zn <sub>4</sub> As <sub>8</sub>	4.1700(2)	81.990(6)	1234.7(1)
Sm <sub>6-y</sub> Zn <sub>4</sub> As <sub>8</sub>	4.1662(2)	81.877(6)	1230.7(1)
Gd <sub>6-y</sub> Zn <sub>4</sub> As <sub>8</sub>	4.1637(2)	81.747(6)	1227.3(1)

Crystals used for structure determination were obtained through further heat treatment at higher temperatures with the aim of exceeding melting points. The samples prepared above were reheated at 800 °C for 2 d, heated to 1050 °C over 20 h, held at this temperature for 7 d, slowly cooled to 500 °C at a rate of 3 °C/h, and cooled to room temperature over 2 d. Small crystals (constituting about 30% of the product) obtained from these reactions were examined on a JEOL JSM-6010LA scanning electron microscope and their compositions were determined by energy-dispersive X-ray (EDX) analyses on several points of individual crystals with acquisition times of 30 s each (**Table A 2.1**). In general, the experimental compositions agree well with expectations. The crystals were unfortunately too small (typically 0.1 mm in longest dimension) to permit physical property measurements such as electrical resistivity.

#### 4.2.2 Structure determination

Single crystals of ternary arsenides and some quaternary Mn-containing derivatives, whose chemical compositions were determined by EDX analyses, were mounted on a Bruker PLATFORM diffractometer equipped with a SMART APEX II CCD area detector and a graphite-monochromated Mo  $K\alpha$  radiation source. Intensity data were collected at room temperature using  $\omega$  scans in 5–8 batches at different  $\phi$  angles with a frame width of 0.3° and an exposure time of 12–15 s per frame. Face-indexed numerical absorption corrections were applied. Structure solution and refinement were carried out with use of the SHELXTL (version 6.12) program package.<sup>25</sup> Atom positions and labels were standardized with the program STRUCTURE TIDY.<sup>26</sup>

Within the  $RE_{4-y}Mn_xZn_{4-x}As_6$  series, crystals of an all-Zn ( $Pr_{4-y}Zn_4As_6$ ) and two Mn-doped members ( $Ce_{4-y}Mn_xZn_{4-x}As_6$ ,  $Nd_{4-y}Mn_xZn_{4-x}As_6$ ) were available. Intensity

symmetry and statistics indicated the centrosymmetric trigonal space group  $R\bar{3}m1$ . For  $\text{Pr}_{4-y}\text{Zn}_4\text{As}_6$ , the locations of three Pr, two Zn, and three As sites were initially found by direct methods. After refinement of this model, the displacement parameters for the Pr2 site were found to be much larger ( $U_{\text{eq}} = 0.04 \text{ \AA}^2$ ) than for the Pr1 and Pr3 sites ( $U_{\text{eq}} = 0.01 \text{ \AA}^2$ ). When the occupancies of these sites were freed, the refinements confirmed that the Pr2 site is partially occupied ( $\sim 0.5$ ) and now has more reasonable displacement parameters ( $U_{\text{eq}} = 0.01 \text{ \AA}^2$ ), whereas the Pr1 and Pr3 sites remained fully occupied (1.0). At this stage, the difference Fourier map revealed considerable residual electron density of  $12 \text{ e}^-/\text{\AA}^3$  at  $0, 0, 0.15$ , about  $1.3 \text{ \AA}$  away from the existing Zn1 site at  $0, 0, 0.13$ . This was assigned to be a secondary site, labeled Zn1b, while the original primary site was relabeled Zn1a. Refinements were performed in which these split sites were fixed to have equal displacement parameters and their occupancies were constrained to sum to unity. The occupancies converged to 0.9 Zn for the primary site (Zn1a) and 0.1 Zn for the secondary site (Zn1b). The other Zn site (Zn2) was well-behaved and unsplit. The difference map was now clean and the formula was determined to be  $\text{Pr}_{3.46(1)}\text{Zn}_4\text{As}_6$ , in reasonable agreement with the EDX analysis. For the Mn-doped compounds  $\text{Ce}_{4-y}\text{Mn}_x\text{Zn}_{4-x}\text{As}_6$  and  $\text{Nd}_{4-y}\text{Mn}_x\text{Zn}_{4-x}\text{As}_6$ , similar features of partially occupied *RE* sites and split Mn/Zn sites were encountered, but the distribution of Mn and Zn atoms within the metal sites (labeled *M1a/M1b* and *M2*) must be considered carefully. The closely spaced *M1a* and *M1b* sites were each allowed to be occupied by a mixture of Mn and Zn atoms, with the constraint that the occupancies sum to unity. Given the large number of free parameters, the refinements were unstable but tended towards high occupancy of Zn in the *M1a* site and of Mn in the *M1b* site. Based on this observation, we applied a

simplified structural model in which the *M1a* site is occupied exclusively by Zn atoms and the *M1b* site by Mn atoms; simultaneously, a mixture of Mn and Zn atoms can be accommodated within the unsplit *M2* site. Refinements of this model led to the formulas  $\text{Ce}_{3.32(1)}\text{Mn}_{1.1(1)}\text{Zn}_{2.9(1)}\text{As}_6$  and  $\text{Nd}_{3.34(1)}\text{Mn}_{0.92(6)}\text{Zn}_{3.08(6)}\text{As}_6$ .

Within the  $\text{RE}_{5-y}\text{Zn}_4\text{As}_7$  series, crystals of the Nd and Sm members were available. Their structures were solved in the trigonal space group  $P\bar{3}m1$ . From similar observations as above, it was determined that the *RE3* site is partially occupied (~0.4) and there is a set of split (*Zn1a/Zn1b*) and unsplit (*Zn2*) metal sites. Refinements following the procedure above led to the formulas  $\text{Nd}_{4.41(1)}\text{Zn}_4\text{As}_7$  and  $\text{Sm}_{4.39(1)}\text{Zn}_4\text{As}_7$ .

Within the  $\text{RE}_{6-y}\text{Mn}_x\text{Zn}_{4-x}\text{As}_8$  series, crystals of two all-Zn ( $\text{Nd}_{6-y}\text{Zn}_4\text{As}_8$ ,  $\text{Sm}_{6-y}\text{Zn}_4\text{As}_8$ ) and two Mn-doped members ( $\text{Sm}_{6-y}\text{Mn}_x\text{Zn}_{4-x}\text{As}_8$ ,  $\text{Gd}_{6-y}\text{Mn}_x\text{Zn}_{4-x}\text{As}_8$ ) were available. Their structures were solved in the trigonal space group  $R\bar{3}m1$ . The *RE3* site is partially occupied (0.3–0.4) and the metal sites are *M1* and *M2a/M2b*. The  $\text{Sm}_{6-y}\text{Mn}_x\text{Zn}_{4-x}\text{As}_8$  structure provides an example in which the site preferences of Mn and Zn within the split metal sites were clearly revealed from intermediate refinements which led to occupancies of 0.7 Zn / –0.1 Mn in the *M2a* site and –0.1 Zn / 0.5 Mn in the *M2b* site. The structural model was then simplified to *M2a* containing only Zn and *M2b* containing only Mn. Because the unsplit *M1* site showed a strong preference to be occupied by Zn atoms (0.9 Zn / 0.1 Mn), we chose to assign this site to contain exclusively Zn atoms. Final refinements led to the formulas  $\text{Nd}_{5.43(1)}\text{Zn}_4\text{As}_8$ ,  $\text{Sm}_{5.40(1)}\text{Zn}_4\text{As}_8$ ,  $\text{Sm}_{5.33(1)}\text{Mn}_{0.58(1)}\text{Zn}_{3.42(1)}\text{As}_8$ , and  $\text{Gd}_{5.27(1)}\text{Mn}_{0.62(1)}\text{Zn}_{3.38(1)}\text{As}_8$ .

In general, the structure refinements led to excellent agreement factors (conventional  $R(F)$  values ranging from 0.02 to 0.04) and featureless difference maps

$((\Delta\rho)_{\max}, (\Delta\rho)_{\min}$  values around 4 and  $-4$  e/Å<sup>3</sup>, respectively). Full experimental details (crystallographic data, positional and displacement parameters, interatomic distances) are given in **Table A 2.2- A 2.4**. Abbreviated crystallographic data are listed in **Table 4.2** and selected ranges of interatomic distances are listed in **Table 4.3**. Further data, in CIF format, have been sent to Fachinformationszentrum Karlsruhe, Abt. PROKA, 76344 Eggenstein-Leopoldshafen, Germany, as supplementary material No. CSD-430205 to 430213 and can be obtained by contacting FIZ (quoting the article details and the corresponding CSD numbers).

**Table 0.2** Abbreviated crystallographic data for  $RE_{2-y}Mn_xZn_{4-x}As_4 \cdot n(REAs)$  ( $n = 2, 3, 4$ ).<sup>a</sup>

<b>Formula</b>		<b>Ce<sub>3.32(1)</sub>Mn<sub>1.1(1)</sub>Zn<sub>2.9(1)</sub>As<sub>6</sub></b>	<b>Pr<sub>3.46(1)</sub>Zn<sub>4</sub>As<sub>6</sub></b>	<b>Nd<sub>3.34(1)</sub>Mn<sub>0.92(6)</sub>Zn<sub>3.08(6)</sub>As<sub>6</sub></b>
Formula mass (amu)	mass	1162.27	1197.14	1182.07
Space group		$R\bar{3}m1$	$R\bar{3}m1$	$R\bar{3}m1$
$Z$		3	3	3
$a$ (Å)		4.218(3)	4.2067(7)	4.1788(7)
$c$ (Å)		62.11(4)	62.637(10)	61.727(10)
$V$ (Å <sup>3</sup> )		957.0(13)	959.9(4)	933.5(3)
$\rho_c$ (g cm <sup>-3</sup> )		6.050	6.213	6.308
$\mu$ (mm <sup>-1</sup> )		33.34	35.57	35.57
$R(F)$ <sup>b</sup>		0.032	0.021	0.026
$R_w(F_o^2)$ <sup>c</sup>		0.058	0.045	0.056

<b>Formula</b>		<b>Nd<sub>4.41(1)</sub>Zn<sub>4</sub>As<sub>7</sub></b>	<b>Sm<sub>4.39(1)</sub>Zn<sub>4</sub>As<sub>7</sub></b>	<b>Nd<sub>5.43(1)</sub>Zn<sub>4</sub>As<sub>8</sub></b>
Formula mass (amu)		1420.58	1447.46	1644.54
Space group		$P\bar{3}m1$	$P\bar{3}m1$	$R\bar{3}m1$
$Z$		1	1	3
$a$ (Å)		4.197(3)	4.1703(6)	4.2038(11)
$c$ (Å)		24.204(15)	23.981(3)	82.97(2)
$V$ (Å <sup>3</sup> )		369.2(5)	361.19(12)	1269.8(7)
$\rho_c$ (g cm <sup>-3</sup> )		6.390	6.654	6.654
$\mu$ (mm <sup>-1</sup> )		37.49	39.96	37.38
$R(F)^b$		0.029	0.028	0.028
$R_w(F_o^2)^c$		0.051	0.067	0.094
<b>Formula</b>		<b>Sm<sub>5.40(1)</sub>Zn<sub>4</sub>As<sub>8</sub></b>	<b>Sm<sub>5.33(1)</sub>Mn<sub>0.58(1)</sub>Zn<sub>3.42(1)</sub>As<sub>8</sub></b>	<b>Gd<sub>5.27(1)</sub>Mn<sub>0.62(1)</sub>Zn<sub>3.38(1)</sub>As<sub>8</sub></b>
Formula Mass (amu)		1672.73	1656.80	1682.59
Space group		$R\bar{3}m1$	$R\bar{3}m1$	$R\bar{3}m1$
$Z$		3	3	3
$a$ (Å)		4.1689(4)	4.1691(9)	4.1398(12)
$c$ (Å)		82.103(9)	81.965(17)	81.17(2)
$V$ (Å <sup>3</sup> )		1235.8(3)	1233.8(6)	1204.8(8)
$\rho_c$ (g cm <sup>-3</sup> )		6.743	6.690	6.957
$\mu$ (mm <sup>-1</sup> )		40.53	39.97	43.15
$R(F)^b$		0.026	0.025	0.033
$R_w(F_o^2)^c$		0.053	0.053	0.088

<sup>a</sup> For all structures,  $T = 296(2)$  K,  $\lambda = 0.71073$  Å.

<sup>b</sup>  $R(F) = \sum ||F_o| - |F_c|| / \sum |F_o|$  for  $F_o^2 > 2\sigma(F_o^2)$ .

<sup>c</sup>  $R_w(F_o^2) = [\sum [w(F_o^2 - F_c^2)^2] / \sum wF_o^4]^{1/2}$ ;  $w^{-1} = [\sigma^2(F_o^2) + (Ap)^2 + Bp]$ , where  $p = [\max(F_o^2, 0) + 2F_c^2] / 3$ .

**Table 0.3** Ranges of interatomic distances (Å) for  $RE_{2-y}Mn_xZn_{4-x}As_4 \cdot n(REAs)$  ( $n = 2, 3, 4$ ).

	<b>Ce<sub>3.32(1)</sub>Mn<sub>1.1(1)</sub>Zn<sub>2.9(1)</sub>As<sub>6</sub></b>	<b>Pr<sub>3.46(1)</sub>Zn<sub>4</sub>As<sub>6</sub></b>	<b>Nd<sub>3.34(1)</sub>Mn<sub>0.92(6)</sub>Zn<sub>3.08(6)</sub>As<sub>6</sub></b>
<i>RE1</i> –As (CN6)	2.991(2)–3.067(2)	2.970(1)–3.050(1)	2.952(1)–3.012(1)
<i>RE2</i> –As (CN6)	2.901(2)	2.987(1)	2.917(1)
<i>RE3</i> –As (CN6)	3.023(2)	3.008(1)	2.978(1)
<i>M1a</i> –As (CN4)	2.530(2)–2.698(6)	2.507(1)–2.754(2)	2.497(1)–2.755(2)
<i>M1b</i> –As (CN4)	2.469(3)–2.747(18)	2.520(3)–2.804(10)	2.456(2)–2.817(8)
<i>M2</i> –As (CN4)	2.529(5)–2.581(2)	2.530(2)–2.571(1)	2.515(2)–2.570(1)
	<b>Nd<sub>4.41(1)</sub>Zn<sub>4</sub>As<sub>7</sub></b>	<b>Sm<sub>4.39(1)</sub>Zn<sub>4</sub>As<sub>7</sub></b>	
<i>RE1</i> –As (CN6)	2.977(1)–3.001(2)	2.950(1)–2.969(1)	
<i>RE2</i> –As (CN6)	2.962(2)–3.018(2)	2.938(1)–2.986(1)	
<i>RE3</i> –As (CN6)	2.969(2)	2.947(1)	
<i>M1a</i> –As (CN4)	2.490(2)–2.809(3)	2.473(1)–2.837(3)	
<i>M1b</i> –As (CN4)	2.502(3)–2.805(12)	2.487(3)–2.776(11)	
	<b>Nd<sub>5.43(1)</sub>Zn<sub>4</sub>As<sub>8</sub></b>	<b>Nd<sub>5.43(1)</sub>Zn<sub>4</sub>As<sub>8</sub></b>	
<i>RE1</i> –As (CN6)	2.970(1)–3.008(1)	2.940(1)–2.973(1)	
<i>RE2</i> –As (CN6)	2.960(1)–3.025(1)	2.931(1)–2.989(1)	
<i>RE3</i> –As (CN6)	2.973(1)	2.944(1)	
<i>RE4</i> –As (CN6)	2.989(1)	2.956(1)	
<i>M1</i> –As (CN4)	2.510(3)–2.578(1)	2.506(2)–2.565(1)	
<i>M2a</i> –As (CN4)	2.496(1)–2.793(3)	2.475(1)–2.815(2)	
<i>M2b</i> –As (CN4)	2.504(4)–2.818(17)	2.483(2)–2.780(10)	
	<b>Sm<sub>5.33(1)</sub>Mn<sub>0.58(1)</sub>Zn<sub>3.42(1)</sub>As<sub>8</sub></b>	<b>Gd<sub>5.27(1)</sub>Mn<sub>0.62(1)</sub>Zn<sub>3.38(1)</sub>As<sub>8</sub></b>	
<i>RE1</i> –As (CN6)	2.942(1)–2.973(1)	2.913(1)–2.949(1)	
<i>RE2</i> –As (CN6)	2.934(1)–2.989(1)	2.899(1)–2.978(1)	
<i>RE3</i> –As (CN6)	2.917(1)	2.871(1)	
<i>RE4</i> –As (CN6)	2.958(1)	2.931(1)	
<i>M1</i> –As (CN4)	2.507(2)–2.570(1)	2.522(2)–2.558(1)	
<i>M2a</i> –As (CN4)	2.488(1)–2.778(3)	2.495(1)–2.715(3)	
<i>M2b</i> –As (CN4)	2.455(2)–2.811(7)	2.426(2)–2.764(9)	

### 4.2.3 Band structure calculations

Tight-binding linear muffin tin orbital band structure calculations were performed within the local density and atomic spheres approximation with use of the Stuttgart TB-LMTO-ASA program (version 4.7).<sup>27</sup> Fully stoichiometric models were constructed for the series  $\text{La}_2\text{Zn}_4\text{As}_4 \cdot n(\text{LaAs})$  with  $n = 0, 1, 2, 3, 4, 5$ , and  $\infty$ . Cell parameters and atomic positions were taken from single-crystal structure determinations where these were available, in which the *RE* component was replaced by La to avoid computational problems associated with filled f orbitals. The calculations for  $\text{La}_2\text{Zn}_4\text{As}_4$  ( $n = 0$ , based on the  $\text{CaAl}_2\text{Si}_2$ -type structure of  $\text{Ce}_{0.63}\text{Zn}_2\text{As}_2$ )<sup>15</sup> and  $\text{LaAs}$  ( $n = \infty$ , based on the rocksalt-type structure in space group  $Fm\bar{3}m$  with  $a = 6.16 \text{ \AA}$ )<sup>28,29</sup> reproduce results reported previously<sup>18</sup> and are included here for comparison. For the hypothetical compounds  $\text{La}_3\text{Zn}_4\text{As}_5$  ( $n = 1$ ) and  $\text{La}_7\text{Zn}_4\text{As}_9$  ( $n = 5$ ), the cell parameters were extrapolated from the trends followed by the real compounds ( $n = 0, 2, 3, 4$ ) and the atomic positions were chosen to give La–As bonds of  $3.0 \text{ \AA}$  and Zn–As bonds of  $2.5\text{--}2.6 \text{ \AA}$ , similar to those found in the real compounds. The basis set consisted of La 6s/6p/5d/4f, Zn 4s/4p/3d, and As 4s/4p/4d orbitals, with the La 6p and As 4d orbitals being downfolded. Integrations in reciprocal space were carried out with an improved tetrahedron method over 131 irreducible  $k$  points within the first Brillouin zone from a  $12 \times 12 \times 8$  mesh for those structures in space group  $P\bar{3}m1$ , or over 189 irreducible  $k$  points from a  $12 \times 12 \times 12$  mesh for those structures in space group  $R\bar{3}m1$ .

### 4.2.4 Results and discussion

The new ternary arsenides  $\text{RE}_{4-y}\text{Zn}_4\text{As}_6$  ( $\text{RE} = \text{La–Nd}$ ),  $\text{RE}_{5-y}\text{Zn}_4\text{As}_7$  ( $\text{RE} = \text{Pr, Nd, Sm, Gd}$ ), and  $\text{RE}_{6-y}\text{Zn}_4\text{As}_8$  ( $\text{RE} = \text{La–Nd, Sm, Gd}$ ) belong to a homologous series

with the general formula  $RE_{2-y}Zn_4As_4 \cdot n(REAs)$  ( $n = 2, 3, 4$ ), which joins the previously known series  $REZn_{2-x}As_2 \cdot n(REAs)$  ( $n = 3, 4, 5, 6$ )<sup>18</sup> to form two daughter branches of an emerging family of trigonal structures that share  $RE_{2-y}Zn_4As_4$  (represented by  $RE_{0.67}Zn_2As_2$  ( $RE = La-Nd, Sm$ )<sup>15</sup> or  $REZn_2As_2$  ( $RE = Eu, Yb$ )<sup>19-21</sup>) as the parent  $n = 0$  member. In all of these phases, Mn atoms can partially substitute for Zn atoms, resulting in the quaternary arsenides  $RE_{2-y}(Mn,Zn)_4As_4 \cdot n(REAs)$ , presented here, and  $RE(Mn,Zn)_{2-x}As_2 \cdot n(REAs)$ , reported previously.<sup>18</sup> Similarly, the known phases  $RE_{2-y}(Mn,Zn)_4As_4$  ( $RE = La-Nd, Sm-Lu$ )<sup>24</sup> can be considered to be the  $n = 0$  members of these more complicated Mn-containing homologous series.

Like the previously known arsenides  $REZn_{2-x}As_2 \cdot n(REAs)$ , the new arsenides  $RE_{2-y}Zn_4As_4 \cdot n(REAs)$  were obtained by reactions of the elements at 750 °C with loading compositions matching the formulas determined from single-crystal structure determinations. In contrast to  $REZn_{2-x}As_2 \cdot n(REAs)$ , which could generally be prepared with high phase purity (>80%),<sup>18</sup>  $RE_{2-y}Zn_4As_4 \cdot n(REAs)$  phases were always found in conjunction with other phases and their proportions become lower on progressing to later  $RE$  components (**Figure A 2.1- A 2.3**). Numerous attempts were made to adjust the stoichiometry (e.g., addition of up to 5% excess  $RE$  or up to 10% excess As), temperature (e.g., increase to 800 °C or to 900 °C), and duration of the reactions but they did not improve phase purity significantly. These phases may well have limited stability within narrow temperature ranges or exhibit complex equilibria that remain to be clarified. The cell parameters of  $RE_{2-y}Zn_4As_4 \cdot n(REAs)$  refined from the powder XRD patterns show some irregular trends (**Table 4.1**), likely attributable to variability in the  $RE$  deficiencies (which are undetermined). In general, however, the unit cell volumes do decrease

monotonically in accordance with the lanthanide contraction on progressing to smaller *RE* components. These phases adopt trigonal structures in space group  $R\bar{3}m1$  with  $Z = 3$  for  $RE_{4-y}Zn_4As_6$  and  $RE_{6-y}Zn_4As_8$ , or space group  $P\bar{3}m1$  with  $Z = 1$  for  $RE_{5-y}Zn_4As_7$ . The tripling of the unit cell in  $RE_{4-y}Zn_4As_6$  and  $RE_{6-y}Zn_4As_8$  arises from a tripling of the *c*-parameter relative to that in  $RE_{5-y}Zn_4As_7$ . The trends in cell parameters are best seen by comparing the cell volume per formula unit (f.u.),  $V/Z$ , and the reduced *c*-parameter,  $c/Z$ , among these series (**Figure 4.1**). For every increment of *n* in  $RE_{2-y}Zn_4As_4 \cdot n(REAs)$ , the normalized cell volume increases by about  $50 \text{ \AA}^3$  and the reduced *c*-parameter increases by  $3.3\text{--}3.4 \text{ \AA}$ , while the *a*-parameter remains constant at  $4.2 \text{ \AA}$ , a manifestation of clear structural regularity as described further below.

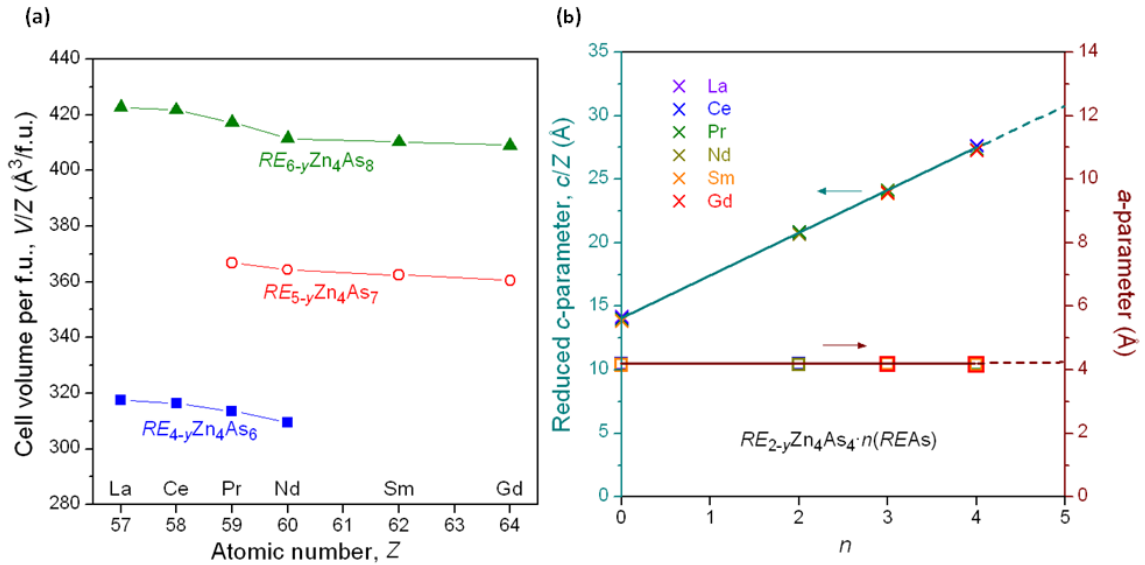


**Figure 4.1** (a) Plots of cell volume per formula unit for different RE members of the three series  $RE_{4-y}Zn_4As_6$ ,  $RE_{5-y}Zn_4As_7$ , and  $RE_{6-y}Zn_4As_8$ . (b) Plots of cell lengths as a function of *n* in the homologous series  $RE_{2-y}Zn_4As_4 \cdot n(REAs)$ . The *c*-parameters are normalized by dividing by 3 for structures in space group.

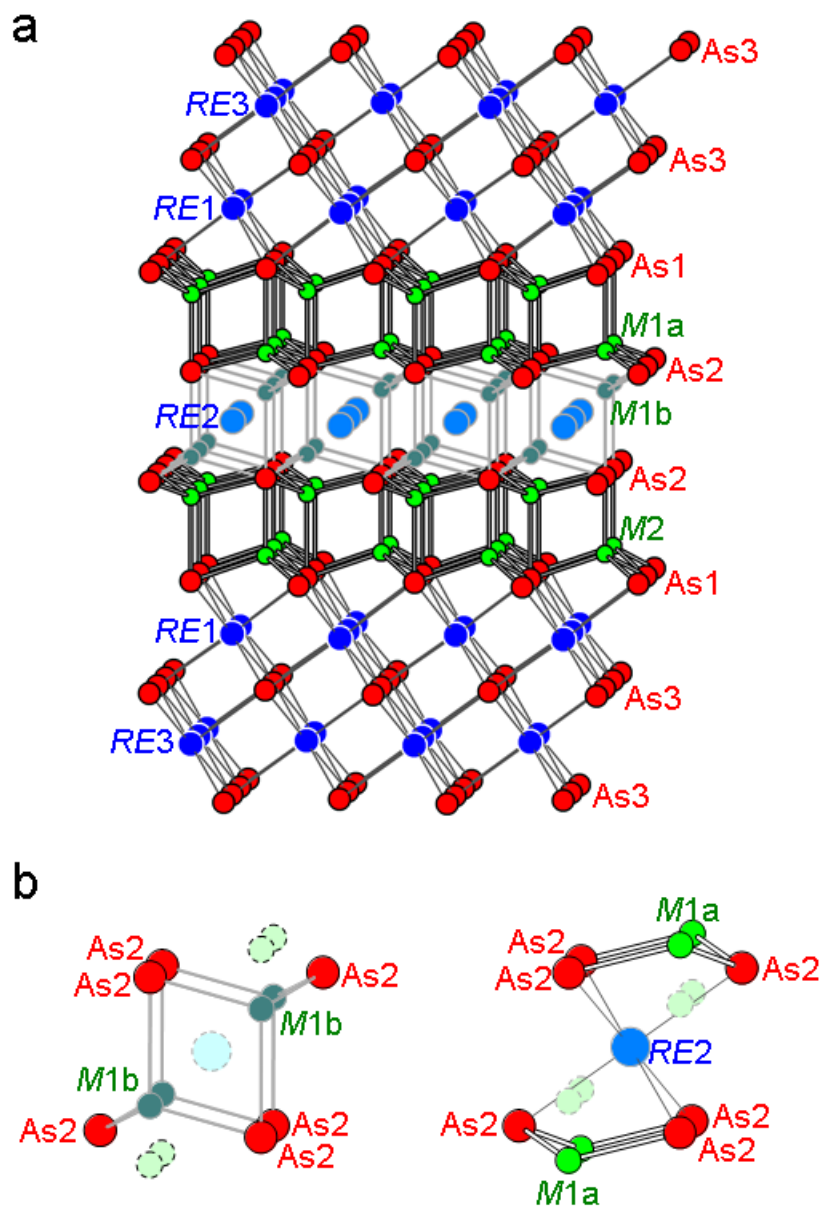


**Figure 4.2** (a) A fragment of the structure of  $RE_{4-y}M_4As_6$ , the  $n = 2$  member of  $RE_{2-y}M_4As_4 \cdot n(REAs)$  ( $M = Mn, Zn$ ). The  $RE2$  sites (lightly shaded) are partially occupied at 0.3–0.4. Mn and Zn atoms are found in a set of split  $M1a$  (primary, with occupancy of 0.7–0.8, preferred by Zn) and  $M1b$  sites (secondary, with occupancy of 0.2–0.3, preferred by Mn), or in the unsplit  $M2$  sites (preferred by Zn). (b) Local coordination within the  $[M_2As_2]$  slab is either tetrahedral geometry exhibited by  $M1b$  sites or octahedral geometry by  $RE2$  sites, with  $M1a$  sites in adjacent slabs.

To describe the trigonal crystal structures of the all-Zn-containing arsenides  $RE_{2-y}Zn_4As_4 \cdot n(REAs)$  and the Mn-doped arsenides  $RE_{2-y}(Mn,Zn)_4As_4 \cdot n(REAs)$  together, we combine the formulas as  $RE_{2-y}M_4As_4 \cdot n(REAs)$ , in which  $M$  represents the sites occupied by Zn or Mn atoms. We first consider the  $n = 2$  member of the homologous series having a hypothetical idealized formula that is fully stoichiometric,  $RE_4M_4As_6$ . Because the  $c$ -parameter is very long (62 Å), it is helpful to examine just a part of the structure at the outset (**Figure 4.2a**).

The structure is built up by condensing two types of slabs,  $[REAs]$  constructed from edge-sharing  $RE$ -centred octahedra and  $[M_2As_2]$  constructed from edge-sharing  $M$ -centred tetrahedra, which are stacked along the  $c$ -direction. Equivalently, the structure consists of an arrangement of close-packed nets of As atoms, with 2/3 of the octahedral interstices occupied by  $RE$  atoms and 1/3 of the tetrahedral interstices by  $M$  atoms. The  $[REAs]$  slabs are fragments of the rocksalt (NaCl-type) structure, which is adopted by the binary rare-earth monoarsenides  $REAs$  themselves.<sup>28,29</sup> The  $[M_2As_2]$  slabs are the same as the anionic substructure of the  $CaAl_2Si_2$ -type structure adopted by the parent  $n = 0$  member of the homologous series.<sup>15,19–21</sup> The slabs are intergrown following the repeating sequence  $[REAs]_3-[M_2As_2]-[REAs]-[M_2As_2]-\dots$ , in which there are single-slab  $[REAs]$  or triple-slab  $[REAs]_3$  blocks. The characteristic feature is the presence of “sandwiches”  $[M_2As_2]-[REAs]-[M_2As_2]$  that interrupt the regular rocksalt-type arrangement of  $REAs$ . On proceeding from the idealized structure  $RE_4M_4As_6$  to the true structure  $RE_{4-y}M_4As_6$ , two complications arise. First, there are  $RE$  deficiencies, and the partially filled  $RE$  sites (labeled here as  $RE2$ ) are always found in the isolated  $[REAs]$  slab inside the sandwiches. The occupancy is typically 0.3–0.4 in these deficient  $RE$

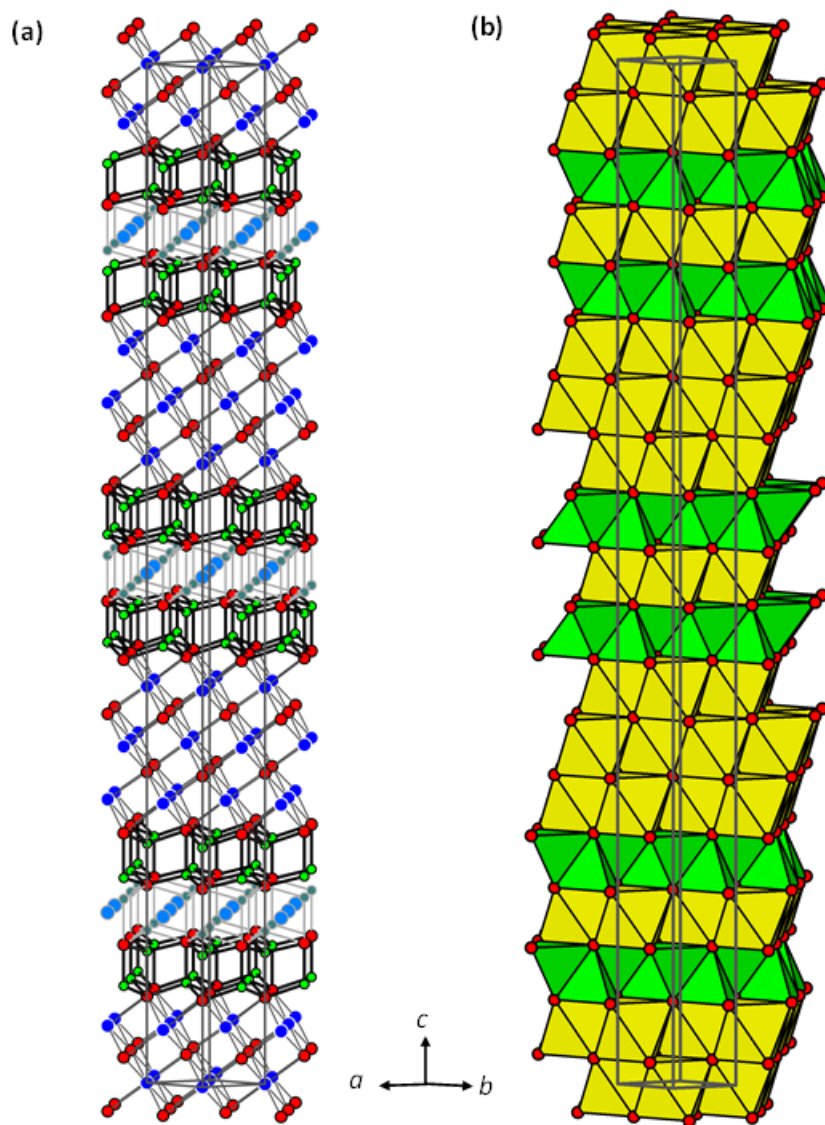


**Figure 4.3** Full structure of  $RE_{4-y}M_4As_6$ , with unit cell outlined, in (a) ball-and-stick and (b) polyhedral representations, showing the intergrowth of  $[REAs]$  slabs built from edge-sharing octahedra and  $[M_2As_2]$  slabs built from edge-sharing tetrahedra.

sites. Second, as a result of the space liberated by these  $RE$  deficiencies, a secondary metal site (labeled as  $M1b$ ) appears which is split off from the main metal site (labeled as  $M1a$ ) found in the inner sides of the  $[M_2As_2]$  slabs of the sandwiches (**Figure 4.2b**). The occupancy is typically 0.7–0.8 in the primary metal sites and 0.2–0.3 in the secondary

sites. On a local level, if the secondary metal site  $M1b$  is occupied, the adjacent  $RE$  site is empty in the slab inside the sandwiches; if instead the primary metal site  $M1a$  is occupied, the  $RE$  site can be filled. In Mn-doped derivatives, such as  $Ce_{3.3}Mn_{1.1}Zn_{2.9}As_6$ , there is a preference for Mn atoms to occupy the secondary site ( $M1b$ ) while the Zn atoms occupy the primary site ( $M1a$ ); the unsplit site ( $M2$ ) is generally preferred by Zn atoms. The full structure of  $RE_{4-y}M_4As_6$  can now be appreciated in both ball-and-stick and polyhedral representations (**Figure 4.3**).

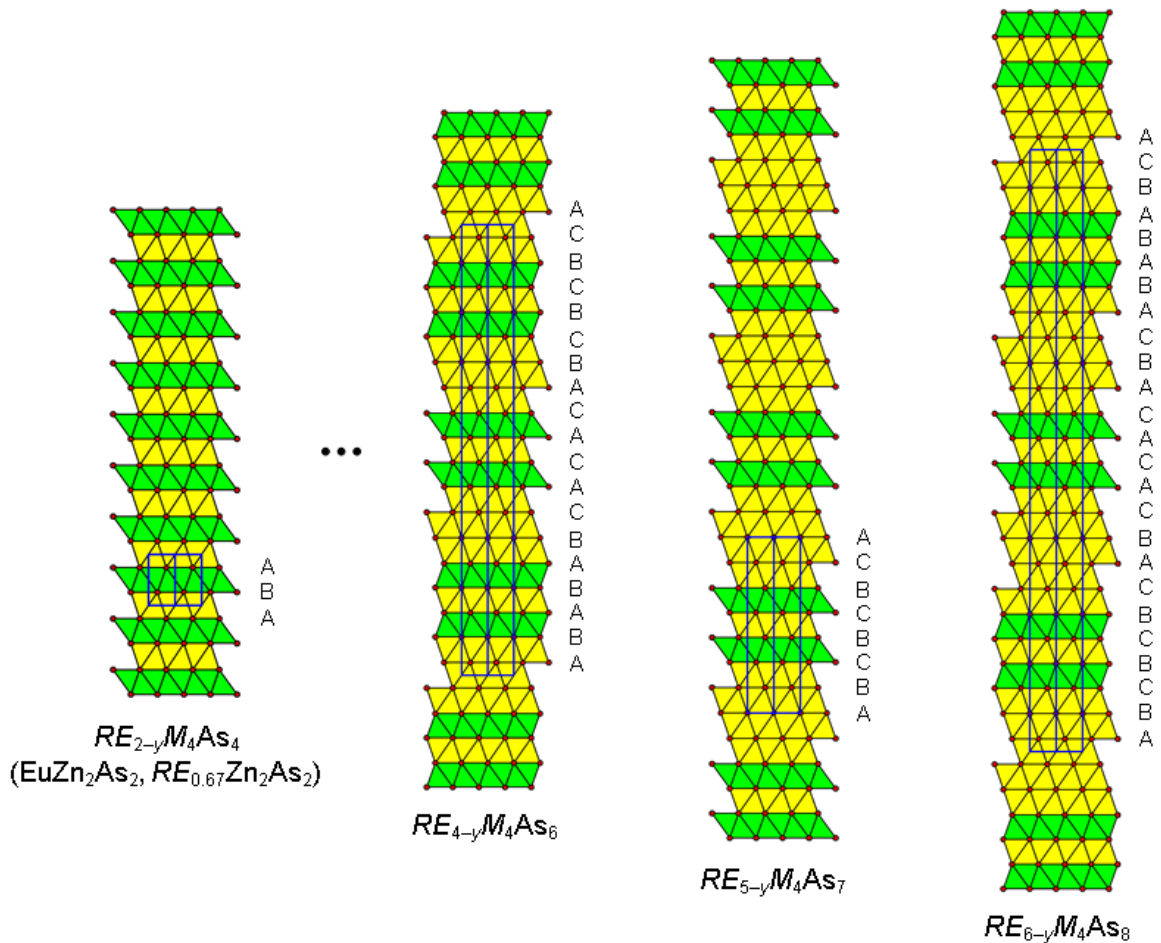


**Figure 4.4** Structures of the  $n = 0, 2, 3,$  and  $4$  members of the homologous series  $RE_{2-y}M_4As_{4+n}(REAs)$  in terms of  $[REAs]$  slabs (yellow) and  $[M_2As_2]$  slabs (green). The stacking sequences of As nets are also marked.

The evolution of the homologous series  $RE_{2-y}M_4As_4 \cdot n(REAs)$  is shown in **Figure 4.4**. The parent  $n = 0$  member  $RE_{2-y}M_4As_4$ , which is fully stoichiometric when  $RE$  is divalent ( $EuZn_2As_2$ ,  $YbZn_2As_2$ )<sup>19-21</sup> but substoichiometric when  $RE$  is trivalent ( $RE_{0.67}Zn_2As_2$ ),<sup>15</sup> adopts the  $CaAl_2Si_2$ -type structure having a simple *hcp* stacking sequence (AB) of As nets and constructed from alternating  $[REAs]$  and  $[M_2As_2]$  slabs. For every increment in  $n$ , the intervening rocksalt-type blocks between the  $[M_2As_2]$ – $[REAs]$ – $[M_2As_2]$  sandwiches increase in thickness by one; this corresponds to a lengthening of the reduced  $c$ -parameter by 3.3–3.4 Å, noted earlier. The  $n = 1$  member is unknown but would have the formula  $RE_{3-y}M_4As_5$ . The  $n = 2$  member is  $RE_{4-y}M_4As_6$  described above, having a long stacking sequence (ABABABCACACABCBCBC) of 18 As nets. These stacking sequences can be expressed in more compact notation, by identifying nets as being surrounded in hexagonal vs. cubic arrangements (e.g.,  $h = \underline{ABA}$ ;  $c = \underline{ABC}$ ), or by simply specifying the lattice ( $H$  vs.  $R$ ) and the number of layers present.<sup>30</sup> For  $RE_{4-y}M_4As_6$ , the stacking sequence is thus  $h^4c^2$  ( $= hhhhcc$ ) or  $18R$ . As summarized in **Table 4.4**, each increment in  $n$  adds a new layer in cubic stacking sequence ( $c$ ). Depending on the repeat length of the sequence, the space group is either

**Table 0.4** Observed and predicted members of homologous series  $RE_{2-y}M_4As_4 \cdot n(REAs)$ .

$n$	idealized formula	space group	fraction of sites occupied		As stacking	$c$ (Å)
			oct. by $RE$	tet. by M		
0	$RE_2M_4As_4$ <sup>a</sup>	$P\bar{3}m1$	2/4	2/4	$h^4$ (4H)	14.0
1	$RE_3M_4As_5$ <sup>b</sup>	$R\bar{3}m1$	3/5	2/5	$h^4c$ (15R)	$17.3 \times 3 = 51.9$
2	$RE_4M_4As_6$	$R\bar{3}m1$	4/6	2/6	$h^4c^2$ (18R)	$20.7 \times 3 = 62.1$
3	$RE_5M_4As_7$	$P\bar{3}m1$	5/7	2/7	$h^4c^3$ (7H)	24.0
4	$RE_6M_4As_8$	$R\bar{3}m1$	6/8	2/8	$h^4c^4$ (24R)	$27.4 \times 3 = 82.2$
5	$RE_7M_4As_9$ <sup>b</sup>	$R\bar{3}m1$	7/9	2/9	$h^4c^5$ (27R)	$30.7 \times 3 = 92.1$

$P\bar{3}m1$  ( $Z = 1$ ) and  $R\bar{3}m1$  ( $Z = 3$ ). The  $c$ -parameters, which can be estimated from an increase of  $3.3 \text{ \AA}$  for every additional  $[REAs]$  slab, agree well with observations. Experimentally, we have determined the structures of the higher members  $RE_{5-y}M_4As_7$  ( $n = 3$ ) and  $RE_{6-y}M_4As_8$  ( $n = 4$ ), the latter having a very long  $c$ -parameter of  $82 \text{ \AA}$ .

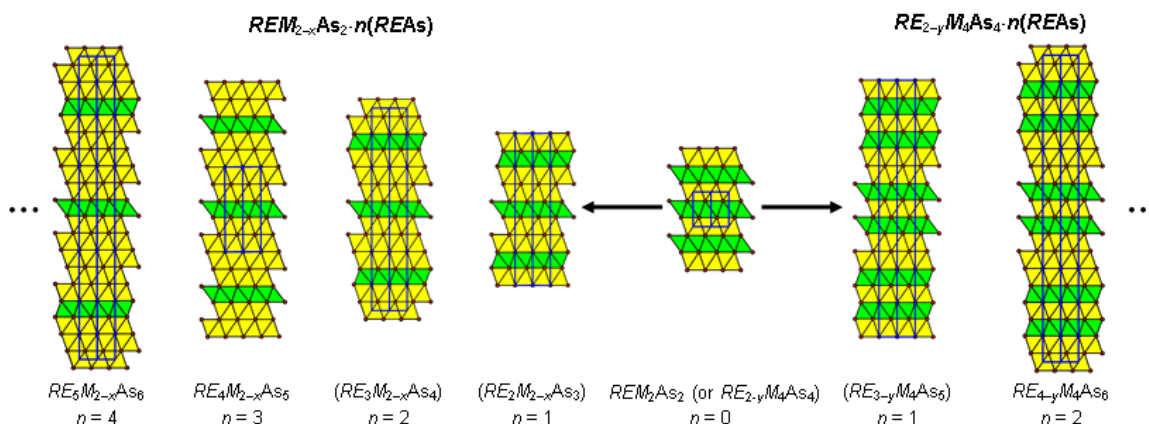


**Figure 4.5** Starting from the same parent member  $REM_2As_2$  (or  $RE_2M_4As_4$ ), inserting additional  $[REAs]$  slabs leads to either the metal-deficient homologous series  $REM_{2-x}As_2 \cdot n(REAs)$  (left) and the rare-earth-deficient homologous series  $RE_{2-y}M_4As_4 \cdot n(REAs)$  (right). Hypothetical structures have their formulas shown in parentheses.

Through the same structural principle of increasing the number of  $[REAs]$  slabs, the parent  $n = 0$  member,  $REM_2As_2$  or  $RE_{2-y}M_4As_4$ , bifurcates into metal-deficient  $REM_{2-x}As_2 \cdot n(REAs)$  and rare-earth-deficient  $RE_{2-y}M_4As_4 \cdot n(REAs)$  homologous series (**Figure 4.5**). There are some interesting points worth noting in comparing members of these two series. The lower members ( $RE_2M_{2-x}As_3$  and  $RE_3M_{2-x}As_4$  of the first series;  $RE_{3-y}M_4As_5$  of the second series) are missing and to date we have not been successful in preparing them, at least with early  $RE$  components. (The existence of fully stoichiometric  $Eu_2Zn_2As_3$  has been reported but it adopts an unrelated monoclinic

structure.<sup>22)</sup> If only the ideal formulas are considered, each member of the first series necessarily has a compositionally identical counterpart with an even-numbered member of the second series. For example, doubling the fully stoichiometric formula  $RE_2M_2As_3$ , which is the  $n = 1$  member in the first series, gives  $RE_4M_4As_6$ , which is the same formula as the  $n = 2$  member in the second series. They have the same number of [REAs] slabs, which are distributed evenly (2–2–...) in  $RE_2M_2As_3$  and unevenly (1–3–...) in  $RE_4M_4As_6$ . However, in practice, their compositions can be distinguished because of the occurrence of significant deficiencies in the  $M$  or  $RE$  sites, respectively. There are also members from the two homologous series which, by virtue of having equal numbers of repeating As layers, share nearly identical cell parameters and crystallize in the same space group. For example, although the stacking sequence differs in  $RE_5M_{2-x}As_6$  ( $h^2c^4$ ) in the first homologous series and  $RE_{4-y}M_4As_6$  ( $h^4c^2$ ) in the second homologous series, they have the same number of As nets (18R) in space group  $R\bar{3}m1$  (compare the structures shown in **Figure 4.5**). Thus, it can be very difficult to distinguish between them experimentally from their cell parameters alone (cf.,  $a = 4.246(3)$  Å,  $c = 62.49(5)$  Å for  $Pr_5Zn_{1.7}As_6$ ;<sup>18</sup>  $a = 4.2067(7)$  Å,  $c = 62.637(10)$  Å for  $Pr_{3.5}Zn_4As_6$ ).

In both homologous series of arsenides, the absence of homoatomic bonding (metal-metal or As–As) implies that all atoms have closed-shell ( $d^0$ ;  $RE^{3+}$ ,  $As^{3-}$ ), closed-subshell ( $d^{10}$ ;  $Zn^{2+}$ ), or half-filled-subshell ( $d^5$ ;  $Mn^{2+}$ ) configurations. Given these assignments, the fully stoichiometric formulas of these arsenides would be electron-excessive:  $(RE^{3+})(M^{2+})_2(As^{3-})_2e^- \cdot n(RE^{3+}As^{3-})$  for the first homologous series, and  $(RE^{3+})_2(M^{2+})_4(As^{3-})_4(e^-)_2 \cdot n(RE^{3+}As^{3-})$  for the second homologous series. The electron excess can be removed through deficiencies in the  $M$  site,  $REM_{2-x}As_2 \cdot n(REAs)$ , or in the

*RE* site,  $RE_{2-y}M_4As_4 \cdot n(REAs)$ . The actual formulas are  $REM_{1.7-1.8}As_2 \cdot n(REAs)$  and  $RE_{1.3-1.4}M_4As_4 \cdot n(REAs)$ , which indicate that the deficiencies do not have to be quite as low as in the strictly valence-precise formulations,  $(RE^{3+})(M^{2+})_{1.5}(As^{3-})_2 \cdot n(RE^{3+}As^{3-})$  and  $(RE^{3+})_{1.33}(M^{2+})_4(As^{3-})_4 \cdot n(RE^{3+}As^{3-})$ , respectively. The small discrepancy between the predicted and actual deficiencies may suggest the existence of a slight homogeneity range, which would be possible especially if there is no band gap in the density of states (see later). The question of which site accommodates the deficiencies, *RE* or *M*, is an interesting one which we attempt to address below.

The occurrence of vacancies entails changes in both enthalpy and entropy terms for the free energy of a substoichiometric phase relative to the hypothetical fully stoichiometric one.<sup>31</sup> In general, it might be thought that removing an atom from a structure is unfavorable from an enthalpy standpoint because of the loss of bonding interactions. However, even at 0 K, low concentrations of vacancies result in a gain in entropy that can offset the cost of creating these defects. Of course, the conventional treatment of defects applies to very small deviations from ideal stoichiometry, not the significant deviations seen here in these arsenides. However, we can make use of similar ideas to construct a qualitative argument. Previous analysis of the electronic structure of  $La_4Zn_2As_5$  (a member of the first homologous series) revealed that removal of electrons from the fully stoichiometric structure depopulates weakly antibonding La–As and Zn–As states so that the Fermi level is lowered to a pseudogap.<sup>18</sup> In other words, a possible driving force is the optimization of bonding, with the formation of deficiencies enthalpically favoured up to a certain point; because there is considerable delocalization of the bonding electrons, however, we gain no insight as to whether La or Zn sites prefer

to be deficient. We consider now the entropy changes, which have two parts: a configurational term, which depends on the distribution of vacancies and atoms within a given site, and a vibrational (or thermal) term, which depends on the bond distortions experienced by neighbouring atoms surrounding a vacancy. Given that these arsenides were formed at  $\sim 1000$  K rather than  $\sim 0$  K, these entropy terms are undoubtedly important contributions to their stability. The configurational entropy favours deficiency in the lower valent site than in the higher valent site because more vacancies can be created for the same electron excess to be removed. Thus, the default response is for the  $M^{2+}$  sites rather than the  $RE^{3+}$  sites to be deficient. The vibrational entropy favours deficiency in the site with the higher coordination number (CN) than with the lower one because greater disruption of the surrounding atoms can take place. However, this is not simply a matter of comparing the coordination of As atoms surrounding  $RE$  (CN6) vs.  $M$  (CN4). To include any eventual  $RE-M$  or  $M-M$  contacts, it seems more appropriate to set a cutoff of  $\sim 3.6$  Å to define the CN around a given  $RE$  or  $M$  site.

In the first homologous series,  $REM_{2-x}As_{2 \cdot n}(REAs)$ , the  $RE$  sites have CN6–9 (consisting of 6 As atoms and 0–3  $M$  atoms) whereas the  $M$  sites have CN10 (consisting of 4 As, 3  $RE$ , and 3  $M$  atoms). Thus, both configurational and vibrational entropy favour deficiency in the  $M$  sites, consistent with observations. In the second homologous series,  $RE_{2-y}M_4As_{4 \cdot n}(REAs)$ , the  $RE$  sites have CN6–12 (consisting of 6 As atoms and 0–6  $M$  atoms) whereas the  $M$  sites have CN10 (consisting of 4 As, 3  $RE$ , and 3  $M$  atoms). The key difference is that the  $RE$  sites sandwiched between the  $[M_2As_2]$  slabs have an especially high CN of 12; the occurrence of vacancies in these  $RE$  sites may then confer greater vibrational entropy, enough to overcome the normal preference for Zn

deficiencies. Note that in the parent  $n = 0$  member common to both homologous series, the  $RE$  atoms are always sandwiched between  $[M_2As_2]$  slabs; consequently, for trivalent  $RE$  components,  $RE_{0.67}Zn_2As_2$  are also deficient in  $RE$ . The occurrence of a split  $M$  site that enters the liberated space of a  $RE$  vacancy in the structures of  $RE_{2-y}M_4As_4 \cdot n(REAs)$  is a manifestation of the significant bond relaxation that takes place, and this feature has the benefit of contributing additional configurational entropy. Note that the reverse – split  $RE$  sites within the space vacated by a  $Zn$  deficiency – cannot happen because  $RE$  atoms are too big to enter into the  $Zn$ -containing slabs.

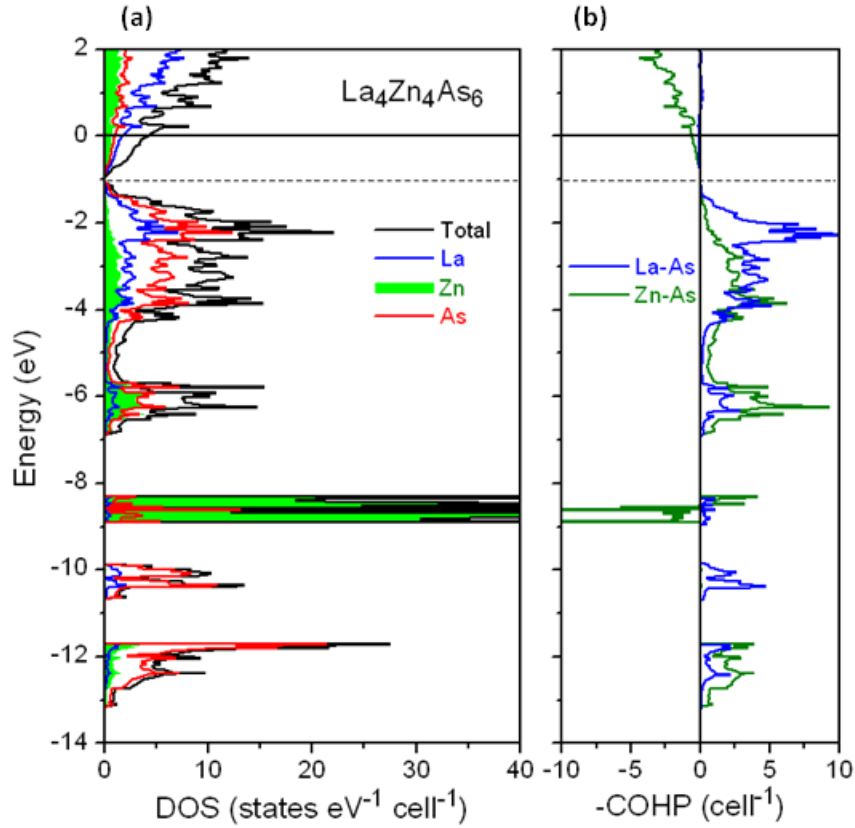


**Figure 4.6** (a) Density of states (DOS) and (b) crystal orbital Hamilton population (–COHP) curves for idealized fully stoichiometric model  $La_4Zn_4As_6$ . Removal of two electrons per formula unit lowers the Fermi level from 0 eV (solid line) to the gap at –1 eV (dashed line).

The electronic band structures of members within the homologous series are expected to vary gradually as more [REAs] slabs are introduced. A calculation was first performed on a fully stoichiometric model of an intermediate member ( $n = 2$ ), with the idealized formula  $\text{La}_4\text{Zn}_4\text{As}_6$ . The density of states (DOS) curve shows a broad valence band (from  $-7$  to  $-1$  eV) that is separated by a small gap of  $0.04$  eV from a conduction band extending upwards in energy (**Figure 4.6**). Consistent with the electron excess implied by this formula,  $(\text{La}^{3+})_4(\text{Zn}^{2+})_4(\text{As}^{3-})_6(\text{e}^-)_2$ , the Fermi level cuts through the bottom of the conduction band. Removal of exactly two electrons per formula unit lowers the Fermi level to where the band gap is located, corresponding to the valence-precise formulation  $(\text{La}^{3+})_{3.3}(\text{Zn}^{2+})_4(\text{As}^{3-})_6$  in which the electron excess is assumed to be alleviated through *RE* deficiencies. At first glance, the closed shell or subshell configurations are generally supported by the occurrence of mostly empty La-based states found above the Fermi level, and mostly filled Zn- and As-based states below. The narrow completely filled Zn 3d-band is centred at  $-8.6$  eV. The As-based states occur as two separate 4s bands (near  $-10$  and  $-12$  eV) and a wide manifold of 4p states within the valence band. However, there is considerable mixing of states from all three atoms in the valence band. In particular, the substantial contribution of La-based states here implies that, contrary to the usual assumption that La atoms mainly participate in ionic interactions, the role of covalent bonding is also important. In fact, as seen in the crystal orbital Hamilton population (COHP) curves (**Figure 4.6**), the La–As covalent bonding interactions are quite significant when compared to the Zn–As interactions. Both types of bonding are optimized when the Fermi level is located at the gap at  $-1$  eV, resulting in integrated COHP values ( $-\text{ICOHP}$ ) of  $0.76$  eV/bond for La–As and  $1.49$  eV/bond for Zn–

As interactions. Above this gap, the interactions are nonbonding for La–As or very weakly antibonding for Zn–As interactions. From this point of view, it may be thought that depopulation of the Zn–As antibonding states favours the occurrence of Zn deficiencies, but as discussed above, entropy stabilization may favour the occurrence for *RE* deficiencies instead. Interestingly, of the three La sites in this structural model, the one sandwiched between the  $[Zn_2As_2]$  slabs (labeled as *RE2* in **Figure 4.2**) participates in the weakest La–As bonds (–ICOHP of 0.63 eV/bond) compared to the other two (–ICOHP of 0.90 and 0.74 eV/bond), despite nearly identical bond lengths of 3.0 Å. Thus, this site should be the least energetically costly one for vacancies to be created (accompanied by the loss of La–As bonding interactions), in agreement with observations.

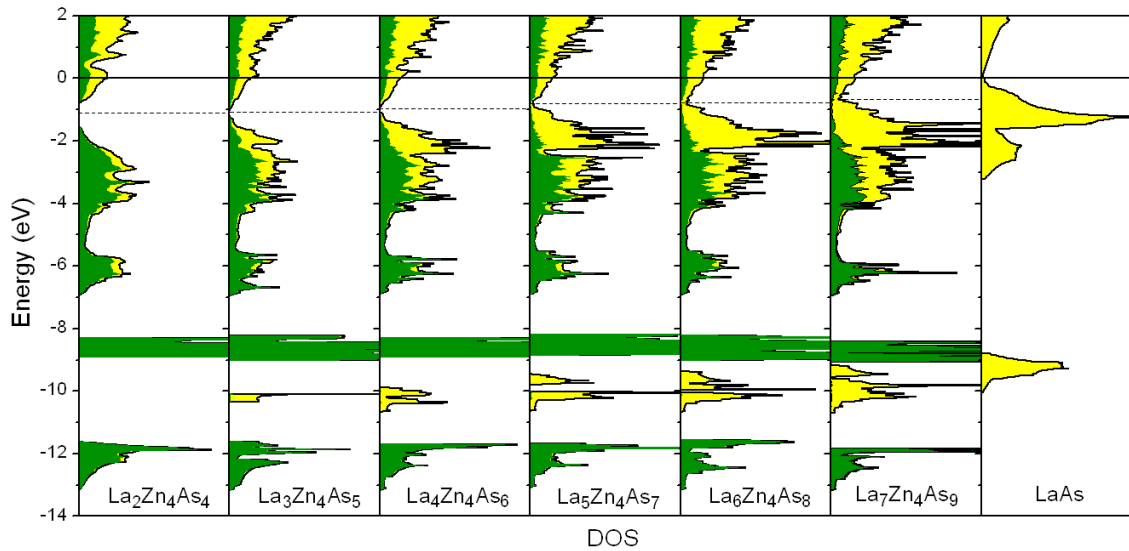


**Figure 4.7** DOS curves for several members of homologous series  $La_2Zn_4As_4 \cdot n(LaAs)$  based on real, rare-earth-deficient compounds ( $n = 0, 2, 3, 4$ ), hypothetical models ( $n = 1, 5$ ), and the limiting extreme of LaAs ( $n = \infty$ ). Regions shaded in green represent projections of states originating from  $[Zn_2As_2]$  slabs; the remaining regions shaded in

yellow are states originating from [LaAs] slabs. Removal of two electrons per formula unit lowers the Fermi level to energies indicated by the dashed lines.

Extrapolation to other members of the homologous series with idealized fully stoichiometric formulas  $\text{La}_2\text{Zn}_4\text{As}_4 \cdot n(\text{LaAs})$  ( $n = 0, 1, 2, 3, 4, 5,$  and  $\infty$ ) shows clear trends in the DOS curves (**Figure 4.7**). The calculations were performed on models with real counterparts ( $n = 0, 2, 3, 4, \infty$ ) or based on hypothetical structures ( $n = 1, 5$ ). As  $n$  increases, the effect of increasing the number of [REAs] slabs is to narrow the gap between valence and conduction bands. The gap starts off at 0.60 eV in the parent  $n = 0$  member ( $\text{La}_2\text{Zn}_4\text{As}_4$ ) and gradually narrows to 0.04 eV at  $n = 2$  ( $\text{La}_4\text{Zn}_4\text{As}_6$ ); beyond this point, the valence and conduction bands just touch at a pseudogap with low DOS (e.g. 0.5 states/eV·cell in  $\text{La}_5\text{Zn}_4\text{As}_7$ ). Lowering the Fermi level to the gap or pseudogap, through removal of two electrons per formula unit, leads to valence-precise formulations consistent with the RE deficiencies observed in the ternary arsenides. The DOS curves show that the electronic structure is derived from a superposition of [REAs] and  $[\text{Zn}_2\text{As}_2]$  slabs. Because the number of  $[\text{Zn}_2\text{As}_2]$  slabs is constant in the homologous series, the projections of states originating from them also remain unchanged. Adding more [REAs] slabs increases the proportion of states originating from isolated As atoms which are partitioned into lower energy 4s (near -10 eV) and higher energy 4p bands (from -4 to -1 eV). In the limit reached in LaAs ( $n = \infty$ ), the DOS curve corresponds essentially to filled As states and empty La states, consistent with the simple formulation  $\text{La}^{3+}\text{As}^{3-}$ . However, even here, there is still substantial mixing of La 5d states with As 4p states, implying that La–As interactions have considerable covalent character. In both this rare-earth-deficient series  $\text{RE}_{2-y}\text{M}_4\text{As}_4 \cdot n(\text{REAs})$  and the previously known metal-deficient

series  $REM_{2-x}As_2 \cdot n(REAs)$ , the transition from a small band gap semiconductor, characteristic of  $CaAl_2Si_2$ -type phases like the parent  $n = 0$  members, to a semimetal, in the limit of LaAs, occurs when the number of  $[REAs]$  slabs is four or more.

### 4.3 Conclusions

The homologous series  $RE_{2-y}Zn_4As_4 \cdot n(REAs)$  illustrates the remarkable diversity of structures that can be built by intergrowing  $[REAs]$  and  $[Zn_2As_2]$  slabs. As in the previously known series  $REZn_{2-x}As_2 \cdot n(REAs)$  made of the same types of slabs, higher members are derived by condensing  $[REAs]$  slabs into thicker blocks, which causes a narrowing of the gap between valence and conduction bands until they eventually just touch to give semimetallic behaviour. In both cases, the formation of vacancies relieves the electron excess that would be found in the fully stoichiometric formulas. Enthalpy factors normally favour Zn defects, as found in  $REZn_{2-x}As_2 \cdot n(REAs)$ , because weakly antibonding Zn–As states can be depopulated. On the other hand, in  $RE_{2-y}Zn_4As_4 \cdot n(REAs)$ , the characteristic feature of single  $[REAs]$  slabs sandwiched between  $[Zn_2As_2]$  slabs leads to particularly high CN of these RE sites, within which formation of defects can provide entropic stabilization. As an alternative to condensing  $[REAs]$  slabs, it is possible to imagine that related homologous series could be built up by condensing  $[Zn_2As_2]$  slabs instead. In such a scenario, the metal sites with the highest CN would be found among the innermost Zn sites of condensed  $[Zn_2As_2]$  blocks. Synthesis of targeted compounds within this hypothetical homologous series has so far been challenging because the formulas would be identical to members found in other series; in other words, these polymorphic forms, if they existed, would likely need to be prepared under different temperature conditions. For example, one hypothetical structure with

condensed  $[\text{Zn}_2\text{As}_2]$  slabs would have the idealized formula  $\text{RE}_5\text{Zn}_4\text{As}_7$ , which is identical to the  $n = 3$  member of the  $\text{RE}_{2-y}\text{Zn}_4\text{As}_4 \cdot n(\text{REAs})$  series. Reassuringly, we do have preliminary evidence for the formation of  $\text{Gd}_5\text{Zn}_{4-x}\text{As}_7$ , in which the structure contains a pair of condensed  $[\text{Zn}_2\text{As}_2]$  slabs with deficiencies in the interior Zn sites, in agreement with predictions.

#### 4.4 References

1. Jansen, M.; Schön, J. C. *Angew. Chem. Int. Ed.* **2006**, *45*, 3406-3412.
2. Kanatzidis, M. G. *Acc. Chem. Res.* **2005**, *38*, 361-370.
3. Poudeu, P. F. P.; Kanatzidis, M. G. *Chem. Commun.* **2005**, *21*, 2672-2674.
4. Lattner, S. E.; Kanatzidis, M. G. *Inorg. Chem.*, **2008**, *47*, 2089-2097.
5. Abakumov, A. M.; Hadermann, J.; Batuk, M.; D'Hondt, H.; Tyablikov, O. A.; Rozova, M. G.; Pokholok, K. V.; Filimonov, D. S.; Sheptyakov, D. V.; Tsirlin, A. A.; Niermann, D.; Hemberger, J.; van Tendeloo, G.; Antipov, E. V. *Inorg. Chem.* **2010**, *49*, 9508-9516.
6. Ainsworth, C. M.; Wang, C.-H.; Johnston, H. E.; McCabe, E. E.; Tucker, M. G.; Brand, H. E. A.; Evans, J. S. O. *Inorg. Chem.* **2015**, *54*, 7230-7238.
7. Mrotzek, A.; Kanatzidis, M. G. *Acc. Chem. Res.* **2003**, *36*, 111-119.
8. Ruck, M.; Poudeu, P. F. P. *Z. Anorg. Allg. Chem.* **2008**, *634*, 482-490.
9. You, T.-S.; Tobash, P. H.; Bobev, S. *Inorg. Chem.* **2010**, *49*, 1773-1783.
10. Karpinnen, M.; Yamauchi, H. *Frontiers in Superconducting Materials*, Narlikar, A. V. Springer-Verlag: Berlin, **2005**, 255-294.
11. Gál, Z. A.; Rutt, O. J.; Smura, C. F.; Overton, T. P.; Barrier, N.; Clarke, S. J.; Hadermann, J. *J. Am. Chem. Soc.* **2006**, *128*, 8530-8540.
12. Ogino, H.; Machida, K.; Yamamoto, A.; Kishio, K.; Shimoyama, J.; Tohei, T.; Ikuhara, Y. *Supercond. Sci. Technol.* **2010**, *23*, 115005-1-115005-5.
13. Nientiedt, A. T.; Jeitschko, W. *J. Solid State Chem.* **1999**, *142*, 266-272.
14. Stoyko, S. S.; Mar, A. *J. Solid State Chem.*, **2011**, *184*, 2360-2367.
15. Nientiedt, A. T.; Lincke, H.; Rodewald, U. Ch.; Pöttgen, R.; Jeitschko, W. *Z. Naturforsch. B: J. Chem. Sci.* **2011**, *66*, 221-226.

16. Stoyko, S. S.; Mar, A. *Inorg. Chem.* **2011**, *50*, 11152-11161.
17. Lin, X.; Stoyko, S. S.; Mar, A. *J. Solid State Chem.* **2013**, *199*, 189-195.
18. Lin, X.; Mar, A. *Inorg. Chem.* **2013**, *52*, 7261-7270.
19. Klüfers, P.; Neumann, H.; Mewis, A.; Schuster, H.-U. *Z. Naturforsch. B: Anorg. Chem., Org. Chem.* **1980**, *35*, 1317-1318.
20. Zwiener, G.; Neumann, H.; Schuster, H.-U. *Z. Naturforsch. B: Anorg. Chem., Org. Chem.* **1981**, *36*, 1195-1197.
21. Nateprov, A.; Cisowski, J.; Heimann, J.; Mirebeau, I. *J. Alloys Compd.* **1999**, *240*, 6-9.
22. Stoyko, S. S.; Khatun, M.; Mar, A. *Inorg. Chem.* **2012**, *51*, 2621-2628.
23. Saparov, B.; Bobev, S. *Acta Crystallogr. Sect. E: Struct. Rep. Online*, **2010**, *66*, i24.
24. Lin, X.; Tabassum, D.; Rudyk, B. W.; Mar, A. *Inorg. Chem.* **2014**, *53*, 8431-8441.
25. Sheldrick, G. M. *SHELXTL, version 6.12*, Bruker AXS Inc., Madison, WI, **2001**.
26. Gelato, L. M.; Parthé, E. *J. Appl. Crystallogr.* **1987**, *20*, 139-143.
27. Tank, R.; Jepsen, O.; Burkhardt, A.; Andersen, O. K. *TB-LMTO-ASA Program, version 4.7*, Max Planck Institut für Festkörperforschung, Stuttgart, **1998**.
28. Brixner, L. H. *J. Inorg. Nucl. Chem.* **1960**, *15*, 199-201.
29. Taylor, J. B.; Calvert, L. D.; Despault, J. G.; Gabe, E. J.; Murray, J. J. *J. Less-Common Met.* **1974**, *34*, 217-232.
30. Pearson, W. B. *The Crystal Chemistry and Physics of Metals and Alloys*, Wiley: New York, **1972**.
31. Anderson, J. S. *Nonstoichiometric Compounds*, Ward, R. American Chemical Society: Washington, DC, **1963**, 1-22.

## Chapter 5

### 5.1 Conclusions

This part of thesis describes some facts of published three projects of chapter 2, chapter 3, and chapter 4; give some insights of ongoing projects; and outline some future direction of these projects.

#### 5.1.1 Reported projects

As mentioned before, *RE-Zn-As* system has very rich chemistry in terms of structure and bonding resulting a wide varieties of phases- tetragonal  $REZn_{0.67}As_2$  (HfCuSi<sub>2</sub>-type structure),<sup>1</sup> tetragonal  $REZn_2As_3$  (novel-type),<sup>2</sup> hexagonal  $REZn_3As_3$  (ScAl<sub>3</sub>C<sub>3</sub>-type),<sup>3</sup> and trigonal  $RE_{0.67}Zn_2As_2$  (CaAl<sub>2</sub>Si<sub>2</sub>-type).<sup>4</sup> Though these compounds have different crystal structures, they are related to each other with some interesting features. For example, they all consist of ZnAs<sub>4</sub> tetrahedra connected in different ways; both  $REZn_{0.67}As_2$  and  $REZn_2As_3$  have arsenic (As) square net but different in thickness;<sup>2</sup> stoichiometric ratio of elements in compounds of both  $REZn_3As_3$  (formed from elemental mixture at 800 °C) and  $RE_{0.67}Zn_2As_2$  (formed in NaCl-KCl salt flux at 800 °C) are same;<sup>3</sup> if the Zn site are fully occupied of  $REZn_2As_3$ ,<sup>2</sup> the formula would be  $REZn_3As_3$  and all above mentioned compounds of *RE-Zn-As* systems belong to zintl phase. These varieties of structures encourage our group to do more study on *RE-Zn-As* system to discover remaining phase, if any.

As the number of compounds forming the CaAl<sub>2</sub>Si<sub>2</sub> is limited to the elements belong to d<sup>0</sup>, d<sup>5</sup>, and d<sup>10</sup> system,<sup>5</sup> one possible way to modify the band structure of  $RE_{0.67}Zn_2As_2$  by changing thickness of REAs which results compounds under the general formula of two homologous series  $REZn_{2-x}As_2 \cdot nREAs$  ( $n = 3-6$ )<sup>6</sup> and  $RE_{2-}$

$y\text{Zn}_4\text{As}_4 \cdot n(\text{REAs})$  ( $n = 2, 3, 4$ ) (**chapter 4**). The band structure calculation of these compounds shows that with the increase the layer of REAs, the band gap decreases providing a useful way to tune the property of these semiconductors.<sup>6</sup> In addition, the compounds of these homologous series have metal deficiency either at Zn sites or RE site responsible for phonon scattering which reduces the thermal conductivity adding them to the list of potential thermoelectrics of  $\text{CaAl}_2\text{Si}_2$ -type compounds.<sup>7</sup>

Substitution of  $d^{10}$  element (Zn) of  $\text{RE}_{0.67}\text{Zn}_2\text{As}_2$  with  $d^5$  (Mn) one was chosen as another way to explore some interesting properties of this  $\text{CaAl}_2\text{Si}_2$ -type structure which results two series of compounds  $\text{RE}_{1-y}\text{Mn}_x\text{Zn}_{2-x}\text{As}_2$  ( $\text{RE} = \text{Eu-Lu}$ ) and  $\text{RE}_{2-y}\text{Mn}_x\text{Zn}_{4-x}\text{As}_4$  ( $\text{RE} = \text{La-Nd, Sm, Gd}$ ) (**Chapter 2**). The complex nature of these structures due to the metal site deficiencies, the presence of disordered transition metal sites, and the inherent anisotropy of  $\text{CaAl}_2\text{Si}_2$ -type structure make these compounds potential candidate for thermoelectrics.

Since it is viable complete substitution Zn ( $d^{10}$ ) with Mn ( $d^5$ ) in the  $\text{CaAl}_2\text{Si}_2$  structure, attempt were made for the compounds of  $\text{REZn}_{2-x}\text{As}_2 \cdot n\text{REAs}$  ( $n = 3-6$ )<sup>6</sup> and  $\text{RE}_{2-y}\text{Zn}_4\text{As}_4 \cdot n(\text{REAs})$  ( $n = 2, 3, 4$ ),  $\text{RE}_{1-y}\text{Mn}_x\text{Zn}_{2-x}\text{As}_2$  ( $\text{RE} = \text{Eu-Lu}$ ) and  $\text{RE}_{2-y}\text{Mn}_x\text{Zn}_{4-x}\text{As}_4$  ( $\text{RE} = \text{La-Nd, Sm, Gd}$ ) to replace Zn with Mn completely. Though partial substitution of Zn with Mn was successful in most cases, complete substitution only possible in one series i.e.,  $\text{RE}_4\text{Mn}_2\text{As}_5$  ( $\text{RE} = \text{La, Pr}$ ) (**Chapter 3**). These compounds are metallic and may show interesting magnetic properties. The two homologous series, as well as the  $\text{RE}_{1-y}\text{Mn}_x\text{Zn}_{2-x}\text{As}_2$  ( $\text{RE} = \text{Eu-Lu}$ ) and  $\text{RE}_{2-y}\text{Mn}_x\text{Zn}_{4-x}\text{As}_4$  ( $\text{RE} = \text{La-Nd, Sm, Gd}$ ) series, were also tried with Cd in place of Zn but the expected compounds did not form.

Another objective of partial Mn substitution in these compounds is to incorporate magnetic property in these semiconductors to explore properties suitable for spintronics.<sup>8</sup> Some systematic studies of these Mn substituted compounds are required to get specific information for use as dilute magnetic semiconductors. But the main challenge is to get pure polycrystalline product or grow suitable crystal for property measurement. Attempts of forming  $RE_4M_2As_5$  phases with other transition metals (*i.e.*, M= Fe, Co, Ni, Cu) resulted only binary phases.

It is also worthy to study  $CaAl_2Si_2$ -type layered crystal structure due to their similarity with the layer of  $BaFe_2As_2$  ( $ThCr_2Si_2$ -type structure) and  $LaFeAsO$  ( $ZrCuSiAs$ -type structure), the iron based superconductors. The tetrahedral layer of (FeAs) is separated by  $Ba^{2+}$  and  $LaO^+$  in  $BaFe_2As_2$  and  $LaFeAsO$  respectively<sup>9</sup> whereas tetrahedral (ZnAs) or (MnAs) layers are separated by  $RE^{3+}$  ions in compounds of  $REZn_{2-x}As_2 \cdot nREAs$  ( $n = 3-6$ ) and  $RE_{2-y}Zn_4As_4 \cdot n(REAs)$  ( $n = 2, 3, 4$ );  $RE_{1-y}Mn_xZn_{2-x}As_2$  ( $RE = Eu-Lu$ ) and  $RE_{2-y}Mn_xZn_{4-x}As_4$  ( $RE = La-Nd, Sm, Gd$ ); and  $RE_4Mn_2As_5$  ( $RE = La, Pr$ ).

### 5.1.2 Current Projects

During my study, I was mainly involved in the following works. I assisted Dr. Xinsong Lin in synthesis and characterization to finish the following projects (not published yet)- (a)  $RECd_{0.67}As_2$  ( $RE=La-Nd, Sm$ ) and  $RECuZn_4As_4$  ( $RE=La-Nd, Sm$ ).

Another type of project was to substitute Zn with Mn in the known compounds of  $RE-Zn-As$  systems. For these purpose, different percentages (*i.e.*, 5%, 10%, 25%, 50%, 75%, 90%, 100% ) of Mn were incorporated in the compounds  $CeZn_{0.67}As_2$ ,  $CeCd_{0.67}As_2$ ,  $Ce_{0.67}Zn_2As_2$ ,  $CeZn_3As_3$ ,  $Ce_4Zn_2As_5$ ,  $C_{3.33}Zn_4As_6$ ,  $Nd_{4.33}Zn_4As_7$ ,  $Sm_{5.33}Zn_4As_8$ ,  $YbZn_2As_2$ , and compounds for further processing were selected based on powder XRD

patterns. The compounds  $CeZn_{0.67}As_2$ ,  $CeCd_{0.67}As_2$ ,  $YbZn_2As_2$  up to 25%, and  $Ce_4Zn_2As_5$  up to 50% shows small peaks of binary phases (e.g.;  $REAs$ ,  $Zn_3As_2$ ) whereas other compounds contains peaks of  $MnAs$ , binary and ternary arsenides and excluded for further attempts. Optimization of conditions resulted some pure samples of  $Ce(Zn,Mn)_{0.67}As_2$ ,  $Ce(Cd,Mn)_{0.67}As_2$ ,  $Yb(Zn,Mn)_2As_2$ ,  $Ce_4(Zn,Mn)_2As_5$  appropriate for magnetic measurement. Single crystal growth of  $Ce(Zn,Mn)_{0.67}Sb_2$  was possible for property measurement. These projects are now in progress.

To find any existing phases for the systems  $RE-M-M'-As$ ,  $RE-M-As$ , and  $RE-M'-As$  ( $M= Mn, Fe, Co, Ni, Cu, Cd, Zn$ ;  $M'=Al, Ga, In, Si, Ge$ ,) have attempted at different compositions and temperatures. Powder XRD and EDX shows some new phases  $REM_3InAs_4$  ( $M=Zn, Cd$ ),  $RE_2MnSiAs_4$  but single crystal data were not possible to solve even the crystal growth was tried at various temperatures. However, an interesting phase,  $RE_{0.8}RE'_{0.2}MnAs_{1.2}$  (tetragonal) was found when mixed rare earth was tried. Optimization of the formula and extension of the series is now ongoing.

### 5.1.3 Future Work

Arsenides have been investigated by several members of our group for last few years, but there is still much work to be done. The most important future work is to synthesis appropriate product for property measurement of all the compounds reported (**Chapter 2-Chapter 4**) in this thesis and determine the homogeneity range of Mn substituted compounds of  $RE-Zn-As$  system. Although in most cases, complete replacement of Zn in the compounds of  $RE-Zn-As$  system with either Mn (except  $RE_4Mn_2As_5$ ) or Cd (except  $RECd_3As_3$ ,  $RECd_{0.67}As_2$ ) resulted in none of the compounds expected, there may be some phases in combination with Mn and Cd in place of Zn sites

which requires a thorough investigation. Because powder XRD pattern of some Mn substituted *RE-Zn-As* compounds show higher percentage of expected compounds.

In addition, various phases of homologous series are missing and the formation of  $RE_{2-y}Mn_xZn_{4-x}As_4$  ( $RE = La-Nd, Sm, Gd$ ) compounds which may consider the first member ( $n=1$ ) of  $RE_{2-y}Zn_4As_4 \cdot n(REAs)$  ( $n = 2, 3, 4$ ) homologous series. Furthermore, the powder XRD pattern of Mn substituted  $RE_{2-y}Zn_4As_4 \cdot n(REAs)$  ( $n = 2, 3, 4$ ) shows good proportion of expected compounds than only ternary phases. It may be possible to discover missing phases of this series for Mn substituted compounds.

The system *RE-M-M'-As* ( $M=$  transition metal,  $M'=$  transition metal or p-block elements) were only investigated by the reactions at high temperature placing direct mixture of the elements, the use of different flux may be a useful tool for synthesis, especially for transition metals with higher melting points (e.g.; Fe, Co). Mixed rare-earth can also help to stabilize some phases and might be a good way to explore some new phases of interesting properties.

## 5.2 References

1. Stoyko, S. S.; Mar, A. *J Solid State Chem.* **2011**, *184*, 2360-2367.
2. Lin, X.; Stoyko, S. S.; Mar, A. *J. Solid State Chem.* **2013**, *199*, 189-195.
3. Stoyko, S. S.; Mar, A. *Inorg. Chem.* **2011**, *50*, 11152-11161.
4. Nientiedt, A. T.; Lincke, H.; Rodewald, U. C.; Pöttgen, R.; Jeitschko, W. Z. *Naturforsch.* **2011**, *66*, 221-226.
5. Zheng, C.; Hoffmann, R. *J. Solid State Chem.* **1988**, *72*, 58-71.
6. Lin, X.; Mar, A. *Inorg. Chem.* **2013**, *52*, 7261-7270.
7. Pomrehn, G. S.; Zevalkink, A.; Zeier, W. G.; van de Walle, A.; Snyder, G. J. *Angew. Chem. Int. Ed.* **2014**, *53*, 3422 -3426.
8. Beach, G. *Nature Mat.* **2010**, *9*, 959-960.
9. Johrendt, D.; Hosono, H.; Hoffmann, R-D.; Pöttgen, R. *Z. Kristallogr.* **2011**, *226*, 435-446.

## Bibliography

1. DiSalvo, J. F. *Science* **1990**, *247*, 649-655.
2. Walsh, A. *Nature Chem.* **2015**, *7*, 274-275.
3. Villars, P.; Cenzual, K. Pearson's Crystal Data - Crystal Structure Database for Inorganic Compounds, Release **2015/16**, ASM international, Materials Park, Ohio, USA.
4. Zdanowicz, W.; Zdanowicz, L. *Annu. Rev. Mater. Sci.* **1975**, *5*, 301-328.
5. Bechstedt, F.; Belabbes, A.; *J. Phys.: Condens. Matter* **2013**, *25*, 273201-273228.
6. Blakemore, J. S. *J. Appl. Phys.* **1982**, *53*, 123-181.
7. Saparov, B.; Mitchell, J. E.; Sefat, A. S. *Supercond. Sci. Technol.* **2012**, *25*, 8-25.
8. Beach, G. *Nature Mat.* **2010**, *9*, 959-960.
9. Erwin, S. C.; Petukhov, A. G. *Phys. Rev. Lett.* **2002**, *89*, 227201-227204.
10. Dietl, T. *Nature Mat.* **2010**, *9*, 965-974.
11. Ohno, H. *Nature Mat.* **2010**, *9*, 952-954.
12. Ohno, H.; Shen, A.; Matsukura, F.; Oiwa, A.; Endo, A.; Katsumoto, S.; Iye, Y. *Appl. Phys. Lett.* **1996**, *69*, 363-365.
13. Cameron, J. M.; Hughes, R. W.; Zhao, Y.; Gregory, D. H. *Chem. Soc. Rev.* **2011**, *40*, 4099-4118.
14. Johrendt, D. *J. Mater. Chem.* **2011**, *21*, 13726-13736.
15. Stoyko, S. S.; Mar, A. *J Solid State Chem.* **2011**, *184*, 2360-2367.
16. Stoyko, S. S.; Mar, A. *Inorg. Chem.* **2011**, *50*, 11152-11161.
17. Lin, X.; Stoyko, S. S.; Mar, A. *J. Solid State Chem.* **2013**, *199*, 189-195.
18. Lin, X.; Mar, A. *Inorg. Chem.* **2013**, *52*, 7261-7270.
19. Geng, F.; Ma, R.; Sasaki, T. *Acc. Chem. Res.* **2010**, *43*, 1177-1185.

20. Zhu, Y.; Murali, S.; Cai, W.; Li, X.; Suk, J. W.; Potts, J. R.; Ruoff, R. S. *Adv. Mater.* **2010**, *22*, 3906-3924.
21. Yakimova, R.; Vasiliauskas, R.; Eriksson, J.; Syväjärvi, M. *Mater. Sci. Forum* **2012**, *711*, 3-10.
22. Pumera, M.; Sofer, Z.; Ambrosi, A. *J. Mater. Chem.* **2014**, *2*, 8981-8987.
23. Baronnet, A. *Prog. Crystal Growth Charact.* **1978**, *178*, 151-211.
24. Pandey, D.; Krishna, P. *Prog. Crystal Growth Charact.* **1983**, *7*, 213-258.
25. Magnéli, A. *Acta Crystallogr.* **1953**, *6*, 495-500.
26. Ruddlesden, S. N.; Popper, P. *Acta Crystallogr.* **1957**, *10*, 538-539.
27. Ruddlesden, S. N.; Popper, P. *Acta Crystallogr.* **1958**, *11*, 54-55.
28. Dion, M.; Ganne, M.; Tournoux, M. *Mater. Res. Bull.* **1981**, *16*, 1429-1435.
29. Jacobson, A. J.; Johnson, J. W.; Lewandowski, J. T. *Inorg. Chem.* **1985**, *24*, 3727-3729.
30. Aurivillius, B. *Ark. Kemi* **1949**, *1*, 463-480.
31. Makovicky, E. *Neues. Jahrb. Miner. Abh.* **1989**, *160*, 269-297.
32. Mrotzek, A.; Kanatzidis, M.G. *Acc. Chem. Res.* **2003**, *36*, 111-119.
33. Poudeu, P. F. P.; Kanatzidis, M. G. *Chem. Commun*, **2005**, *21*, 2672-2674.
34. West, A.R. *John Wiley & Sons Ltd, Chichester*, **1984**.
35. Lewis, G. N. *J. Am. Chem. Soc.* **1916**, *38*, 762-785.
36. Wallace, W. E. *Annu. Rev. Phys. Chem.* **1964**, *15*, 109-130.
37. Nesper, R. *Angew. Chem. Int. Ed. Engl.* **1991**, *30*, 789-817.
38. Nesper, R. *Z. Anorg. Allg. Chem.* **2014**, *640*, 2639-2648.
39. Corbett, J. D. *Chem. Rev.* **1985**, *85*, 383-397.

40. Müller, U. *Inorganic Structural Chemistry*, 2nd ed.; Wiley: Cheichester, 2007.
41. Kossel, W. *Ann. Phys.* **1916**, *49*, 229.
42. Brylak, M.; Möller, M. H.; Jeitschko, W. *J. Solid State Chem.* **1995**, *115*, 305-308.
43. Eschen, M.; Jeitschko, W. *Z. Naturforsch. B.* **2003**, *58*, 399-409.
44. Nientiedt, A. T.; Lincke, H.; Rodewald, U. C.; Pöttgen, R.; Jeitschko, W. *Z. Naturforsch.* **2011**, *66*, 221-226.
45. Hoffmann, R.; Zheng, C. *J. Phys. Chem.* **1985**, *89*, 4175-4181.
46. Zheng, C.; Hoffmann, R.; Nesper, R.; Schnering, H-G, v. *J. Am. Chem. Soc.* **1986**, *108*, 1876-1884.
47. Zheng, C.; Hoffmann, R. *J. Solid State Chem.* **1988**, *72*, 58-71.
48. Johrendt, D.; Felser, C.; Jepsen, O.; Andersen, O. K.; Mewis, A.; Rouxel, J. *J. Solid State Chem.* **1997**, *130*, 254-265.
49. Stoyko, S. S.; Ramachandran, K. K.; Blanchard, P. E. R.; Rosmus, K. A.; Aitken, J. A.; Mar, A. *J. Solid State Chem.* **2014**, *213*, 275-286.
50. Raffius, H.; Mörsen, E.; Mosel, B. D.; Müller-Warmuth, W.; Jeitschko, W.; Terbüchte, L.; Vomhof, T. *J. Phys. Chem. Solids* **1993**, *54*, 135-144.
51. Jeitschko, W.; Terbüchte, L. J.; Rodewald, U. *Ch. Z. Naturforsch.* **2001**, *56*, 1281-1288.
52. Babizhetskyy, V.; Sénéchal, C. Le.; Bauer, J.; Députier, S.; Guérin, R. *J. Alloys Comp.* **1999**, *287*, 174-180.
53. Stoyko S. S.; Oryshchyn S.V. *Visn. Lviv. Derzh. Univ., Ser. Khim.* **2010**, *51*, 74-78.
54. Jeitschko, W.; Jaberg, B. *J. Less-Common Met.* **1981**, *79*, 311-314.

55. Babizhetskyy, V.; Guérin, R.; Simon, A. *Z. Naturforsch., B: J. Chem. Sci.* **2006**, *61*, 733-740.
56. Zelinska, M.; Zhak, O.; Oryshchyn, S.; Polianska, T.; Pivan, J.-Y. *Z. Naturforsch., B: J. Chem. Sci.* **2007**, *62*, 1143-1152.
57. Pivan, J. Y.; Guérin, R.; Sergent, M. *J. Less-Common Met.* **1985**, *107*, 249-258.
58. Wurth, A.; Keimes, V.; Johrendt, D.; Mewis, A. *Z. Anorg. Allg. Chem.* **2001**, *627*, 2183-2190.
59. Dhahri, E. *J. Phys.: Condens. Matter* **1996**, *8*, 4351-4360.
60. Stoyko, S. S.; Ramachandran, K. K.; Mullen, C. S.; Mar, A. *Inorg. Chem.* **2013**, *52*, 1040-1046.
61. Kraus, W.; Nolze, G. *J. Appl. Cryst.* **1996**, *29*, 301-303.
62. Holland, T. J. B.; Redfern, S. A. T. *Mineral. Mag.* **1997**, *61*, 65-77.
63. Massa, W., Ed.; *Crystal Structure Determination, 2nd Ed.* Springer-Verlag: Berlin, **2004**.
64. Sheldrick, G. M. SHELXTL. *Bruker AXS Inc.: Madison, WI* **2001**, 6.12.
65. Gelato, L. M.; Parthé, E. *J. Appl. Crystallogr.* **1987**, *20*, 139-143.
66. Spek, A. L. *Acta Cryst.* **2009**, *D65*, 148-155.
67. Russ, J. C. *Fundamentals of energy dispersive X-ray analysis*, Butterworth: London, **1984**.
68. Hoffmann, R. *Angew. Chem. Int. Ed. Engl.* **1987**, *26*, 846-878.
69. Alemany P.; Canadell, E. Chemical Bonding in Solids, In *The Chemical Bond : Chemical Bonding Across the Periodic Table*, Frenking, G.; Shaik, S. ch15; Wiley-VCH Verlag GmbH & Co. KGaA: Weinheim, Germany. **2014**.
70. Anderson, O. K. LDA, ASA. *Phys. Rev. B: Condens. Matter* **1975**, *12*, 3060-3083.

71. Hott, R.; Kleiner, R.; Wolf, T.; Zwicknagi, G. *Review on Superconducting Materials*, arXiv:1306.0429 [cond-mat.supr-con].
72. Rahman, M. A.; Rahaman, M. Z.; Samsuddoha, M. N. *Am. J. Phys. Appl.* **2015**, *3*, 39-56.
73. Johrendt, D.; Hosono, H.; Hoffmann, R.-D.; Pöttgen, R. *Z. Kristallogr.* **2011**, *226*, 435-446.
74. Tritt, T. M.; Subramanian, M. A. *MRS Bulletin* **2006**, *31*, 188-194.
75. Gascoin, F.; Ottensmann, S.; Stark, D.; Haile, S. M.; Snyder, G. J. *Adv. Funct. Mater.* **2005**, *15*, 1860-1864.
76. Rotter, M.; Pangerl, M.; Tegel, M.; Johrendt, D. *Angew. Chem. Int. Ed.* **2008**, *47*, 7949-7952.
77. Johrendt, D.; Pöttgen, R. *Physica C* **2009**, *469*, 332-339.
78. Mandrus, D.; Sefat, A. S.; McGuire, M. A.; Sales, B. C. *Chem. Mater.* **2010**, *22*, 715-723.
79. Paglione, J.; Greene, R. L. *Nat. Phys.* **2010**, *6*, 645-658.
80. Klüfers, P.; Mewis, A. *Z. Kristallogr.* **1984**, *169*, 135-147.
81. Burdett, J. K.; Miller, G. J. *Chem. Mater.* **1990**, *2*, 12-26.
82. Kranenberg, C.; Johrendt, D.; Mewis, A. *Z. Anorg. Allg. Chem.* **1999**, *625*, 1787-1793.
83. Kranenberg, C.; Johrendt, D.; Mewis, A. *Solid State Sci.* **2002**, *4*, 261-265.
84. Wartenberg, F.; Kranenberg, C.; Pocha, R.; Johrendt, D.; Mewis, A.; Hoffmann, R.-D.; Mosel, B. D.; Pöttgen, R. *Z. Naturforsch. B: J. Chem. Sci.* **2002**, *57*, 1270-1276.
85. Alemany, P.; Llunell, M.; Canadell, E. *J. Comput. Chem.* **2008**, *29*, 2144-2153.

86. Kauzlarich, S. M.; Brown, S. R.; Snyder, G. J. *Dalton Trans.* **2007**, 2099-2107.
87. Toberer, E. S.; May, A. F.; Snyder, G. J. *Chem. Mater.* **2010**, *22*, 624-634.
88. Zhang, H.; Zhao, J.-T.; Grin, Yu.; Wang, X.-J.; Tang, M.-B.; Man, Z.-Y.; Chen, H.-H.; Yang, X.-X. *J. Chem. Phys.* **2008**, *129*, 164713-1-164713-5.
89. Zhang, H.; Fang, L.; Tang, M.-B.; Chen, H.-H.; Yang, X.-X.; Guo, X.; Zhao, J.-T.; Grin, Yu. *Intermetallics* **2010**, *18*, 193-198.
90. Flage-Larsen, E.; Diplas, S.; Prytz, Ø.; Toberer, E. S.; May, A. F. *Phys. Rev. B* **2010**, *81*, 205204-1-205204-7.
91. May, A. F.; McGuire, M. A.; Singh, D. J.; Ma, J.; Delaire, O.; Huq, A.; Cai, W.; Wang, H. *Phys. Rev. B* **2012**, *85*, 035202-1-035202-10.
92. Pomrehn, G. S.; Zevalkink, A.; Zeier, W. G.; van de Walle, A.; Snyder, G. J. *Angew. Chem. Int. Ed.* **2014**, *53*, 3422-3426.
93. Villars, P.; Cenzual, K. *Pearson's Crystal Dat –Crystal Structure Database for Inorganic Compounds, release 2010/11*; ASM International: Materials Park, OH, **2010**.
94. Klüfers, P.; Mewis, A.; Schuster, H.-U. *Z. Kristallogr.* **1979**, *149*, 211-225.
95. Mewis, A. *Z. Naturforsch. B: Anorg. Chem., Org. Chem.* **1980**, *35*, 939-941.
96. Klüfers, P.; Neumann, H.; Mewis, A.; Schuster, H.-U. *Z. Naturforsch. B: Anorg. Chem., Org. Chem.* **1980**, *35*, 1317-1318.
97. Zwiener, G.; Neumann, H.; Schuster, H.-U. *Z. Naturforsch. B: Anorg. Chem., Org. Chem.* **1981**, *36*, 1195-1197.
98. Mahan, A.; Mewis, A. *Z. Naturforsch. B: Anorg. Chem., Org. Chem.* **1983**, *38*, 1041-1045.
99. Tejedor, P.; Stacy, A. M. *J. Solid State Chem.* **1990**, *89*, 227-236.

100. Blanchard, P. E. R.; Stoyko, S. S.; Cavell, R. G.; Mar, A. *J. Solid State Chem.* **2011**, *184*, 97-103.
101. Nateprov, A. N.; Kravtsov, V. Ch.; Moshnyaga, V.; Schorr, S. *Elektron. Obrab. Mater.* **2012**, *48*, 94-98.
102. Ponnambalam, V.; Lindsey, S.; Xie, W.; Thompson, D.; Drymiotis, F.; Tritt, T. M. *J. Phys. D: Appl. Phys.* **2011**, *44*, 155406-1-155406-6.
103. Ponnambalam, V.; Morelli, D. T. *J. Electron. Mater.* **2014**, *43*, 1875-1880.
104. Yu, C.; Zhu, T. J.; Zhang, S. N.; Zhao, X. B.; He, J.; Su, Z.; Tritt, T. M. *J. Appl. Phys.* **2008**, *104*, 013705-1-013705-5.
105. Wang, X.-J.; Tang, M.-B.; Chen, H.-H.; Yang, X.-X.; Zhao, J.-T.; Burkhardt, U.; Grin, Yu. *Appl. Phys. Lett.* **2009**, *94*, 092106-1-092106-3.
106. Zhang, H.; Baitinger, M.; Tang, M.-B.; Man, Z.-Y.; Chen, H.-H.; Yang, X.-X.; Liu, Y.; Chen, L.; Grin, Yu.; Zhao, J.-T. *Dalton Trans.* **2010**, *39*, 1101-1104.
107. Cao, Q.-G.; Zhang, H.; Tang, M.-B.; Chen, H.-H.; Yang, X.-X.; Grin, Yu.; Zhao, J.-T. *J. Appl. Phys.* **2010**, *107*, 053714-1-053714-5.
108. Zhang, H.; Fang, L.; Tang, M.-B.; Man, Z.-Y.; Chen, H.-H.; Yang, X.-X.; Baitinger, M.; Grin, Yu.; Zhao, J.-T. *J. Chem. Phys.* **2010**, *133*, 194701-1-194701-5.
109. Guo, K.; Cao, Q.-G.; Feng, X.-J.; Tang, M.-B.; Chen, H.-H.; Guo, X.; Chen, L.; Grin, Yu.; Zhao, J.-T. *Eur. J. Inorg. Chem.* **2011**, 4043-4048.
110. Zhao, L.-D.; Lo, S.-H.; Zhang, Y.; Sun, H.; Tan, G.; Uher, C.; Wolverton, C.; Dravid, V. P.; Kanatzidis, M. G. *Nature* **2014**, *508*, 373-377.
111. Deng, Z.; Jin, C. Q.; Liu, Q. Q.; Wang, X. C.; Zhu, J. L.; Feng, S. M.; Chen, L. C.; Yu, R. C.; Arguello, C.; Goko, T.; Ning, F.; Zhang, J.; Wang, Y.; Aczel, A. A.; Munsie,

- T.; Williams, T. J.; Luke, G. M.; Kakeshita, T.; Uchida, S.; Higemoto, W.; Ito, T. U.; Gu, B.; Maekawa, S.; Morris, G. D.; Uemura, Y. J. *Nat. Commun.* **2011**, *2*, 422-1-422-5.
112. Deng, Z.; Zhao, K.; Gu, B.; Han, W.; Zhu, J. L.; Wang, X. C.; Li, X.; Liu, Q. Q.; Yu, R. C.; Goko, T.; Frandsen, B.; Liu, L.; Zhang, J.; Wang, Y.; Ning, F. L.; Maekawa, S.; Uemura, Y. J.; Jin, C. Q. *Phys. Rev. B* **2013**, *88*, 081203-1-081203-5.
113. Altshuler, T. S.; Goryunov, Yu. V.; Nateprov, A. V. *J. Phys.: Conf. Ser.* **2011**, *324*, 012020-1-012020-5.
114. Goryunov, Yu.; Fritsch, V.; von Löhneysen, H.; Nateprov, A. *J. Phys.: Conf. Ser.* **2012**, *391*, 012015-1-012015-4.
115. Goryunov, Yu. V.; Levchenko, A. V.; Nateprov, A. N. *J. Phys.: Conf. Ser.* **2012**, *400*, 032013-1-032013-4.
116. Nateprov, A.; Cisowski, J.; Heimann, J.; Mirebeau, I. *J. Alloys Compd.* **1999**, *290*, 6-9.
117. Stoyko, S. S.; Khatun, M.; Mar, A. *Inorg. Chem.* **2012**, *51*, 2621-2628.
118. Saparov, B.; Bobev, S. *Acta Crystallogr., Sect. E* **2010**, *66*, i24.
119. Gladyshevskii, E. I.; Kripyakevich, P. I.; Bodak, O. I. *Ukr. Fiz. Zh.* **1967**, *12*, 447-452.
120. Tank, R.; Jepsen, O.; Burkhardt, A.; Andersen, O. K. *TB-LMTO-ASA Program*, version 4.7; Max Planck Institut für Festkörperforschung: Stuttgart, Germany, 1998.
121. Fairley, N. *CasaXPS*, version 2.3.9; Casa Software Ltd.: Teighmouth, Devon, UK, 2003, <http://www.casaxps.com>.
122. Rühl, R.; Jeitschko, W. *Mater. Res. Bull.* **1979**, *14*, 513-517.

123. Guymont, M.; Tomas, A.; Julien-Pouzol, M.; Jaulmes, S.; Guittard, M. *Phys. Status Solidi A* **1990**, *121*, 21-28.
124. Onoda, M.; Chen, X.; Sato, A.; Wada, H. *J. Solid State Chem.* **2000**, *152*, 332-339.
125. Suga, S.; Ogawa, S.; Namatame, H.; Taniguchi, M.; Kakizaki, A.; Ishii, T.; Fujimori, A.; Oh, S.-J.; Kato, H.; Miyahara, T.; Ochiai, A.; Suzuki, T.; Kasuya, T. *J. Phys. Soc. Jpn.* **1989**, *58*, 4534-4543.
126. Iwanowski, R. J.; Heinonen, M. H.; Janik, E. *Chem. Phys. Lett.* **2004**, *387*, 110-115.
127. Iwanowski, R. J.; Heinonen, M. H.; Janik, E. *Appl. Surf. Sci.* **2005**, *249*, 222-230.
128. Wagner, C. D.; Naumkin, A. V.; Kraut-Vass, A.; Allison, J. W.; Powell, C. J.; Rumble, J. R., Jr. *NIST X-ray Photoelectron Spectroscopy Database*, version 3.5 (web version); National Institute of Standards and Technology: Gaithersburg, MD, 2003, <http://srdata.nist.gov/xps>.
129. Carver, J. C.; Schweitzer, G. K.; Carlson, T. A. *J. Chem. Phys.* **1972**, *57*, 973-982.
130. Aoki, A. *Jpn. J. Appl. Phys.* **1976**, *15*, 305-311.
131. Franzen, H. F.; Umaña, M. X.; McCreary, J. R.; Thorn, R. J. *J. Solid State Chem.* **1976**, *18*, 363-368.
132. Franzen, H. F.; Sterner, C. *J. Solid State Chem.* **1978**, *25*, 227-230.
133. Di Castro, V.; Polzonetti, G. *J. Electron Spectrosc. Relat. Phenom.* **1989**, *48*, 117-123.
134. Eid, K. F.; Stone, M. B.; Maksimov, O.; Shih, T. C.; Ku, K. C.; Fadgen, W.; Palstrøm, C. J.; Schiffer, P.; Samarth, N. *J. Appl. Phys.* **2005**, *97*, 10D304-1-10D304-6.
135. Brisk, M. A.; Baker, A. D. *J. Electron Spectrosc. Relat. Phenom.* **1975**, *7*, 197-213.
136. Jeng, S.-P.; Lad, R. J.; Heinrich, V. E. *Phys. Rev. B* **1991**, *43*, 11971-11977.

137. Stranick, M. A. *Surf. Sci. Spectra* **1999**, *6*, 31-38.
138. Stranick, M. A. *Surf. Sci. Spectra* **1999**, *6*, 39-46.
139. Villars, P.; Cenzual, K. Pearson's Crystal Data-Crystal Structure Database for Inorganic Compounds, ASM International, Materials Park, OH, 2010.
140. Vidyasagar, K.; Hönle, W.; von Schnering, H. G. *Z. Anorg. Allg. Chem.* **1996**, *622*, 518-524.
141. Payne, A. C.; Olmstead, M. M.; Kauzlarich, S. M.; Webb, D. J. *Chem. Mater.* **2001**, *13*, 1398-1406.
142. Hermann, R. P.; Grandjean, F.; Kauzlarich, S. M.; Jiang, J.; Brown, S.; Long, G. J. *Inorg. Chem.* **2004**, *43*, 7005-7013.
143. Denissen, C. J. M.; Sun, D.; Kopinga, K.; de Jonge, W. J. M.; Nishihara, H.; Sakakibara, T.; Goto, T. *Phys. Rev. B* **1987**, *36*, 5316-5325.
144. Lin, X.; Tabassum, D.; Rudyk, B. W.; Mar, A. *Inorg. Chem.* **2014**, *53*, 8341-8441.
145. Lincke, H.; Hermes, W.; Nilges, T.; Pöttgen, R. *Solid State Sci.* **2008**, *10*, 1480-1484.
146. Taylor, J. B.; Calvert, L. D.; Despault, J. G.; Gabe, E. J.; Murray, J. J. *Less-Common Met.* **1974**, *37*, 217-232.
147. Jansen, M.; Schön, J. C. *Angew. Chem. Int. Ed.* **2006**, *45*, 3406-3412.
148. Kanatzidis, M. G. *Acc. Chem. Res.* **2005**, *38*, 361-370.
149. Lattner, S. E.; Kanatzidis, M. G. *Inorg. Chem.*, **2008**, *47*, 2089-2097.
150. Abakumov, A. M.; Hadermann, J.; Batuk, M.; D'Hondt, H.; Tyablikov, O. A.; Rozova, M. G.; Pokholok, K. V.; Filimonov, D. S.; Sheptyakov, D. V.; Tsirlin, A. A.;

- Niermann, D.; Hemberger, J.; van Tendeloo, G.; Antipov, E. V. *Inorg. Chem.* **2010**, *49*, 9508-9516.
151. Ainsworth, C. M.; Wang, C.-H.; Johnston, H. E.; McCabe, E. E.; Tucker, M. G.; Brand, H. E. A.; Evans, J. S. O. *Inorg. Chem.* **2015**, *54*, 7230-7238.
152. Ruck, M.; Poudeu, P. F. P. *Z. Anorg. Allg. Chem.* **2008**, *634*, 482-490.
153. You, T.-S.; Tobash, P. H.; Bobev, S. *Inorg. Chem.* **2010**, *49*, 1773-1783.
154. Karpinnen, M.; Yamauchi, H. *Frontiers in Superconducting Materials*, ed. Narlikar, A. V. Springer-Verlag: Berlin, **2005**, 255-294.
155. Gál, Z. A.; Rutt, O. J.; Smura, C. F.; Overton, T. P.; Barrier, N.; Clarke, S. J.; Hadermann, J. *J. Am. Chem. Soc.* **2006**, *128*, 8530-8540.
156. Ogino, H.; Machida, K.; Yamamoto, A.; Kishio, K.; Shimoyama, J.; Tohei, T.; Ikuhara, Y. *Supercond. Sci. Technol.* **2010**, *23*, 115005-1-115005-5.
157. Nientiedt, A. T.; Jeitschko, W. *J. Solid State Chem.* **1999**, *142*, 266-272.
158. Brixner, L. H. *J. Inorg. Nucl. Chem.* **1960**, *15*, 199-201.
159. Pearson, W. B. *The Crystal Chemistry and Physics of Metals and Alloys*, Wiley, New York, **1972**.
160. Anderson, J. S. *Nonstoichiometric Compounds*, Ward, R. American Chemical Society: Washington, DC, **1963**, 1-22.

# Appendix 1

## Supporting information for chapter 2

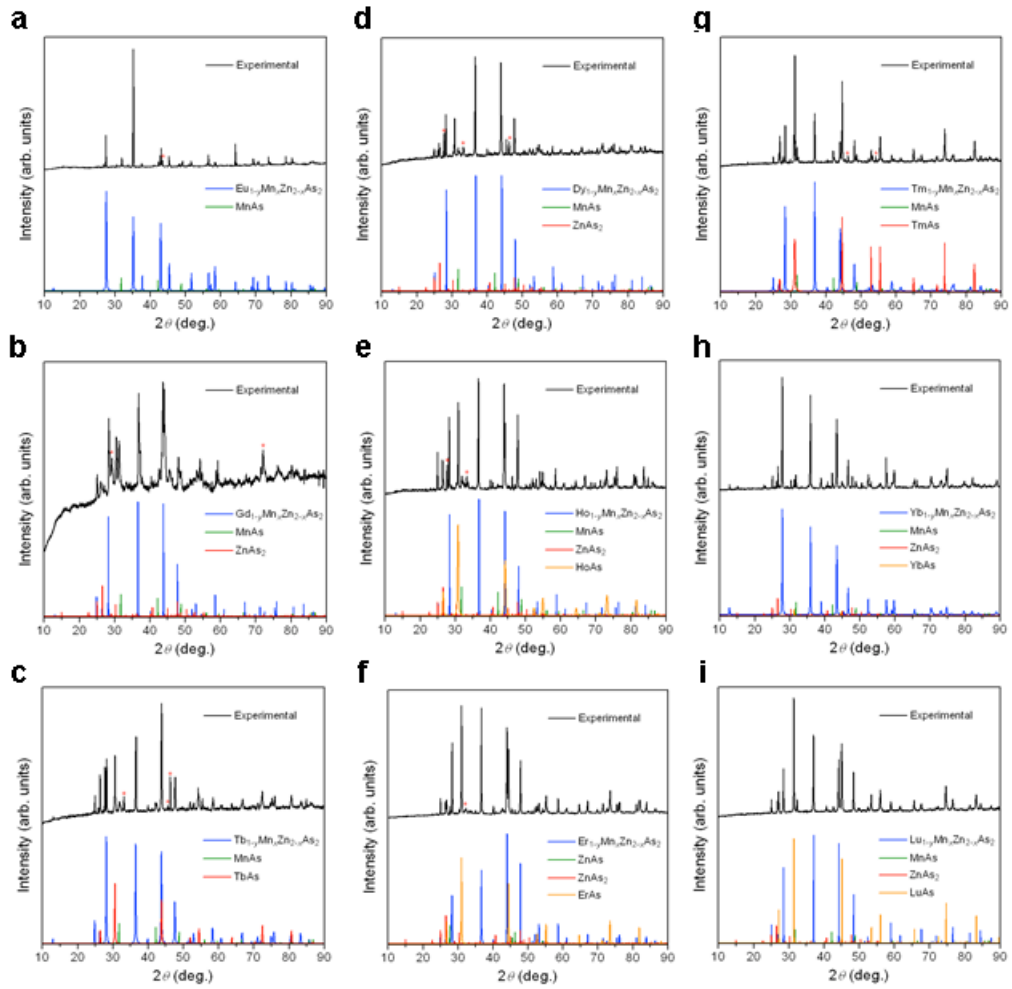


**Figure A 1. 1** Powder XRD patterns for  $RE_{1-y}MnZn_{2-x}As_2$  ( $RE = Eu-Lu$ ). Unidentified peaks are marked with asterisks.

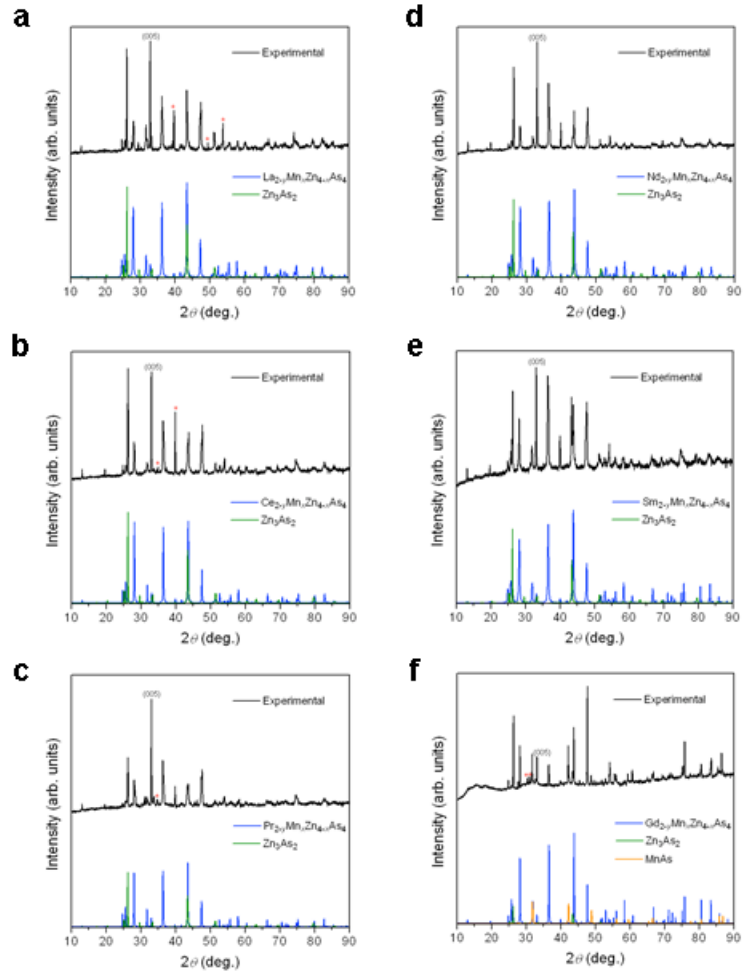


**Figure A 1.2** Powder XRD patterns for  $RE_{2-y}Mn_xZn_{4-x}As_4$  ( $RE = \text{La-Nd, Sm, Gd}$ ). Unidentified peaks are marked with asterisks. Observed (00 $l$ ) peaks are more intense than expected because of preferred orientation (e.g., the (005) peaks are marked).

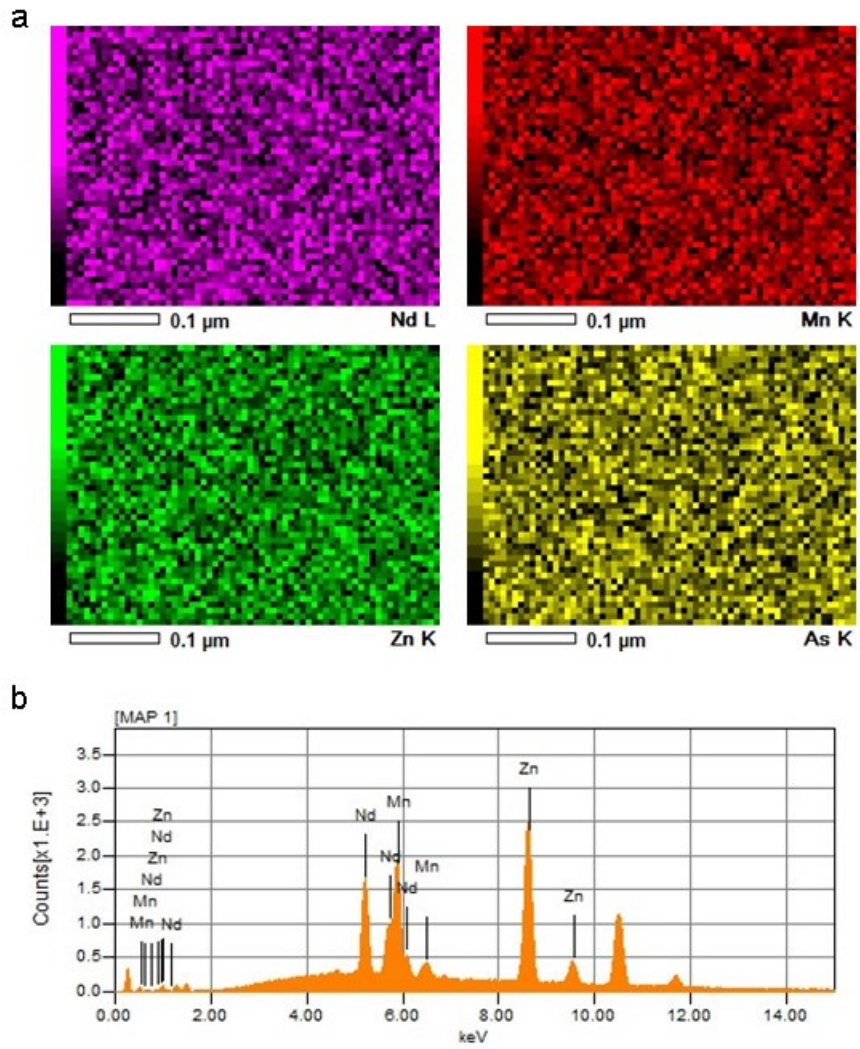


**Figure A 1. 3** (a) Elemental maps and (b) EDX spectrum for  $\text{Nd}_{2-y}\text{Mn}_x\text{Zn}_{4-x}\text{As}_4$ .

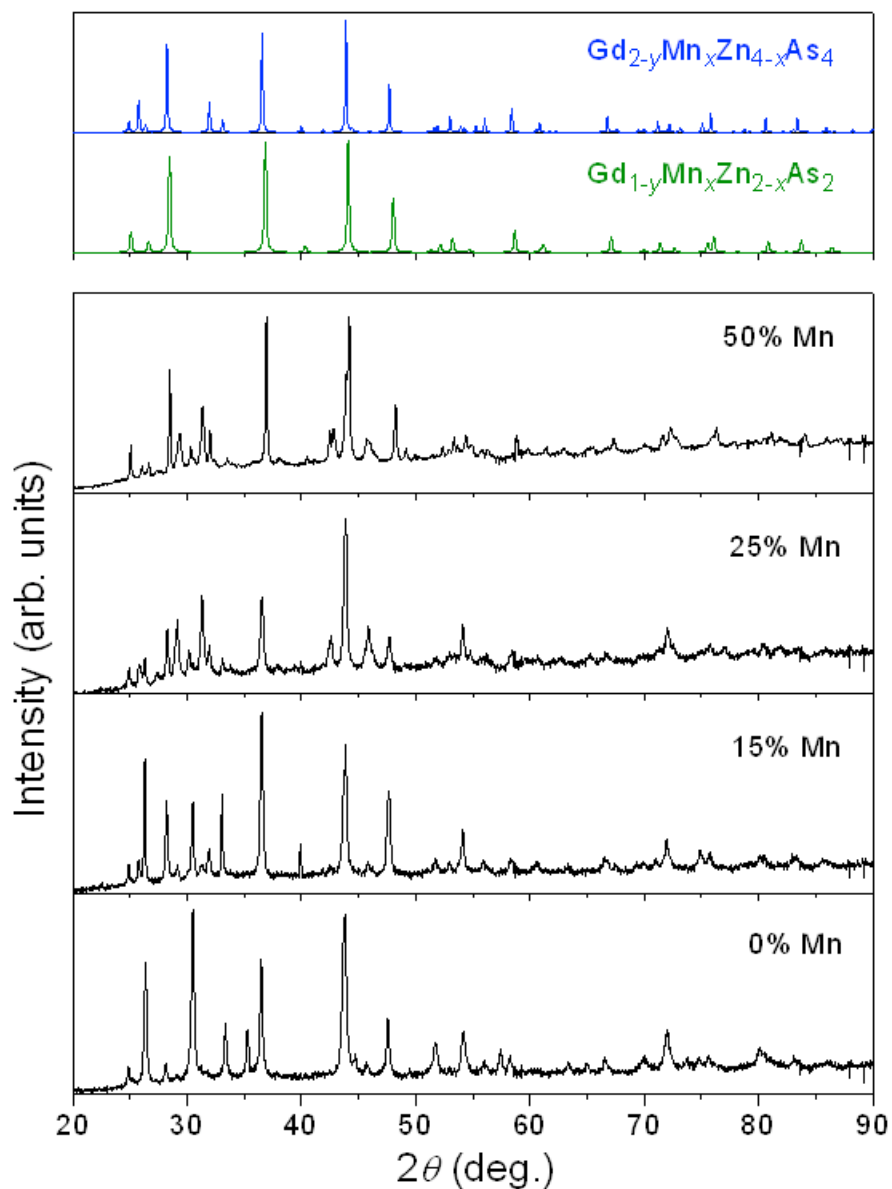


**Figure A 1.4** Powder XRD patterns for products from loading compositions “ $Gd_{0.67}Mn_xZn_{2-x}As_2$ ” (lower panels), compared with simulated patterns for  $Gd_{1-y}Mn_xZn_{2-x}As_2$  and  $Gd_{2-y}Mn_xZn_{4-x}As_4$  (upper panels). Other phases present include various binary arsenides ( $GdAs$ ,  $MnAs$ ,  $ZnAs$ ,  $ZnAs_2$ ,  $Zn_3As_2$ ).

**Table A 1.1** EDX analyses (atomic %) of  $RE_{1-y}Mn_xZn_{2-x}As_2$  and  $RE_{2-y}Mn_xZn_{4-x}As_4$  crystals.<sup>a</sup>

	<b>RE</b>	<b>Mn</b>	<b>Zn</b>	<b>As</b>	<b>n</b>
Gd <sub>0.5</sub> Mn <sub>0.4</sub> Zn <sub>1.6</sub> As <sub>2</sub>	9(1)	20(1)	32(1)	39(1)	16
Tb <sub>0.5</sub> Mn <sub>0.4</sub> Zn <sub>1.6</sub> As <sub>2</sub>	8(1)	17(2)	36(1)	39(2)	18
Dy <sub>0.5</sub> Mn <sub>0.4</sub> Zn <sub>1.6</sub> As <sub>2</sub>	11(1)	9(1)	36(5)	43(5)	8
Ho <sub>0.5</sub> Mn <sub>0.4</sub> Zn <sub>1.6</sub> As <sub>2</sub>	10(3)	11(2)	37(4)	41(3)	11
Er <sub>0.5</sub> Mn <sub>0.4</sub> Zn <sub>1.6</sub> As <sub>2</sub>	9(1)	13(1)	39(1)	39(1)	16
<i>Average</i>	9(1)	14(4)	36(2)	40(2)	
<i>Expected based on</i> <i>RE<sub>0.5</sub>Mn<sub>0.4</sub>Zn<sub>1.6</sub>As<sub>2</sub></i>	11	9	36	44	
La <sub>1.2</sub> Mn <sub>0.9</sub> Zn <sub>3.1</sub> As <sub>4</sub>	15(3)	12(3)	31(2)	42(3)	16
Ce <sub>1.3</sub> Mn <sub>0.8</sub> Zn <sub>3.2</sub> As <sub>4</sub>	10(3)	9(3)	38(3)	43(3)	14
Pr <sub>1.2</sub> Mn <sub>1.0</sub> Zn <sub>3.0</sub> As <sub>4</sub>	13(6)	13(2)	33(5)	41(1)	14
Nd <sub>1.2</sub> Mn <sub>1.0</sub> Zn <sub>3.0</sub> As <sub>4</sub>	10(1)	12(1)	38(1)	40(1)	18
Sm <sub>1.2</sub> Mn <sub>0.9</sub> Zn <sub>3.1</sub> As <sub>4</sub>	14(8)	11(3)	34(7)	42(2)	8
Gd <sub>1.2</sub> Mn <sub>0.9</sub> Zn <sub>3.1</sub> As <sub>4</sub>	11(1)	10(1)	39(1)	40(1)	16
<i>Average</i>	12(2)	11(2)	36(3)	41(2)	
<i>Expected based on</i> <i>RE<sub>1.3</sub>Mn<sub>0.9</sub>Zn<sub>3.1</sub>As<sub>4</sub></i>	14	10	33	43	
EuMn <sub>0.4</sub> Zn <sub>1.6</sub> As <sub>2</sub>	21(1)	8(4)	32(4)	39(2)	11
YbMn <sub>0.3</sub> Zn <sub>1.7</sub> As <sub>2</sub>	24(1)	7(1)	33(1)	36(1)	16
<i>Average</i>	22(2)	7(1)	32(2)	38(3)	
<i>Expected based on</i> <i>REMn<sub>0.4</sub>Zn<sub>1.6</sub>As<sub>2</sub></i>	20	8	32	40	

<sup>a</sup>Average chemical formulas as determined from the single-crystal structure determinations were taken to calculate the expected chemical compositions.

**Table A 1.2** Crystallographic Data for  $RE_{1-y}Mn_xZn_{2-x}As_2$  ( $RE = Eu-Ho$ ).<sup>a</sup>

Formula	EuMn <sub>0.44(6)</sub> Zn <sub>1.56(6)</sub> As <sub>2</sub>	Gd <sub>0.52(1)</sub> Mn <sub>0.40(1)</sub> Zn <sub>1.60(1)</sub> As <sub>2</sub>	Tb <sub>0.52(1)</sub> Mn <sub>0.42(1)</sub> Zn <sub>1.58(1)</sub> As <sub>2</sub>
fm (amu)	427.95	355.03	355.87
space group	$P\bar{3}m1$ (No. 164)	$P\bar{3}m1$ (No. 164)	$P\bar{3}m1$ (No. 164)
$a$ (Å)	4.234(2)	4.109(3)	4.1135(4)
$c$ (Å)	7.198(4)	6.703(5)	6.7246(7)
$V$ (Å <sup>3</sup> )	111.74(14)	98.02(13)	98.54(2)
$Z$	1	1	1
$\rho_{\text{calcd}}$ (g cm <sup>-3</sup> )	6.360	6.014	5.997
crystal dimensions (mm)	0.08 × 0.07 × 0.04	0.04 × 0.03 × 0.03	0.04 × 0.04 × 0.02
radiation	graphite monochromated Mo $K\alpha$ , $\lambda = 0.71073$ Å		
$\mu$ (Mo $K\alpha$ ) (mm <sup>-1</sup> )	37.86	35.88	36.25
transmission factors	0.131–0.470	0.396–0.548	0.362–0.558
$2\theta$ limits	5.66–66.54°	6.08–65.74°	6.06–66.18°
data collected	$-6 \leq h \leq 6,$ $-6 \leq k \leq 6,$ $-10 \leq l \leq 11$	$-6 \leq h \leq 6,$ $-6 \leq k \leq 6,$ $-10 \leq l \leq 10$	$-6 \leq h \leq 6,$ $-6 \leq k \leq 6,$ $-10 \leq l \leq 10$
no. of data collected	1620	1396	1453
no. of unique data, including $F_o^2 < 0$	198 ( $R_{\text{int}} = 0.072$ )	172 ( $R_{\text{int}} = 0.100$ )	177 ( $R_{\text{int}} = 0.032$ )
no. of unique data, with $F_o^2 > 2\sigma(F_o^2)$	158	135	164
no. of variables	11	15	15
$R(F)$ for $F_o^2 > 2\sigma(F_o^2)$ <sup>a</sup>	0.026	0.034	0.025
$R_w(F_o^2)$ <sup>b</sup>	0.043	0.060	0.050
goodness of fit	1.16	1.10	1.07
$(\Delta\rho)_{\text{max}}, (\Delta\rho)_{\text{min}}$ (e Å <sup>-3</sup> )	2.33, -1.69	2.88, -1.52	2.38, -2.04
Formula	Dy <sub>0.53(1)</sub> Mn <sub>0.42(1)</sub> Zn <sub>1.58(1)</sub> As <sub>2</sub>	Ho <sub>0.53(1)</sub> Mn <sub>0.39(1)</sub> Zn <sub>1.61(1)</sub> As <sub>2</sub>	Er <sub>0.51(1)</sub> Mn <sub>0.38(1)</sub> Zn <sub>1.62(1)</sub> As <sub>2</sub>
fm (amu)	362.32	363.93	360.04
space group	$P\bar{3}m1$ (No. 164)	$P\bar{3}m1$ (No. 164)	$P\bar{3}m1$ (No. 164)
$a$ (Å)	4.1023(9)	4.091(3)	4.103(5)
$c$ (Å)	6.7197(16)	6.700(11)	6.722(7)
$V$ (Å <sup>3</sup> )	97.93(4)	97.1(2)	98.02(19)

<i>Z</i>	1	1	1
$\rho_{\text{calcd}}$ (g cm <sup>-3</sup> )	6.143	6.223	6.099
crystal dimensions (mm)	0.06 × 0.04 × 0.03	0.03 × 0.03 × 0.02	0.04 × 0.04 × 0.03
radiation	graphite monochromated Mo <i>K</i> α, λ = 0.71073 Å		
$\mu$ (Mo <i>K</i> α) (mm <sup>-1</sup> )	37.49	38.50	38.13
transmission factors	0.359–0.546	0.437–0.593	0.306–0.532
2θ limits	6.06–65.34°	6.08–66.28°	6.06–65.98°
data collected	–6 ≤ <i>h</i> ≤ 6, –6 ≤ <i>k</i> ≤ 6, –10 ≤ <i>l</i> ≤ 10	–6 ≤ <i>h</i> ≤ 6, –6 ≤ <i>k</i> ≤ 6, –10 ≤ <i>l</i> ≤ 10	–6 ≤ <i>h</i> ≤ 6, –6 ≤ <i>k</i> ≤ 6, –10 ≤ <i>l</i> ≤ 10
no. of data collected	1344	1350	1357
no. of unique data, including $F_o^2 < 0$	168 ( $R_{\text{int}} = 0.053$ )	175 ( $R_{\text{int}} = 0.077$ )	173 ( $R_{\text{int}} = 0.060$ )
no. of unique data, with $F_o^2 > 2\sigma(F_o^2)$	149	135	149
no. of variables	15	15	15
$R(F)$ for $F_o^2 > 2\sigma(F_o^2)$ <sup>a</sup>	0.031	0.032	0.031
$R_w(F_o^2)$ <sup>b</sup>	0.062	0.072	0.045
goodness of fit	1.09	1.09	1.10
(Δρ) <sub>max</sub> , (Δρ) <sub>min</sub> (e Å <sup>-3</sup> )	1.80, –1.09	1.94, –1.05	1.46, –1.37
Formula	Tm <sub>0.43(1)</sub> Mn <sub>0.21(1)</sub> Zn <sub>1.79(1)</sub> As <sub>2</sub>	Yb <sub>0.95(1)</sub> Mn <sub>0.32(6)</sub> Zn <sub>1.68(6)</sub> As <sub>2</sub>	Lu <sub>0.42(1)</sub> Mn <sub>0.20(1)</sub> Zn <sub>1.80(1)</sub> As <sub>2</sub>
fw (amu)	351.03	441.84	348.48
space group	$P\bar{3}m1$ (No. 164)	$P\bar{3}m1$ (No. 164)	$P\bar{3}m1$ (No. 164)
<i>a</i> (Å)	4.0980(18)	4.1682(6)	4.0932(9)
<i>c</i> (Å)	6.664(3)	6.9478(10)	6.6433(14)
<i>V</i> (Å <sup>3</sup> )	96.91(7)	104.54(3)	96.39(4)
<i>Z</i>	1	1	1
$\rho_{\text{calcd}}$ (g cm <sup>-3</sup> )	6.015	7.018	6.003
crystal dimensions (mm)	0.04 × 0.03 × 0.03	0.05 × 0.04 × 0.04	0.04 × 0.03 × 0.03
radiation	graphite monochromated Mo <i>K</i> α, λ = 0.71073 Å		
$\mu$ (Mo <i>K</i> α) (mm <sup>-1</sup> )	38.16	47.12	38.75
transmission factors	0.426–0.558	0.226–0.340	0.392–0.482
2θ limits	6.12–65.96°	5.86–66.32°	6.14–66.06°

data collected	$-6 \leq h \leq 6,$ $-6 \leq k \leq 6,$ $-10 \leq l \leq 10$	$-6 \leq h \leq 6,$ $-6 \leq k \leq 6,$ $-10 \leq l \leq 10$	$-6 \leq h \leq 6,$ $-6 \leq k \leq 6,$ $-10 \leq l \leq 10$
no. of data collected	1379	1485	1345
no. of unique data, including $F_o^2 < 0$	172 ( $R_{\text{int}} = 0.043$ )	186 ( $R_{\text{int}} = 0.040$ )	168 ( $R_{\text{int}} = 0.036$ )
no. of unique data, with $F_o^2 > 2\sigma(F_o^2)$	148	168	149
no. of variables	15	12	15
$R(F)$ for $F_o^2 > 2\sigma(F_o^2)$ <sup>a</sup>	0.021	0.018	0.021
$R_w(F_o^2)$ <sup>b</sup>	0.045	0.040	0.050
goodness of fit	1.11	1.16	1.12
$(\Delta\rho)_{\text{max}}, (\Delta\rho)_{\text{min}}$ ( $\text{e } \text{\AA}^{-3}$ )	0.71, -1.23	1.42, -1.60	0.72, -1.32

$$^a R(F) = \sum ||F_o| - |F_c|| / \sum |F_o|.$$

$$^b R_w(F_o^2) = [\sum [w(F_o^2 - F_c^2)^2] / \sum wF_o^4]^{1/2};$$

$$w^{-1} = [\sigma^2(F_o^2) + (Ap)^2 + Bp], \text{ where } p = [\max(F_o^2, 0) + 2F_c^2] / 3.$$

**Table A 1.3** Crystallographic Data for  $RE_{2-y}Mn_xZn_{4-x}As_4$  ( $RE = \text{La-Nd, Sm, Gd}$ ).<sup>a</sup>

Formula	$\text{La}_{1.25(1)}\text{Mn}_{0.93(2)}\text{Zn}_{3.07(2)}\text{As}_4$	$\text{Ce}_{1.30(1)}\text{Mn}_{0.83(3)}\text{Zn}_{3.17(3)}\text{As}_4$	$\text{Pr}_{1.25(1)}\text{Mn}_{0.95(2)}\text{Zn}_{3.05(2)}\text{As}_4$
fm(amu)	722.33	734.66	727.39
space group	$P\bar{3}m1$ (No. 164)	$P\bar{3}m1$ (No. 164)	$P\bar{3}m1$ (No. 164)
$a$ ( $\text{\AA}$ )	4.159(2)	4.156(5)	4.1533(4)
$c$ ( $\text{\AA}$ )	13.639(7)	13.569(16)	13.5629(13)
$V$ ( $\text{\AA}^3$ )	204.3(2)	203.0(5)	202.61(4)
$Z$	1	1	1
$\rho_{\text{calcd}}$ ( $\text{g cm}^{-3}$ )	5.870	6.010	5.961
crystal dimensions (mm)	$0.07 \times 0.04 \times 0.03$	$0.05 \times 0.03 \times 0.02$	$0.07 \times 0.07 \times 0.04$
radiation	graphite monochromated Mo $K\alpha$ , $\lambda = 0.71073 \text{ \AA}$		
$\mu$ (Mo $K\alpha$ ) ( $\text{mm}^{-1}$ )	32.53	33.69	33.81
transmission factors	0.377–0.623	0.353–0.583	0.247–0.370
$2\theta$ limits	$5.97\text{--}66.38^\circ$	$3.00\text{--}61.75^\circ$	$6.00\text{--}66.38^\circ$
data collected	$-6 \leq h \leq 6,$ $-6 \leq k \leq 6,$ $-20 \leq l \leq 21$	$-6 \leq h \leq 5,$ $-6 \leq k \leq 6,$ $-19 \leq l \leq 19$	$-6 \leq h \leq 6,$ $-6 \leq k \leq 6,$ $-20 \leq l \leq 20$
no. of data collected	2919	2484	2844
no. of unique data,	359 ( $R_{\text{int}} = 0.097$ )	301 ( $R_{\text{int}} = 0.060$ )	353 ( $R_{\text{int}} = 0.034$ )

including $F_o^2 < 0$			
no. of unique data, with $F_o^2 > 2\sigma(F_o^2)$	318	274	324
no. of variables	22	22	22
$R(F)$ for $F_o^2 > 2\sigma(F_o^2)$ <sup>a</sup>	0.052	0.044	0.033
$R_w(F_o^2)$ <sup>b</sup>	0.113	0.125	0.097
goodness of fit	1.15	1.19	1.16
$(\Delta\rho)_{\max}, (\Delta\rho)_{\min}$ (e $\text{\AA}^{-3}$ )	3.04, -3.40	2.17, -4.01	2.25, -4.06
Formula	Nd <sub>1.25(1)</sub> Mn <sub>0.95(3)</sub> Zn <sub>3.05(3)</sub> As <sub>4</sub>	Sm <sub>1.24(1)</sub> Mn <sub>0.87(4)</sub> Zn <sub>3.13(4)</sub> As <sub>4</sub>	Gd <sub>1.24(1)</sub> Mn <sub>0.93(3)</sub> Zn <sub>3.07(3)</sub> As <sub>4</sub>
fm(amu)	731.55	738.52	746.45
space group	$P\bar{3}m1$ (No. 164)	$P\bar{3}m1$ (No. 164)	$P\bar{3}m1$ (No. 164)
$a$ (Å)	4.1283(17)	4.1240(19)	4.1180(14)
$c$ (Å)	13.513(6)	13.507(6)	13.500(5)
$V$ (Å <sup>3</sup> )	199.45(14)	198.9(2)	198.27(15)
$Z$	1	1	1
$\rho_{\text{calcd}}$ (g cm <sup>-3</sup> )	6.091	6.164	6.252
crystal dimensions (mm)	0.07 × 0.06 × 0.03	0.02 × 0.02 × 0.02	0.04 × 0.03 × 0.03
radiation	graphite monochromated Mo $K\alpha$ , $\lambda = 0.71073$ Å		
$\mu$ (Mo $K\alpha$ ) (mm <sup>-1</sup> )	34.84	36.04	37.27
transmission factors	0.195–0.459	0.549–0.653	0.314–0.533
$2\theta$ limits	3.02–65.32°	3.02–65.92°	3.02–65.99°
data collected	$-6 \leq h \leq 6,$ $-6 \leq k \leq 6,$ $-20 \leq l \leq 20$	$-6 \leq h \leq 6,$ $-6 \leq k \leq 6,$ $-20 \leq l \leq 20$	$-6 \leq h \leq 6,$ $-6 \leq k \leq 6,$ $-20 \leq l \leq 20$
no. of data collected	2589	2802	2841
no. of unique data, including $F_o^2 < 0$	342 ( $R_{\text{int}} = 0.102$ )	352 ( $R_{\text{int}} = 0.159$ )	352 ( $R_{\text{int}} = 0.097$ )
no. of unique data, with $F_o^2 > 2\sigma(F_o^2)$	304	224	282
no. of variables	22	22	22
$R(F)$ for $F_o^2 > 2\sigma(F_o^2)$ <sup>a</sup>	0.067	0.051	0.048
$R_w(F_o^2)$ <sup>b</sup>	0.144	0.153	0.135
goodness of fit	1.24	1.06	1.22
$(\Delta\rho)_{\max}, (\Delta\rho)_{\min}$ (e $\text{\AA}^{-3}$ )	5.68, -4.60	2.56, -3.66	3.08, -3.44

$$^a R(F) = \sum ||F_o| - |F_c|| / \sum |F_o|.$$

$${}^b R_w(F_o^2) = [\sum[w(F_o^2 - F_c^2)^2] / \sum w F_o^4]^{1/2};$$
$$w^{-1} = [\sigma^2(F_o^2) + (Ap)^2 + Bp], \text{ where } p = [\max(F_o^2, 0) + 2F_c^2] / 3.$$

## Appendix 2

### Supporting information for chapter 4

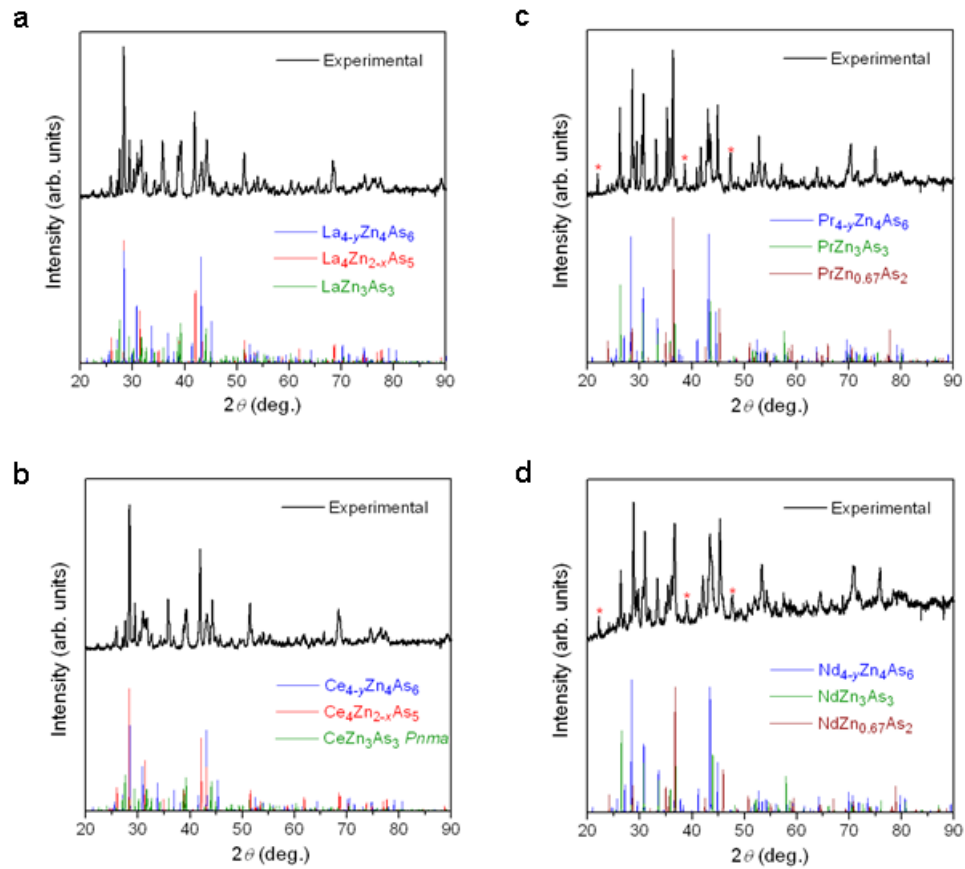


**Figure A 2.1** Powder XRD patterns for  $RE_{4-y}Zn_4As_6$  ( $RE = La-Nd$ ).

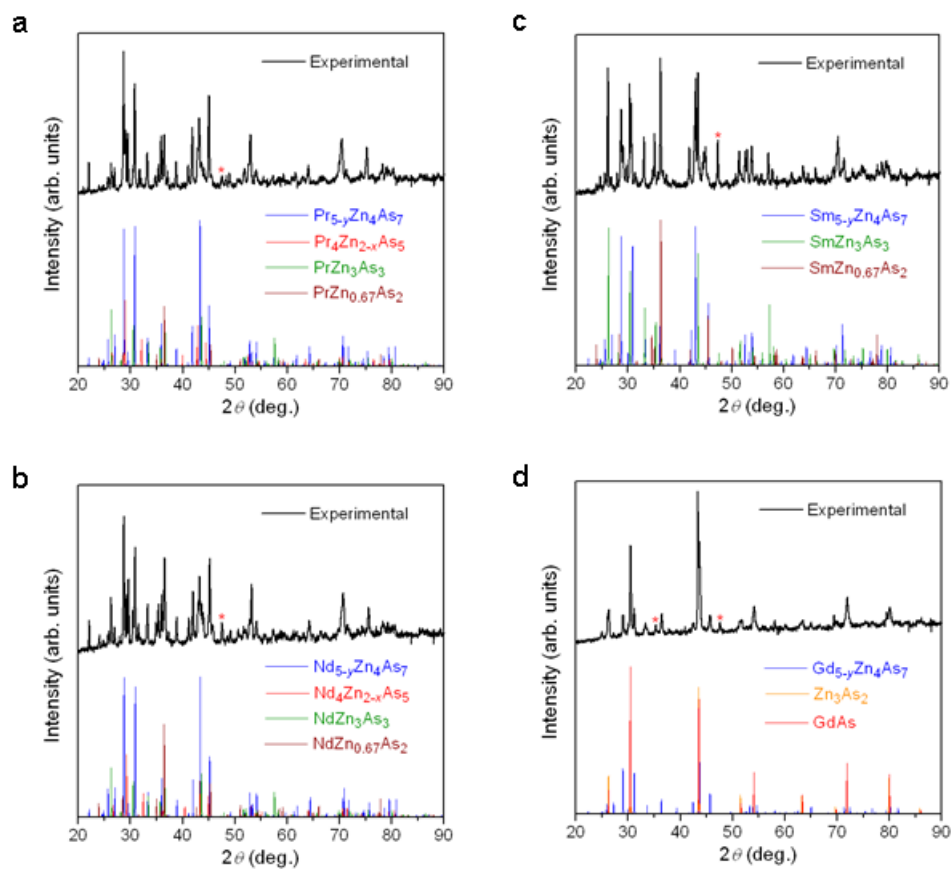


**Figure A 2.2** Powder XRD patterns for  $RE_{5-y}Zn_4As_7$  ( $RE = Pr, Nd, Sm, Gd$ ).

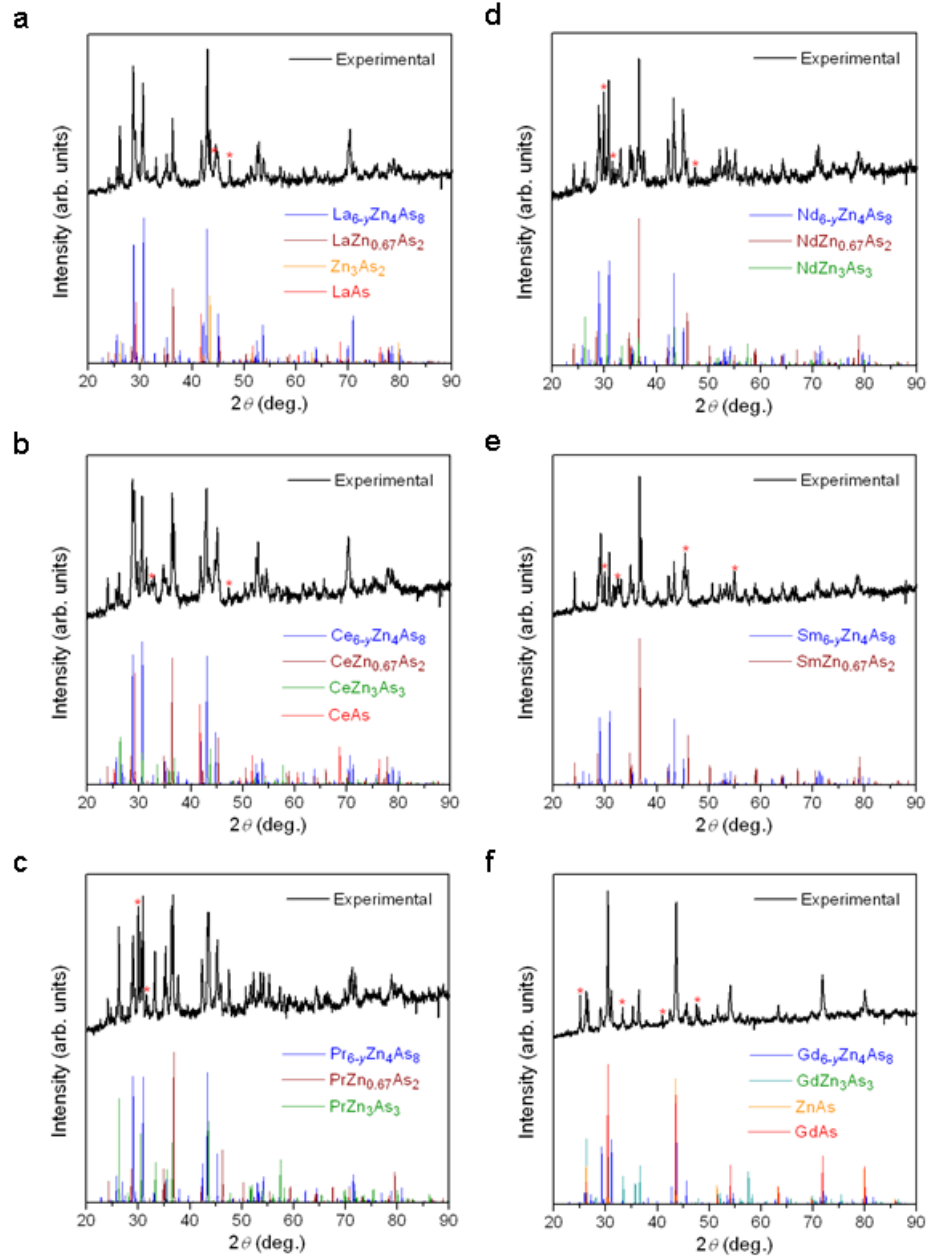


**Figure A 2.3** Powder XRD patterns for  $RE_{6-y}Zn_4As_8$  ( $RE = La-Nd, Sm, Gd$ ).

**Table A 2.1** EDX analyses of  $RE_{2-y}Mn_xZn_{4-x}As_4 \cdot n(REAs)$  ( $RE = La-Nd, Sm, Gd; n = 2, 3, 4$ ) crystals.<sup>a</sup>

Compound	No. of analyses	at. % <i>RE</i>	at. % Mn	at. % Zn	at. % As
$Ce_{3.3}Mn_{1.1}Zn_{2.9}As_6$	16	25(1)	13(1)	20(2)	41(2)
		<i>25</i>	<i>8</i>	<i>22</i>	<i>45</i>
$Pr_{3.5}Zn_4As_6$	16	29(1)		30(2)	41(2)
		<i>26</i>		<i>30</i>	<i>44</i>
$Nd_{3.3}Mn_{0.9}Zn_{3.1}As_6$	15	25(2)	4(1)	28(1)	44(3)
		<i>25</i>	<i>7</i>	<i>23</i>	<i>45</i>
$Nd_{4.4}Zn_4As_7$	19	31(1)		26(1)	43(1)
		<i>29</i>		<i>26</i>	<i>45</i>
$Sm_{4.4}Zn_4As_7$	16	33(2)		26(2)	41(2)
		<i>29</i>		<i>26</i>	<i>45</i>
$Nd_{5.4}Zn_4As_8$	16	30(1)		23(1)	47(1)
		<i>31</i>		<i>23</i>	<i>46</i>
$Sm_{5.4}Zn_4As_8$	15	35(1)		22(1)	43(1)
		<i>31</i>		<i>23</i>	<i>46</i>
$Sm_{5.3}Mn_{0.6}Zn_{3.4}As_8$	16	35(2)	5(1)	20(1)	40(3)
		<i>31</i>	<i>3</i>	<i>20</i>	<i>46</i>
$Gd_{5.3}Mn_{0.6}Zn_{3.4}As_8$	16	34(1)	6(1)	17(1)	42(2)
		<i>31</i>	<i>3</i>	<i>20</i>	<i>46</i>

<sup>a</sup>Expected compositions are indicated in italics

**Table A 2.2** Crystallographic data for  $RE_{2-y}Mn_xZn_{4-x}As_4 \cdot n(REAs)$  ( $n = 2, 3, 4$ ).<sup>a,b</sup>

Formula	Ce <sub>3.32(1)</sub> Mn <sub>1.1(1)</sub> Zn <sub>2.9(1)</sub> As	Pr <sub>3.46(1)</sub> Zn <sub>4</sub> As	Nd <sub>3.34(1)</sub> Mn <sub>0.92(6)</sub> Zn <sub>3.08(6)</sub> As	Nd <sub>4.41(1)</sub> Zn <sub>4</sub> As
	6	6	6	7
Formula mass (amu)	1162.27	1197.14	1182.07	1420.58
Space group	$R\bar{3}m1$ (No. 166)	$R\bar{3}m1$ (No. 166)	$R\bar{3}m1$ (No. 166)	$P\bar{3}m1$ (No. 164)
$a$ (Å)	4.218(3)	4.2067(7)	4.1788(7)	4.197(3)
$c$ (Å)	62.11(4)	62.637(10)	61.727(10)	24.204(15)
$V$ (Å <sup>3</sup> )	957.0(13)	959.9(4)	933.5(3)	369.2(5)
$Z$	3	3	3	1
$\rho_{\text{calcd}}$ (g cm <sup>-3</sup> )	6.050	6.213	6.308	6.390
Crystal dimensions (mm)	0.05 × 0.03 × 0.02	0.09 × 0.04 × 0.02	0.04 × 0.03 × 0.02	0.08 × 0.05 × 0.03
Radiation	graphite monochromated Mo $K\alpha$ , $\lambda = 0.71073$ Å			
$\mu$ (Mo $K\alpha$ ) (mm <sup>-1</sup> )	33.34	35.57	36.14	37.49
Transmission factors	0.277–0.519	0.176–0.558	0.334–0.636	0.153–0.452
$2\theta$ limits	3.93–51.16°	3.90–66.47°	3.96–66.35°	3.37–66.26°
Data collected	$-5 \leq h \leq 5$ , $-5 \leq k \leq 5$ , $-75 \leq l \leq 75$	$-6 \leq h \leq 6$ , $-6 \leq k \leq 6$ , $-94 \leq l \leq 95$	$-6 \leq h \leq 6$ , $-6 \leq k \leq 6$ , $-93 \leq l \leq 93$	$-6 \leq h \leq 6$ , $-6 \leq k \leq 5$ , $-36 \leq l \leq 36$
No. of data collected	2373	4546	4476	4144
No. of unique data, including $F_o^2 < 0$	297 ( $R_{\text{int}} = 0.080$ )	564 ( $R_{\text{int}} = 0.031$ )	546 ( $R_{\text{int}} = 0.049$ )	647 ( $R_{\text{int}} = 0.055$ )
No. of unique data, with $F_o^2 > 2\sigma(F_o^2)$	216	509	440	480
No. of variables	27	27	28	30
$R(F)$ for $F_o^2 > 2\sigma(F_o^2)$ <sup>a</sup>	0.032	0.021	0.026	0.029
$R_w(F_o^2)$ <sup>b</sup>	0.058	0.045	0.056	0.051
Goodness of fit	1.06	1.16	1.08	1.06
$(\Delta\rho)_{\text{max}}$ , $(\Delta\rho)_{\text{min}}$ (eÅ <sup>-3</sup> )	1.74, -1.58	3.60, -2.78	2.05, -2.88	2.75, -3.55

<sup>a</sup> $R(F) = \sum ||F_o| - |F_c|| / \sum |F_o|$ .

<sup>b</sup> $R_w(F_o^2) = [\sum [w(F_o^2 - F_c^2)^2] / \sum wF_o^4]^{1/2}$ ;

$w^{-1} = [\sigma^2(F_o^2) + (Ap)^2 + Bp]$ , where  $p = [\max(F_o^2, 0) + 2F_c^2] / 3$ .

**Table A 2.3** Atomic coordinates and equivalent isotropic displacement parameters for  $RE_{2-y}Mn_xZn_{4-x}As_4 \cdot n(REAs)$  ( $n = 2, 3, 4$ ).

Atom	Wyckoff position	Occupancy	$x$	$y$	$z$	$U_{eq} (\text{Å}^2)^a$
<b>Ce<sub>3.32(1)</sub>Mn<sub>1.1(1)</sub>Zn<sub>2.9(1)</sub>As<sub>6</sub></b>						
Ce1	6c	1	0	0	0.39010(2)	0.0187(4)
Ce2	3b	0.323(9)	0	0	1/2	0.038(3)
Ce3	3a	1	0	0	0	0.0170(5)
M1a	6c	0.721(7) Zn	0	0	0.13028(8)	0.0332(13)
M1b	6c	0.279(7) Mn	0	0	0.1478(3)	0.0332(13)
M2	6c	0.75(6) Zn, 0.25(6) Mn	0	0	0.23276(5)	0.0265(13)
As1	6c	1	0	0	0.08679(4)	0.0186(6)
As2	6c	1	0	0	0.19204(5)	0.0271(7)
As3	6c	1	0	0	0.30451(4)	0.0173(6)
<b>Pr<sub>3.46(1)</sub>Zn<sub>4</sub>As<sub>6</sub></b>						
Pr1	6c	1	0	0	0.38893(2)	0.0079(1)
Pr2	3b	0.461(3)	0	0	1/2	0.0105(3)
Pr3	3a	1	0	0	0	0.0072(1)
M1a	6c	0.879(3) Zn	0	0	0.12902(2)	0.0237(3)
M1b	6c	0.121(3) Zn	0	0	0.14966(15)	0.0237(3)
M2	6c	1 Zn	0	0	0.23482(2)	0.0165(2)
As1	6c	1	0	0	0.08505(2)	0.0088(2)
As2	6c	1	0	0	0.19442(2)	0.0116(2)
As3	6c	1	0	0	0.30502(2)	0.0079(1)
<b>Nd<sub>3.34(1)</sub>Mn<sub>0.92(6)</sub>Zn<sub>3.08(6)</sub>As<sub>6</sub></b>						
Nd1	6c	1	0	0	0.38917(2)	0.0106(1)
Nd2	3b	0.339(4)	0	0	1/2	0.0234(8)
Nd3	3a	1	0	0	0	0.0092(2)
M1a	6c	0.722(4) Zn	0	0	0.12967(3)	0.0259(5)
M1b	6c	0.279(4) Mn	0	0	0.14757(12)	0.0259(5)
M2	6c	0.82(3) Zn, 0.18(3) Mn	0	0	0.23396(2)	0.0186(4)
As1	6c	1	0	0	0.08504(2)	0.0119(2)
As2	6c	1	0	0	0.19321(2)	0.0169(2)
As3	6c	1	0	0	0.30506(2)	0.0097(2)
<b>Nd<sub>4.41(1)</sub>Zn<sub>4</sub>As<sub>7</sub></b>						
Nd1	2d	1	1/3	2/3	0.07145(2)	0.0072(1)
Nd2	2c	1	0	0	0.21498(2)	0.0082(1)

Nd3	1b	0.410(4)	0	0	1/2	0.0112(6)
M1a	2d	0.830(4) Zn	1/3	2/3	0.40538(10)	0.0279(5)
M1b	2d	0.170(4) Zn	1/3	2/3	0.4550(5)	0.0279(5)
M2	2d	1 Zn	1/3	2/3	0.67457(6)	0.0169(3)
As1	2d	1	1/3	2/3	0.28933(5)	0.0087(2)
As2	2d	1	1/3	2/3	0.57088(5)	0.0116(2)
As3	2d	1	1/3	2/3	0.85542(4)	0.0067(2)
As4	1a	1	0	0	0	0.0067(3)
<b>Sm<sub>4.39(1)</sub>Zn<sub>4</sub>As<sub>7</sub></b>						
Sm1	2d	1	1/3	2/3	0.07017(2)	0.0085(1)
Sm2	2c	1	0	0	0.21375(2)	0.0094(1)
Sm3	1b	0.385(4)	0	0	1/2	0.0127(6)
M1a	2d	0.804(4) Zn	1/3	2/3	0.40566(10)	0.0313(5)
M1b	2d	0.196(4) Zn	1/3	2/3	0.4551(4)	0.0313(5)
M2	2d	1 Zn	1/3	2/3	0.67521(6)	0.0183(3)
As1	2d	1	1/3	2/3	0.28737(4)	0.0101(2)
As2	2d	1	1/3	2/3	0.57084(5)	0.0135(2)
As3	2d	1	1/3	2/3	0.85646(4)	0.0083(2)
As4	1a	1	0	0	0	0.0082(3)
<b>Nd<sub>5.43(1)</sub>Zn<sub>4</sub>As<sub>8</sub></b>						
Nd1	6c	1	0	0	0.29167(2)	0.0072(2)
Nd2	6c	1	0	0	0.41684(2)	0.0084(2)
Nd3	3b	0.429(5)	0	0	1/2	0.0088(7)
Nd4	3a	1	0	0	0	0.0069(2)
M1	6c	1 Zn	0	0	0.11573(2)	0.0182(5)
M2a	6c	0.848(5) Zn	0	0	0.19440(4)	0.0268(7)
M2b	6c	0.152(5) Zn	0	0	0.1799(2)	0.0268(7)
As1	6c	1	0	0	0.06309(2)	0.0071(3)
As2	6c	1	0	0	0.14598(2)	0.0121(3)
As3	6c	1	0	0	0.22807(2)	0.0092(3)
As4	6c	1	0	0	0.35437(2)	0.0072(3)
<b>Sm<sub>5.40(1)</sub>Zn<sub>4</sub>As<sub>8</sub></b>						
Sm1	6c	1	0	0	0.29186(2)	0.0072(1)
Sm2	6c	1	0	0	0.41644(2)	0.0082(1)
Sm3	3b	0.400(4)	0	0	1/2	0.0113(5)
Sm4	3a	1	0	0	0	0.0070(1)
M1	6c	1 Zn	0	0	0.11549(2)	0.0169(3)

<i>M2a</i>	<i>6c</i>	0.819(4) Zn	0	0	0.19437(3)	0.0286(5)
<i>M2b</i>	<i>6c</i>	0.181(4) Zn	0	0	0.17988(12)	0.0286(5)
As1	<i>6c</i>	1	0	0	0.06272(2)	0.0068(2)
As2	<i>6c</i>	1	0	0	0.14601(2)	0.0122(2)
As3	<i>6c</i>	1	0	0	0.22865(2)	0.0088(2)
As4	<i>6c</i>	1	0	0	0.35424(2)	0.0070(2)
<b>Sm<sub>5.33(1)</sub>Mn<sub>0.58(1)</sub>Zn<sub>3.42(1)</sub>As<sub>8</sub></b>						
Sm1	<i>6c</i>	1	0	0	0.29173(2)	0.0089(1)
Sm2	<i>6c</i>	1	0	0	0.41670(2)	0.0104(1)
Sm3	<i>3b</i>	0.332(4)	0	0	1/2	0.0212(7)
Sm4	<i>3a</i>	1	0	0	0	0.0088(1)
<i>M1</i>	<i>6c</i>	1 Zn	0	0	0.11598(2)	0.0197(3)
<i>M2a</i>	<i>6c</i>	0.710(4) Zn	0	0	0.19445(3)	0.0255(4)
<i>M2b</i>	<i>6c</i>	0.290(4) Mn	0	0	0.18086(9)	0.0255(4)
As1	<i>6c</i>	1	0	0	0.06290(2)	0.0086(2)
As2	<i>6c</i>	1	0	0	0.14657(2)	0.0157(2)
As3	<i>6c</i>	1	0	0	0.22834(2)	0.0107(2)
As4	<i>6c</i>	1	0	0	0.35430(2)	0.0089(2)
<b>Gd<sub>5.27(1)</sub>Mn<sub>0.62(1)</sub>Zn<sub>3.38(1)</sub>As<sub>8</sub></b>						
Gd1	<i>6c</i>	1	0	0	0.29192(2)	0.0112(2)
Gd2	<i>6c</i>	1	0	0	0.41624(2)	0.0134(2)
Gd3	<i>3b</i>	0.271(5)	0	0	1/2	0.0292(13)
Gd4	<i>3a</i>	1	0	0	0	0.0109(2)
<i>M1</i>	<i>6c</i>	1 Zn	0	0	0.11600(2)	0.0252(4)
<i>M2a</i>	<i>6c</i>	0.692(5) Zn	0	0	0.19511(4)	0.0276(6)
<i>M2b</i>	<i>6c</i>	0.308(5) Mn	0	0	0.18112(11)	0.0276(6)
As1	<i>6c</i>	1	0	0	0.06269(2)	0.0108(3)
As2	<i>6c</i>	1	0	0	0.14706(2)	0.0189(3)
As3	<i>6c</i>	1	0	0	0.22855(2)	0.0128(3)
As4	<i>6c</i>	1	0	0	0.35423(2)	0.0107(3)

---

**Table A 2.4** Interatomic distances (Å) for  $RE_{2-y}Mn_xZn_{4-x}As_4 \cdot n(REAs)$  ( $n = 2, 3, 4$ ).

	<b>Ce<sub>3.32(1)</sub>Mn<sub>1.1(1)</sub>Zn<sub>2.9(1)</sub>As<sub>6</sub></b>	<b>Pr<sub>3.46(1)</sub>Zn<sub>4</sub>As<sub>6</sub></b>	<b>Nd<sub>3.34(1)</sub>Mn<sub>0.92(6)</sub>Zn<sub>3.08(6)</sub>As<sub>6</sub></b>
<i>RE1</i> –As3 (×3)	2.991(2)	2.970(1)	2.952(1)
<i>RE1</i> –As1 (×3)	3.067(2)	3.050(1)	3.012(1)
<i>RE1</i> – <i>M2</i> (×3)	3.652(3)	3.623(1)	3.611(1)
<i>RE2</i> –As2 (×6)	2.901(2)	2.987(1)	2.917(1)
<i>RE2</i> – <i>M1b</i> (×6)	2.702(8)	2.652(4)	2.685(3)
<i>RE2</i> – <i>M1a</i> (×6)	3.324(4)	3.385(1)	3.322(2)
<i>RE3</i> –As3 (×6)	3.023(2)	3.008(1)	2.978(1)
<i>M1a</i> –As2 (×3)	2.530(2)	2.507(1)	2.497(1)
<i>M1a</i> –As1	2.698(6)	2.754(2)	2.755(2)
<i>M1a</i> – <i>M2</i> (×3)	3.053(4)	3.090(1)	3.053(2)
<i>M1b</i> –As2 (×3)	2.469(3)	2.520(3)	2.456(2)
<i>M1b</i> –As2	2.747(18)	2.804(10)	2.817(8)
<i>M1b</i> – <i>M1b</i> (×3)	3.38(2)	3.231(13)	3.374(10)
<i>M2</i> –As2	2.529(5)	2.530(1)	2.515(2)
<i>M2</i> –As1 (×3)	2.581(2)	2.571(1)	2.570(1)
<i>M2</i> – <i>M1a</i> (×3)	3.053(4)	3.090(1)	3.053(2)
	<b>Nd<sub>4.41(1)</sub>Zn<sub>4</sub>As<sub>7</sub></b>	<b>Sm<sub>4.39(1)</sub>Zn<sub>4</sub>As<sub>7</sub></b>	
<i>RE1</i> –As4 (×3)	2.977(1)	2.950(1)	
<i>RE1</i> –As3 (×3)	3.001(2)	2.969(1)	
<i>RE2</i> –As3 (×3)	2.962(2)	2.938(1)	
<i>RE2</i> –As1 (×3)	3.018(2)	2.986(1)	
<i>RE2</i> – <i>M2</i> (×3)	3.608(2)	3.590(1)	
<i>RE3</i> –As2 (×6)	2.969(2)	2.947(1)	
<i>RE3</i> – <i>M1b</i> (×6)	2.657(5)	2.638(4)	
<i>RE3</i> – <i>M1a</i> (×6)	3.334(2)	3.304(2)	
<i>M1a</i> –As2 (×3)	2.490(2)	2.473(1)	
<i>M1a</i> –As1	2.809(3)	2.837(3)	
<i>M1a</i> – <i>M2</i> (×3)	3.101(2)	3.092(2)	
<i>M1b</i> –As2 (×3)	2.502(3)	2.487(3)	

<i>M1b</i> –As2		2.805(12)		2.776(11)
<i>M1b</i> – <i>M1b</i> (×3)		3.259(16)		3.231(14)
<i>M2</i> –As2		2.510(2)		2.503(2)
<i>M2</i> –As1 (×3)		2.576(2)		2.570(1)
<i>M2</i> – <i>M1a</i> (×3)		3.101(2)		3.092(2)
	Nd <sub>5.43(1)</sub> Zn <sub>4</sub> As <sub>8</sub>	Sm <sub>5.40(1)</sub> Zn <sub>4</sub> As <sub>8</sub>	Sm <sub>5.33(1)</sub> Mn <sub>0.58(1)</sub> Zn <sub>3.42(1)</sub> As <sub>8</sub>	Gd <sub>5.27(1)</sub> Mn <sub>0.62(1)</sub> Zn <sub>3.38(1)</sub> As <sub>8</sub>
<i>RE1</i> –As4 (×3)	2.970(1)	2.940(1)	2.942(1)	2.913(1)
<i>RE1</i> –As1 (×3)	3.008(1)	2.973(1)	2.973(1)	2.949(1)
<i>RE2</i> –As1 (×3)	2.960(1)	2.931(1)	2.934(1)	2.899(1)
<i>RE2</i> –As3 (×3)	3.025(1)	2.989(1)	2.989(1)	2.978(1)
<i>RE2</i> – <i>M1</i> (×3)	3.611(2)	3.586(1)	3.598(1)	3.596(2)
<i>RE3</i> –As2 (×6)	2.973(1)	2.944(1)	2.917(1)	2.871(1)
<i>RE3</i> – <i>M2b</i> (×6)	2.665(7)	2.640(4)	2.674(3)	2.662(4)
<i>RE3</i> – <i>M2a</i> (×6)	3.344(2)	3.312(2)	3.314(2)	3.323(2)
<i>RE4</i> –As4 (×6)	2.989(1)	2.956(1)	2.958(1)	2.931(1)
<i>M1</i> –As2	2.510(3)	2.506(2)	2.507(2)	2.522(2)
<i>M1</i> –As3 (×3)	2.578(1)	2.565(1)	2.570(1)	2.558(1)
<i>M1</i> – <i>M2a</i> (×3)	3.098(2)	3.084(2)	3.053(2)	2.995(2)
<i>M2a</i> –As2 (×3)	2.496(1)	2.475(1)	2.488(1)	2.495(1)
<i>M2a</i> –As2	2.793(3)	2.815(2)	2.778(3)	2.715(3)
<i>M2a</i> – <i>M1</i> (×3)	3.098(2)	3.084(2)	3.052(2)	2.995(2)
<i>M2b</i> –As2 (×3)	2.504(4)	2.483(2)	2.455(2)	2.426(2)
<i>M2b</i> –As2	2.818(17)	2.780(10)	2.811(7)	2.764(9)
<i>M2b</i> – <i>M2b</i> (×3)	3.28(2)	3.240(13)	3.348(10)	3.349(13)